Sheffield Hallam University

Investigation of rolling variables on the structure of steel.

EKEBUISI, Godwyn O.

Available from the Sheffield Hallam University Research Archive (SHURA) at:

http://shura.shu.ac.uk/19605/

A Sheffield Hallam University thesis

This thesis is protected by copyright which belongs to the author.

The content must not be changed in any way or sold commercially in any format or medium without the formal permission of the author.

When referring to this work, full bibliographic details including the author, title, awarding institution and date of the thesis must be given.

Please visit http://shura.shu.ac.uk/19605/ and http://shura.shu.ac.uk/information.html for further details about copyright and re-use permissions.

POLYTECHNIC LIBRARY
POND STREET
SHEFFIELD S1 1WB
6789

793290401 3
TELEPEN

Sheffield City Polytechnic Library

REFERENCE ONLY

ProQuest Number: 10694486

All rights reserved

INFORMATION TO ALL USERS
The quality of this reproduction is dependent upon the quality of the copy submitted.

In the unlikely event that the author did not send a complete manuscript
and there are missing pages, these will be noted. Also, if material had to be removed,
a note will indicate the deletion.

ProQuest 10694486

Published by ProQuest LLC (2017). Copyright of the Dissertation is held by the Author.

All rights reserved.
This work is protected against unauthorized copying under Title 17, United States Code
Microform Edition © ProQuest LLC.

ProQuest LLC.
789 East Eisenhower Parkway
P.O. Box 1346
Ann Arbor, MI 48106 – 1346

INVESTIGATION OF ROLLING VARIABLES ON THE STRUCTURE OF STEEL

BY

GODWIN ONYEJIZU EKEBUISI

A THESIS SUBMITTED TO THE COUNCIL FOR NATIONAL ACADEMIC AWARDS IN PARTIAL FULFILMENT FOR THE DEGREE OF

DOCTOR OF PHILOSOPHY

COLLABORATING ESTABLISHMENT:

British Steel Corporation
Sheffield Laboratories
Swinden House
Moorgate
Rotherham S60 3AR
ENGLAND

SPONSORING ESTABLISHMENT:

Department of Metallurgy
Sheffield City Polytechnic
Pond Street
Sheffield S1 1WB
ENGLAND

September 1984

SHEFFIELD CITY POLYTECHNIC LIBRARY
672.32
EK
POND STREET

7932904-01

PREFACE

The research work reported in this thesis was carried out during the period the Candidate was registered for a higher degree.

In accordance with the regulations for PhD in Industrial Metallurgy, a full formal M. Sc. Course work in Metallurgical Process Management was successfully completed. The Candidate's performance during the course was assessed by means of continuous assessment of specific assignments and by written examinations. The details of the course are specified below:

Module 1.

- Process Metallurgy
- Mechanical Metallurgy
- Advanced Thermodynamics

Module 2.

- Applied Economics
- Management Accounting Methods
- Financial Analysis and Control
- Computer Programming and Numerical Analysis
- Operational Research

Module 3.

- High Strength Steels
- Arc Furnace Steel Making
- Continuous Casting
- Corrosion Resistance and High Temperature Materials
- Quality Assurance
- Automatic and Computer Aided Control

Module 4.

THREE Industrial Case Studies

One of these case studies is closely related to the current research investigation and is therefore attached to the thesis as Appendix 1 on pages AP1. 1 to AP1. 38

In addition, the International Conference on Hot working and forming Processes (Sheffield 1979) was attended.

The work described in this thesis is, to the best of my knowledge, original except where reference is made to others, and no part of it has been submitted for an award any-where else.

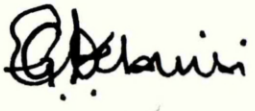

Godwin O. Ekébuisi

ACKNOWLEDGEMENTS

I am grateful to my Supervisors, Mr. G. Butterworth and Dr. F. B. Pickering for their guidance and help during the course of this research. I would also like to thank my Industrial Supervisor, Dr. Terry Gladman of British Steel Corporation for his advice and suggestions.

My sincere thanks also go to Dr. A. W. D. Hills not only for the provision of the research facilities, but also for his active encouragement and moral support throughout the period of this work. To Dr. Briggs, I am profoundly grateful for his invaluable advice, guidance and encouragement without which, this research programme could have been extremely difficult to complete.

The technical support I received from the technicians in the Departments of Metallurgy, Applied Physics and Mechanical and Production Engineering is sincerely acknowledged. In this connection, I am especially thankful to Messers Derek O. Latimer, Gerry E. Gregory, Bob R. Grant, John Bradshaw, Brian Dodds, Russ E. Day, Percy Fletcher and Dr. Brian Lewis - all of Metallurgy Department; to Ms. Gillian Sidda of Applied Physics Department; and to Mr. Stuart J. Leigh of Mechanical and Production Engineering Department.

I would also like to express my thanks to Professors G. J. Davies and C. M. Sellars of Metallurgy Department, University of Sheffield, for the use of the Computer - Controlled Servohydraulic Machine and to Dr. J. M. West for his advice on the chromium - plating of certain materials used for plane strain deformation work.

The contribution by the Institution of Mechanical Engineers towards my financial support at some stage of this work is gratefully acknowledged.

Finally, I would like to thank my wife, Josephine, for her patience, understanding and support throughout the duration of this work and also my children who admirably coped with my research - dominated life of the past few years.

SYNOPSIS

The Literature pertaining to the present research has been critically reviewed.

Hot deformation of Nb-free and Nb-containing stainless and C-Mn steels has been carried out by: upset-forging, rolling, and plane strain compression testing. Also, some gridded lead alloy and some mild steel containing Type I MnS inclusions as markers have been hot rolled. Subsequently investigations have been made into: barrelling and lubrication in upsetting; distributions of temperature and strain during thermo-mechanical working; microstructural processes associated with hot deformation of steel and the evolution of microstructures particularly recrystallised γ-grain size; isothermal transformation of austenite to ferrite; and the mechanisms governing hot deformation of austenite.

Barrelling during the hot upsetting of a solid cylinder arises from the combined effects of interface friction and inhomogeneous distribution of temperature. A barrelling factor, B_f, has been defined to quantify the degree of barrelling and hence of inhomogeneity of deformation in an upset-forged cylinder. Employing glass as a lubricant, an optimised lubrication technique, which ensures homogeneous deformation in upsetting, has been developed and a mechanism of lubrication proposed.

The through-thickness temperature distribution of a deforming material, particularly during hot rolling, is inhomogeneous. Generally, the centre-plane temperature rises due to heat generation while the surface-plane temperature drops due to the cooling effects of the tools. Strain distribution during hot rolling is also inhomogeneous. In particular, the vertical strain (ε_z) is minimum at the surface-plane of the material, maximum at the mid-plane and intermediate at the centre-plane.

Hot deformation of the stainless steels leads to substructure formation and, at suitably high strains, dynamic and metadynamic recrystallisation. Only a small amount of static recovery precedes static recrystallisation. Nucleation for recrystallisation occurs at preferential sites, particularly serrated boundaries and triple junctions of the deformed prior γ-grains. The nucleated γ-grains grow anisotropically and link up to form chains of grains at the prior γ-grain boundaries. Recrystallisation in hot-rolled samples is inhomogeneous at micro and macro-levels. Particularly, recrystallisation is accelerated at the centre-plane and retarded at the surface plane. This effect arises mainly from non-uniform distribution of temperature and is influenced by material and hot rolling variables.

Nb retards recrystallisation by the combined effects of Nb carbide/nitride particles and Nb atoms in solid solution, the particle effect predominating at $\leq$1000°C and the solid solution effect dominating at $\geq$1100°C. Recrystallisation is accelerated by a higher strain, a higher deformation temperature, a higher strain rate, a decrease in the prior γ-grain size, and the presence of deformation bands and twins. A non-isothermal multiple deformation sequence increases the incubation time due to a large temperature drop but promotes a fast recrystallisation rate at the recrystallisation temperature. The kinetics of recrystallisation of the stainless steels have been described by an Avrami recrystallisation equation with the time exponent (k) being from 0.5-2.9. Factors which retard recrystallisation increase k as well as the time (t_{50}) for 50% recrystallisation.

The recrystallised γ-grain size is inhomogeneous and the heterogeneities observed have been categorised into three types. The most important of

these, termed macro-inhomogeneity of recrystallised γ-grain size, is characterised in rolled samples, by the mean recrystallised γ-grain size (d_{rex}) having a maximum value in the surface-plane of the sample, a minimum value in the intermediate-plane and a moderate value in the centre-plane. It arises principally from inhomogeneity of deformation and is accentuated by a Nb addition, a higher strain, a lower rolling temperature, and a lower strain rate.

A Nb addition, a decrease in the prior γ-grain size, a higher strain, a lower deformation temperature, a lower strain rate, a suitably designed multiple deformation sequence and, to lesser extents, deformation bands, twins and second-phase particles - all decrease d_{rex}.

Kinetic relationships developed show that the primary grain growth rate of recrystallised γ-grains decreases with increasing isothermal holding time, is somewhat strain-dependent, and is retarded by the presence of Nb.

A uniform ferrite-grain size is produced only when γ→α transformation proceeds from a completely recrystallised, uniform γ-grain size morphology. Three types of α-grain size inhomogeneity have been identified when the γ→α transformation proceeded from other types of austenite morphology. Inhomogeneous distributions of strain and temperature, and partial recrystallisation, among several other factors, have been invoked to account for the formation of these ferrite grain size heterogeneities.

The activation energy (Q_{def}) for hot deformation of each steel investigated is stress and temperature dependent. Also, Q_{def} values at strains (ε) less than the strain (ε_p) to the peak stress are smaller than Q_{def} values at $\varepsilon \geq \varepsilon_p$, a behaviour which should enable the hot deformation mechanisms to be modelled in terms of suitable activation energies. The temperature compensated strain rate, Z, is exponentially related to the dynamic flow stress.

A model for the prediction of the recrystallised γ-grain size (d_{rex}) as a function of material and thermo-mechanical working variables, incorporating an inhomogeneity factor, has been proposed.

CONTENTS

CHAPTER 1. INTRODUCTION

During conventional hot-working operations, the primary interest is to effect the requisite shape change in as few deformation passes as possible within the confines of the load-capacity of the plant and the hot ductility of the steel. In rolling, this necessitates the use of high reheating temperatures (~1250°C) and the imposition of relatively heavy strains during the roughing reduction when the prevailing high temperatures lower the dynamic flow stress and the mill load while raising the ductility of the material. Structural refinement may be obtained after working, by annealing treatments. Thermo-mechanical processing differs from conventional hot working in that the emphasis is on optimising the mechanical property package (notably, strength, toughness, formability and weldability) obtained in the as-worked product, without any further processing by heat treatment. This objective can only be achieved by control of the microstructure developed in the thermo-mechanically processed product through careful control of compositional and processing variables which govern the microstructural evolution processes, namely, dynamic and static recovery and recrystallisation, and grain growth.

Grain size refinement is the single most important microstructural factor which can be used to optimise the strength-toughness-formability combination of many Engineering Steels, particularly the high strength low alloy (HSLA) steels. In thermo-mechanical processing practice, such as controlled rolling with the allied controlled cooling, the grain size refinement arises predominantly from microalloying carbides/nitrides which inhibit austenite recrystallisation thus permitting the imposition of heavy strains prior to recrystallisation (or $\gamma \rightarrow \alpha$ transformation) and which also retard the growth of recrystallised γ-grains through pinning of the γ-grain boundaries. In non-transforming steels such as austenitic stainless steels, the recrystallised γ-grain size determines the low-temperature properties of the finished product. On the other hand, in steels which undergo a transformation as in the case of HSLA steels, the ferrite grain size developed is what determines the room temperature properties.

A fine ferrite grain size is produced by transformation from heavily deformed elongated γ-grains (the pancake grain structure) because of the increased number of ferrite nucleation sites and the early impingement of the α-grains which forestalls significant grain growth. However, a mixed α-grain size may occur which will have an adverse effect upon

toughness. On the other hand, a fine and uniform ferrite grain size is produced if transformation takes place from a starting structure of fine and uniform recrystallised γ-grains. It would therefore be of considerable industrial significance, for mechanical property optimisation, if a recrystallised γ-grain size which is both as fine as possible and uniform could be obtained after the thermo-mechanical working of both transformable and non-transformable steels. Furthermore, since the recrystallised γ-grain size is in turn dependent upon the material and thermo-mechanical processing variables, it will be of incalculable benefit to the hot working industry if the recrystallised γ-grain size after working can be predicted in terms of the material and thermo-mechanical working variables.

The material variable of relevance in this connection is the (prior) γ-grain size developed after reheating for deformation. This is determined by the reheating temperature and compositional factors, particularly the micro-alloying additions in the case of HSLA steels. In considering thermo-mechanical processing variables of relevance, the parameters traditionally examined are deformation temperature, strain, and strain rate. These variables exert their influence on the recrystallised γ-grain size through their effects on the recrystallisation kinetics of the deformed austenite and on the subsequent growth of the recrystallised γ-grains. However, reduction sequence is also an important thermo-mechanical working variable in that, during multiple deformation sequencing, the total strain must be optimally distributed between the various passes with respect to both temperature and interpass time so as to avoid or at least minimise partial recrystallisation between passes which may lead to the formation of a mixed grain size in the finished product.

In order to study the influence of the processing variables, namely temperature, strain, and strain rate, a variety of testing techniques, notably, tensile testing, upset-forging and plane strain compression testing, are often used. Although each of these process routes has its characteristic draw back, such as localised necking at relatively small strains in tensile testing and the problem of barrelling in upsetting, they all provide a simple deformation pattern. On the other hand, the hot rolling process presents a very complex deformation pattern and is characterised by inhomogeneity, within the material being thermo-mechanically processed, of temperature, strain and strain rate in addition to any inhomogeneity of composition. Although relationships which describe the temperature distribution within the steel stock in the rolling process exist, practical demonstration of the theoretically

predicted temperature profiles does not seem to be available. Furthermore, there appears to be no published work in which the influence of the temperature inhomogeneities on microstructural evolution is explicitly taken into account. Similarly, numerous studies have been carried out into the inhomogeneity of deformation during rolling but where exactly within the material deformation is maximum and what effects the inhomogeneous deformation has on structural evolution and hence on the final properties of the finished product does not seem to have been identified with clarity. It may perhaps be surprising that the long held misleading view that interface friction is the sole cause of inhomogeneous deformation has remained unchallenged even in hot working where internal temperature variations will be expected to contribute to inhomogeneity of deformation as a result of the associated flow stress (resistance to deformation) variations. Strain rate inhomogeneity is also important because strain rate influences both the dynamic flow stress and the microstructural evolution processes.

In addition to the material and processing variables so far identified, the rate controlling microstructural process which governs the hot deformation mechanism must be modelled in terms of an activation energy for hot deformation in order that a model for quantitative prediction of recrystallised γ-grain size can be built as a function of material and processing variables. Information available in this area is very sparse and lacks unanimity from one author to another. In some cases, unrealistic activation energies for hot deformation are assumed thus rendering suspect the validity of any γ-grain size prediction model subsequently developed. Indeed, the data presently available on activation energies for hot deformation is so limited that experimental determination of this parameter for any class of steel being used to develop a quantitative predictive model, is mandatory. Even those models in which reasonably realistic activation energies for hot deformation have been used do not produce satisfactory predictions of the recrystallised γ-grain size. This is not surprising because the effects of inhomogeneities of the processing variables have not been taken into account in developing any of the existing predictive models.

From the foregoing preamble, it is clear that our present knowledge of the influence of thermo-mechanical working variables on the structure of rolled steels and the complex field of inhomogeneities of these processing variables in the hot rolling process, is far from complete. Nor is the extent to which the heterogeneities of the processing variables result

in structural inhomogeneities in the as-rolled steel product fully understood. It is also apparent that no satisfactory model has as yet been developed for accurate prediction of recrystallised γ-grain size as a function of thermo-mechanical working variables. The design of the present research, outlined in Section 3.1, is therefore aimed at bridging this gap in our existing knowledge. Success in this direction will be of prime Engineering and Metallurgical importance for optimising the operation of existing hot rolling mills for the production of as-rolled steel products with an optimum combination of properties and in designing new thermo-mechanical working plants with realistic safety factors which will allow the full exploitation of plant capacities to be made

2.1 HIGH TEMPERATURE THERMO-MECHANICAL WORKING VARIABLES

2.1.1 Major Processing Variables during High Temperature Thermo-Mechanical Working of Steel

Plastic forming of materials at temperatures above about two-thirds of their homologous[1] temperature in the strain rate range of $10^{-1}s^{-1}$ to $\sim 10^{4}s^{-1}$ is customarily recognised as hot working. At such temperatures and strain rates, the processing variables influence the work-hardening rate and the microstructural restoration processes and these in turn interact in a complex manner to determine the structure developed in the deformed material. High temperature thermo-mechanical processing, typified by controlled rolling[2,3] (see also Case Study in Appendix 1) is a special form of hot working in that it involves careful control of compositional and processing variables in order to obtain certain desired microstructures and mechanical properties in the finished product without any further processing such as heat treatment. In controlled rolling of High Strength Low Alloy (HSLA) Steels for example, the most important compositional variables are the micro-alloying additions, while the major processing variables are temperature, deformation, and strain rate. These variables, which are generally distributed inhomogeneously within the material during rolling, will now be examined in detail.

2.1.2 Micro-Alloying Additions

The familiar micro-alloying additions to steels are niobium, vanadium, titanium and aluminium, although niobium is generally considered[2] (see also Appendix 1) to be the best for effective inhibition of recrystallisation of austenite during the production of HSLA steels. The commercial importance of micro-alloying lies mainly in improving strength and toughness through grain size refinement and to a lesser extent, in precipitation strengthening.

The precipitation strengthening is due to the precipitation of fine carbide/nitride particles in the ferrite[4-6] during or after $\gamma \rightarrow \alpha$ transformation. Strain induced precipitation in the austenite may contribute to strength through grain refinement by inhibiting austenite recrystallisation so that greater deformation can be effected and by restricting grain growth[4,6] of recrystallised γ-grains through pinning[7] of the grain boundaries: this does not contribute to precipitation strengthening and may in fact reduce it by diminishing the amount of carbide/nitride particles for potential precipitation in the ferrite. Only vanadium and niobium produce significant precipitation

strengthening when present as a micro-alloying addition. Aluminium nitride (Al forms no stable carbide) produces no precipitation hardening. The importance of Ti seems to lie in the recent use of it (with enhanced N) at levels of 0.01-0.015% to inhibit γ-grain growth at high reheating temperatures prior to hot deformation[5]. The prior γ-grain growth inhibition comes from the grain-boundary pinning action of TiN particles which have high stability and slow coarsening rate characteristics compared to VN or even NbN.

The degree of precipitation strengthening achieved strongly depends upon the austenitisation temperature. This dependence has been extensively studied[8-11] and the results, usually expressed in the form of equations[2,8-11] is exemplified by[10]:

$$\log_{10}[Nb][C]^{0.83}[N]^{0.14} = \frac{-9800}{T} + 4.46 \quad \text{----------(1)}$$

where T is the temperature in Kelvin, and the bracketed terms represent the dissolved components of the appropriate element, expressed in mass%. Maximum precipitation hardening occurs at the stoichiometric composition[12] since the maximum temperature dependence of solubility occurs at the stoichiometric ratio of the micro-alloying element with respect to carbon and nitrogen. The precipitation temperature and cooling rate control the size and distribution of the precipitates through their effects on the coarsening rate of the precipitates. If the precipitation temperature is high and the cooling rate low, a few coarse precipitates form which are not effective for strengthening. On the other hand, at low temperatures and fast cooling rates, many fine particles which are semi-coherent with the matrix are formed and these produce maximum precipitation strengthening. Precipitation is generally harmful to impact properties but, in micro-alloying practice, the beneficial effects on impact properties from grain refinement and from free nitrogen entrapment as carbonitrides outweigh the deleterious effects of precipitation strengthening.

Grain refinement is the major strengthening mechanism imparted to thermo-mechanically worked steels by the micro-alloying additive. Traditional methods of grain refinement involve increasing one or all of the three factors[10] - carbon content, manganese content, cooling rate - since each depresses the transformation temperature thereby increasing the nucleation rate of the ferrite and restricting the growth of nucleated ferrite grains. However, carbon, while increasing strength, impairs weldability, formability, toughness and, in stainless steels corrosion resistance. Manganese can also only be increased to a level consistent with the absence of bainite. For example, if Mn is too high, it may depress the $\gamma \rightarrow \alpha$ transformation temperature

too far and/or interact with carbon, resulting in the formation of bainite. Accelerated cooling has been suggested[4,13] but this does not produce uniform cooling.

Grain refinement by micro-alloying additions is optimised by careful control of thermo-mechanical working variables and operates unimpaired at very low carbon contents. During austenitisation, any undissolved carbonitride particles pin the grain boundaries and the solute drag exerted by the micro-alloying element in solution also assists to immobilise the grain boundaries, thus restricting the growth of the prior austenite grains. During deformation, recrystallisation is inhibited by the micro-alloying additive thus permitting the imposition of large reductions either in one or a series of deformation sequences to produce heavily deformed, elongated, pancaked, γ-grains. These pancaked γ-grains transform to fine α-grains because ferrite nucleation sites are much increased[14] and significant growth is forestalled by early impingement of the α-grains. If however the unrecrystallised γ-grains are deformed further to a total strain greater than the critical strain (ε_c) for dynamic recrystallisation, complete recrystallisation may occur[14,15,16]. In this case, the recrystallised γ-grain size is refined because of: the large amount of available nucleation sites, early impingement of the recrystallised grains, and inhibition of growth of these grains by the pinning of their boundaries by carbonitride (or carbide/nitride) particles. If the $\gamma \rightarrow \alpha$ transformation now occurs, the resulting α-grains are correspondingly fine. Industrially, HSLA steel strip with grain size as low as ~4μm has been produced[17] by thermo-mechanical processing. Such grain size control has in turn made commercially available, steels of excellent weldability and low impact transition temperature for use in large diameter pipes[18], having yield strengths of up to 480 MP_a. Also, it has made available steels with yield strengths exceeding 600 MP_a[19] for other applications such as in the automotive and high-rise building industries where weight savings and easy repair by welding are highly desirable.

Considering recrystallisation inhibition by the micro-alloying additions, it is now widely accepted that niobium is more effective than vanadium although at appropriate vanadium and nitrogen levels, vanadium may exert similar effects to niobium, particularly on dynamic recrystallisation[20], albeit at about a 50°C lower temperature[20-23].

The precise mechanism by which the micro-alloying additive, particularly niobium, inhibits recrystallisation has been a subject of unresolved contro-

versies between the advocates of the particle effect[21] and the advocates of the solid solution effect[24-26]. Basically, the precipitate particle effect involves the niobium carbonitride particles exerting a Zener drag on the grain boundaries to reduce their migration rate and/or the Nb(C,N) particles pinning individual dislocations and subgrain walls thus preventing dislocation rearrangements and subgrain re-orientations which are important in the development of recrystallisation nuclei. The solute effect involves the dissolved atoms of niobium either exerting solute drag which reduces the migration rate of high-angle boundaries, or directly inhibiting the diffusional drift of point defects which would otherwise facilitate nucleation mechanisms such as subgrain coalescence. Recent work by Lombry et al[27] indicates that at temperatures $\gtrsim$1100°C, only the precipitate particle effect operates. The validity of this generalised conclusion over a wide range of niobium additions seems doubtful. Amin and Pickering[27b] have also shown the operation of solute drag at high rolling temperatures. It is considered that both the solute drag and precipitate particle effects are important in inhibiting recrystallisation and that both may operate simultaneously under suitable conditions. It is well known that the precipitate particle effect is increased by a larger volume fraction and a finer particle size[28-33].

2.1.3 TEMPERATURE

2.1.3.1 Temperature Inhomogeneities and Profiles during Rolling

The temperature within the reheated steel stock is not necessarily uniform when it leaves the reheating furnace though efforts are made to achieve uniformity[34]. Even if the material leaves with a uniform temperature, this will be expected to become non-uniform prior to deformation due to heat losses by radiation, conduction, and convection. Such a temperature gradient will become even steeper when the stock enters the rolling pass as a result of heat losses at the various zones characteristic of typical rolling mills. The most important of these zones are depicted in Fig.1a and comprise the high-pressure descaler zone, the approach and rolling roll tables, the deformation zone, and the run-out and inter-stand roll tables. These heat losses, together with heat generation by plastic deformation and interface friction, create within the material, temperature inhomogeneities which are sometimes described in terms of temperature profiles[34,35].

In the axial direction, two possible temperature profiles (Fig.2a)[35] have been identified, namely a run-down in temperature from head to tail and a run-up in temperature from head to tail. An ideal axial temperature distribution

is the uniform temperature from head to tail included in Fig.2a. In the thickness direction, Cornfield and Johnson[34] identified three possible temperature distributions (Fig. 2b), viz: cold-surface with hot interior, hot-surface with cold interior, and uniform temperature all through the thickness. Hollander[35] considered the effect of axial temperature inhomogeneity on gauge variations while Cornfield and Johnson[34] considered the influence of through-thickness temperature heterogeneity on strain distribution. These authors[34,35] did not consider the influence of such inhomogeneities on structural modification processes.

Employing heat conduction equations, various workers[35-39] have proposed relationships to describe the temperature distribution within the steel stock in the rolling process. In some of the analyses[35, 37] the descaler spray jets, the inter-stand zones, the insulating effect of scale[35], and heat generated by recrystallisation[35] have even been considered. However, practical demonstration of the theoretically predicted[35-39] temperature profiles seems not to be available. Furthermore, there is no published data on how to minimise through-thickness temperature variations during hot rolling although such information has been suggested[40,41] for minimising axial temperature variations. It is therefore not surprising that in hot strip mills, rolling temperatures are generally defined by the furnace temperature[36] or by the temperature of the material after leaving the last roughing stand, the later being scanned at the material surface with radiation pyrometers without taking into account the internal temperature variations. Obviously, practical elucidation of the phenomenon is of great metallurgical and engineering interest and will be attempted in the present work.

2.1.3.2 Temperature Distribution within the Material during Upset-forging

Hot upset-forging, like hot rolling, has been used extensively in the present research. It is therefore pertinent to examine briefly as well, the distribution of temperature within the material during upset-forging.

As in the rolling process, a material leaving the reheating furnace with uniform through-thickness temperature distribution will be expected to acquire a surface-to-centre temperature gradient as a result of surface air cooling before the upsetting starts. When 'upset-deformation' begins, the material loses further heat, mainly by conduction to the relatively cold dies and radiation and convection losses are of secondary importance.

Heat generated by plastic deformation, interface friction and dynamic recrystallisation constitute heat supply sources to the process. This supply and removal of heat (Fig. 1b), creates within the material being forged, an inhomogeneous temperature distribution whose severity depends upon the thermo-mechanical processing variables and several other factors such as the thermal properties and conditions of the dies, the size of the specimen, and the nature of the interface layer with respect to both heat transfer and friction coefficient.

Neither analytical nor experimental work seems to be available on the temperature distribution within the material during upset-forging. The well publicised work of Beck[42,43] essentially dealt with heat transfer from the material to the platens and not within the material being deformed.

2.1.4 PLASTIC DEFORMATION

2.1.4.1 Fundamental Concepts of the Deformation Mode in Rolling

Siebel's pioneering works[44,45] in the development of rolling theories for the calculation of rolling loads started with a homogeneous differential equation which he solved by assuming:- slipping friction at the contact faces between the rolls and the materials, absence of lateral spread, and homogeneity of deformation. Subsequent rolling theories[46-50] were essentially similar to those of Siebel, with the assumptions of non-variabilities of both flow stress and friction coefficient along the arc of contact, absence of lateral spread, and homogeneity of deformation being common to all the theories[46-50].

The above assumptions, particularly that of homogeneity of deformation, render the validity of the theories questionable. Ekelund's "Parallelopipedal deformation theory"[46] summarises the homogeneous deformation concept. The theory defines a rectangular parallelopiped as a rectangular block, the deformation of the block being termed parallelopipedal if, in the course of deformation, all the plane faces move parallel to themselves and remain plane. A body may be considered as being composed of a large number of such rectangular blocks and if all the composite blocks undergo parallelopipedal deformation, then the whole body actually undergoes parallelopipedal deformation. The flow lines of the parallelopipedal deformation are hyperbolas, Fig. 3. If deformation during rolling were homogeneous, the parallelopipedal deformation theory would apply and plane parallel sections before rolling would remain plane and parallel after rolling. However, deformation during rolling is considerably inhomogeneous

and so the parallelopipedal deformation theory cannot be valid in rolling. Roll flattening[51], and material and deformation variables influence the extent of the inhomogeneity of deformation during rolling.

2.1.4.2 Methods for Studying Material flow and Inhomogeneity of Deformation in Rolling

Hollenberg's experimental technique[52] for investigating material flow in rolling consisted of drilling holes in a wrought-iron stock perpendicular to the surfaces to be rolled and then plugging these holes with short rods of the same material. After reheating, the bar was rolled only up to half its original length and the mill was stopped to withdraw the partially rolled stock. After cooling, upon examining the shape of the rods by sectioning, he found that they were bent during the rolling deformation in the direction opposite to the movement of the stock, indicating that the material flow in any cross-section is such that the central layers lag behind the surface layers. Metz[53] replaced the smooth rods of Hollenberg by bolts and covered the four faces of certain rectangular test specimens with engraved grid networks so that he could study material flow within, and on the surface of, the material. Metz confirmed Hollenberg's findings and concluded further that heavy reductions and/or lower temperatures produce more drastic bending of the bolt axis. These experiments which were performed using wrought-iron[52] and mild steel[53] have been repeated with lead[54] and aluminium[55,56] with only minor modifications and all the results point to one conclusion, viz, plastic deformation during rolling is inhomogeneous.

A notable divergence from the use of inserts and grid networks was Orowan's plasticine modelling[57] in which he built a wide slab out of alternate laminae of white and grey plasticine and then rolled this in a two-high mill with rough wooden rolls. The slab was only partially rolled and then withdrawn to obtain transverse and longitudinal sections. After studying these sections, Orowan proposed a diagramatic representation of the mode of deformation within the roll gap in which regions of plastic deformation with non-plastic wedges sandwiched at the neutral plane are shown, Fig.4. This sketch indicates that rolling deformation is complex and characteristically inhomogeneous.

Green and Wallace[58], after analysing theoretically the plastic wedge identified by Orowan, proposed a shear plane theory of hot rolling deformation in which all deformation takes place by shear strain along the

sides of a triangular rigid zone, Fig.5, developed under the arc of contact. The shear plane theory is a case of inhomogeneous deformation.

The short-comings of the use of metal inserts and bolts, or of grooves and lines placed on the surface of the material, to investigate material flow in rolling have been summarised by Underwood[59]. In addition, it is to be noted that all the techniques[52-57], from Hollenberg's[52] to even Orowan's[57], failed to identify where exactly within the material deformation is maximum and what effects the inhomogeneity of deformation has on structural evolution and the final properties of the worked material. Obviously, more work is needed in this area and this is taken up in the present research.

2.1.4.3 Plastic Deformation of Inclusions in Steel during Hot Rolling and the Concept of Plasticity Index

In the present work, type I MnS inclusions have been used as internal inserts for assessing the mode of plastic deformation during rolling. Therefore, the plastic deformation characteristics of MnS inclusions will be reviewed briefly against a background of the deformation behaviour of other inclusions (silicates and alumina) under hot working conditions.

The most important factors which govern the behaviour of an inclusion during hot working are: the nature, size, shape, composition, flow stress, and distribution of the inclusion; its plasticity relative to that of the steel matrix; the inclusion-matrix cohesion; and the hot working variables, namely, strain, strain rate, and temperature. Recently the influence of hydrostatic pressure has also been considered[60]. With respect to the nature of the inclusion, alumina inclusions are the most rigid inclusions in steel, being non-deformable at low and high hot working temperatures. In considering siliceous inclusions, it has been found[60,61] that, at low rolling temperatures, non-crystalline glassy silicates behave rigidly resulting in void formation while crystalline duplex silicates exhibit a brittle behaviour and may therefore crack into fragments which are subsequently rotated and disseminated. As the rolling temperature is increased, both silicate types undergo a transition from a non-plastic to a plastic state at some characteristic critical transition temperature. Relative to the alumina and siliceous inclusions, MnS inclusions are plastically deformable during hot working of steels.

There seems to be no known method as yet by which the absolute plasticity

of an inclusion phase, resulting from the deformation of the steel matrix, can be ascertained in situ. However, since the strength of an inclusion relative to that of the matrix crucially determines its behaviour within the steel, the plasticity of the inclusion can be assessed by evaluating the plasticity relative to that of the steel matrix. This concept was first applied by Unckel[62] to cold rolled, two-phase, alloys in which second-phase particles were imbedded. He defined a relative deformability factor, ν, also termed plasticity index,

$$\nu = \frac{\Delta h/h}{\Delta H/H} \qquad \text{----------(2)}$$

where Δh is the compression of the inclusion of original height h and ΔH the compression of the steel specimen of initial height H. Scheil and Schnell[63] carried out hot upset-forging of steels containing oxide and sulphide inclusions and assumed that each inclusion deformed into an ellipsoid from an initially spherical shape - a reasonable assumption but not likely to be strictly true at high matrix strains. They defined the plasticity index, ν, by

$$\nu = \frac{a/b}{A/B} \qquad \text{----------(3)}$$

where a and b are the major and minor axes respectively of the elliptical face obtained from a longitudinal section of the inclusion ellipsoid, A is the diameter of the compressed steel sample and B is its thickness. Pickering[61] investigated hot rolled steel samples and analysed his results in a more or less similar way[63] with the major modification that the deformation of the steel matrix, A/B, was defined by the relationship:

$$A/B = x_1^{3/2} / x_2^{3/2}$$

where x_1 is the original cross-section area of the steel ingot and x_2 the final cross-section area after rolling.

Malkiewicz and Rudnik[64] developed the above concepts in greater generality by deriving the following expression for ν:

$$\nu = \frac{\frac{2}{3} \ln \lambda}{\ln h} = \frac{\varepsilon_i}{\varepsilon_s} \qquad \text{----------(4)}$$

where λ is the inclusion aspect ratio, $\varepsilon_i = 2/3 \ln \lambda$ = the true strain on the inclusion, and $\varepsilon_s = \ln h$ = the true strain experienced by the steel matrix. As shown in Appendix 3, this relationship strictly applies

to ingot or rod rolling where a cylindrical state of strain exists, while under plane strain, as in strip rolling, it must be modified to the form:

$$\nu = \frac{\frac{1}{2} \ln \lambda}{\ln h} = \frac{\varepsilon_i}{\varepsilon_s} \quad \text{(Appendix 3)} \quad (5)$$

If $\nu = 0$, the inclusion does not deform at all; if $\nu = 1$, the inclusion deforms by an amount exactly equal to that of the steel matrix; and a value of $\nu > 1$ implies that the inclusion deforms more than the steel matrix. These are illustrated by detailed studies[65] of cavity formation in hot rolled steel which show that $\nu = 0$ leads to conical caps and hot tears, $\nu = 0.03 - 0.5$ results in fish tails with conical caps, $0.5 < \nu < 1.0$ gives a low frequency of microcracks, and when $\nu = 1$ the inclusion/matrix interface remains unbroken due to good cohesion with the matrix[66]. Chao et al[67] showed that MnS inclusions and steel have fairly similar deformation characteristics within a wide range of hot working conditions. Obviously, this behaviour will be influenced by the type of the MnS inclusion as well as the deformation variables.

Considering the MnS inclusion type, it has been shown[68,69] that the plastic deformation of MnS inclusions increases in the order: type I to II to III during hot working, probably due to the decreasing oxygen content from type I to type III. The MnS inclusion size is also important because small inclusions have been reported[61,64,68,69] to deform less than larger ones, possibly because of the large surface to volume ratio[68] of small inclusions which results in an excessively high energy[60,68] requirement to create a new interface as the inclusion deforms, and also probably due to inclusion rotation[60].

With respect to the influence of working variables, an increase in matrix strain generally decreases the relative plasticity of inclusions[60,61,68] and this has variously been attributed to: greater work-hardening index of the inclusion relative to the steel matrix[61]; excessive work-hardening of a narrow region of the matrix adjacent to the inclusions resulting in a protective hard shell around the inclusion[69]; and a reduction in the applied couple and hence the shear stress on the inclusion[60]. Strain rate and hydrostatic pressure have been reported[60] to be important as well. In a more general way, Bridgeman[70] has emphasised the importance of hydrostatic pressure in the plastic flow of Engineering materials.

2.1.4.4 The Kinematics of Homogeneous and Inhomogeneous Deformation during the Upset-forging of a Solid Cylinder

In upset-forging, as in rolling, plastic deformation may be categorised into homogeneous and inhomogeneous types. Ideally, when a solid cylinder of an isotropic and homogeneous material, with its height not exceeding 1.5 times its diameter, is being upset-forged between two rigid, parallel, frictionless platens, the applied force is uniformly distributed over the contact area, giving rise to pure compressive stresses with the radial and circumferential stresses both equal to zero. Thus every transverse cross-section of the cylindrical workpiece remains circular and increases in diameter at the same rate as every other cross-section. The circular ends slide freely outwards over the platens so that the initially vertical sides remain straight and vertical after the upsetting. The deformation process as described in this paragraph is a homogeneous deformation.

In the case of inhomogeneous upset-deformation, the expansion of the end regions of the deforming cylinder is restricted and the initially straight and vertical sides roll-out into a barrel-like shape, a phenomenon termed barrelling. This implies the setting up of severe hoop strains and stresses on the outer fibre which may cause cracking. The barrelling phenomenon is customarily attributed solely to tool/workpiece interface friction and thus has been utilised by several workers[71-79] for friction studies. The contribution of temperature variations to the barrelling, particularly in hot upset-forging seems not to have been considered in published literature. This will be considered in the present work.

2.1.4.5 Methods Suggested for Producing Homogeneous Deformation in the Upset-forging of a Solid Cylinder

The earliest reported attempt for obtaining homogeneous deformation in upsetting was due to Rummel[80] and was repeated by Meyer and Nehl[81]. This is illustrated schematically in figure 6. Essentially, the technique consisted of sandwiching the specimen, M, between two other blocks, P, both of which are of the same material and diamter as M. When the composite block was deformed, M was claimed to have undergone homogeneous deformation. Siebel and Pomp[82] used conical platens, figure 7, the base angle of the cone being equal to the friction angle, and machined conical craters into the ends of the specimen. They believed that the resulting unbarrelled upset sample was homogeneously deformed.

Cook and Larke[83] tackled the problem by deforming four cylinders of initial height to diameter (H/D) ratios = 0.5, 1.0, 2.0, 3.0 and from their stress-strain surves, they suggested that by extrapolation, a stress-strain curve corresponding to a height to diameter ratio of zero could be found and such a curve would be unaffected by inhomogeneity of deformation. Interpreting Cook and Larke's curves at low strains as indicating that plastic deformation remains homogeneous until a 25% height reduction has been exceeded, Polakowski[84] proposed remachining the cylinder to its original proportions after every 25% height reduction until the required final reduction in height had been achieved. In their search for homogeneous deformation, Taylor and Quinney[85] took out and relubricated the specimen over 30 times for only a reduction of ~36%!

As discussed in Section 5.1.2 later, each of the methods outlined above has its serious shortcomings. A more realistic and satisfactory approach to the elimination of inhomogeneous deformation during hot upsetting would seem to lie in eliminating both temperature variations and interface friction, the later being achieved through effective lubrication.

2.1.4.6 Lubrication in Hot Upsetting

The technique of effective lubrication recommended in the previous section has been utilised in the present research to eliminate inhomogeneity of deformation during hot upsetting. It is therefore relevant to examine, briefly, certain fundamental aspects of lubrication, with particular reference to the hot upset-forging process.

In general, lubrication may be divided into two types, namely, hydrodynamic lubrication during which the lubricant develops dynamic fluid pressures, and boundary-sliding lubrication in which the lubricant simply cushions the 'slide-face' into a 'low-friction' or 'frictionless' interface. If the lubricated surfaces suffer only elastic deformation, the lubrication mechanism is termed elasto-hydrodynamic or elasto-boundary sliding while if any of the surfaces deforms plastically, the lubrication mechanism operating becomes either plasto-hydrodynamic or plasto-boundary-sliding. In practice, both the elasto- and the plasto-lubrication mechanisms often exist together although one mechanism may be more dominant.

The lubricants used for plastic deformation may be grouped into water-based , oil-based, grease-based, and solid lubricants. The water-based

lubricants, usually in the form of aqueous solutions, emulsions, or dispersions of soaps and fatty acids with the addition of fillers, may be advantageous where cooling is required. Oil-based lubricants are normally in the form of light mineral or compound heavy oil, containing one or more additives such as graphite, molybdenum disulphide, mica and clay. Greases are basically oils containing thickening agents to make them semi-solid. Solid lubricants are either organic or inorganic solids, the more widely known being graphite although molybdenum disulphide, basalt, and glass may be used in special applications. The mode of application of the lubricant largely depends on its nature.

Water-based and oil-based lubricants are generally brushed onto, or sprayed on the platens, while grease-based lubricants are normally brushed onto the dies prior to the forging action. Solid lubricants are normally applied by sprinkling them on the bottom die (platen) and on the upper end face of the specimen just prior to the deformation[77]. If the lubricant forms a viscous squeeze film during the deformation, the specimen end faces are generally grooved for lubricant trapping. In this connection, Loizon and Sims[86] used concentric circular grooves of 0.02 mm depth placed at very close, regularly fixed, intervals; and Suzuki et al[87] employed troughs which were formed by using lips on the periphery of the specimen end faces.

2.1.4.7 Properties of a Good Hot Deformation Lubricant and the Influence of Working Variables

The properties of an ideal hot working lubricant have been extensively discussed[74, 88-90]. Not surprisingly, no one lubricant has all the properties associated with the ideal lubricant. However, glass meets most of the more important requirements and is particularly attractive for hot working[88,91] because: it is one of the best known thermal insulators and so will be expected to minimise heat losses from the specimen as well as thermal fluctuations of the dies; it has good viscosity which varies only slightly with temperature even up to ~1280°C; it has a very low friction coefficient, reported values in extrusion being 0.04[92] and 0.01[91], a value as low as 0.001 having also been reported[88]; it forms a viscous film which does not easily break down under high pressures if suitably trapped; and it is inexpensive when compared with grease or graphite, the price differential being mainly because lubricating glass is usually made from scrap glass.

Sejournet[88,92] pointed out that proper lubrication using glass is

impossible in the presence of scale because the debris formed by scale promotes local breakdown of the glass film. An increase in strain rate has been observed[77,78,93] to increase the effectiveness of squeeze film lubricants probably because of increased hydrodynamic action. Direct information about the effects of other processing variables, such as, material composition, strain, temperature and deformation sequence seem to be lacking. Some aspects of this will be considered in the present research.

2.1.5 STRAIN RATE

2.1.5.1 Strain Rate Distribution and Evaluation in the Rolling Process

In rolling, the strain rate, $\dot{\varepsilon}$, varies considerably within the deformation zone, figures 8a[59] and 8b[94], being a maximum at the entry plane and decreasing along the arc of contact, until a value of zero is attained at the exit plane. As the thickness of the rolled material decreases, the strain rate generally increases (figures 8a and b) and under certain conditions may exhibit a maximum point, figure 8a.

One of the earliest relationships for evaluating strain rate, $\dot{\varepsilon}$, both for homogeneous and inhomogeneous deformation was Ekelund's relationship[46]:-

$$\dot{\varepsilon} = \frac{h_1 - h_2}{\frac{1}{2}(h_1 + h_2)} \cdot \frac{1}{t_c} \qquad \text{(6)}$$

where h_1 and h_2 are the initial and final heights respectively of the sample, t_c is the contact time defined as the time in seconds for a point on the roll surface to pass from the plane of entry to the plane of exit. This definition of t_c implies a sticking friction assumption and so, for a roll of radius R, and peripheral speed V, t_c will be given by:-

$$t_c = \frac{[R(h_1 - h_2)]^{\frac{1}{2}}}{V} \qquad \text{(7)}$$

Larke[94] pointed out more specifically the need to resort to a mean strain rate, $\bar{\dot{\varepsilon}}$, in order to take account of the considerable variation of strain rate values along the arc of contact. He then developed two relationships, one for full sticking friction, given by:

$$\bar{\dot{\varepsilon}} = \frac{V}{[R(h_1 - h_2)]^{\frac{1}{2}}} \cdot \ln \frac{h_1}{h_2} \qquad \text{(8)}$$

and the other for full slipping friction, viz:-

$$\dot{\bar{\varepsilon}} = \frac{V h_\alpha \cos\alpha}{h_1 h_2} \cdot \left[\frac{h_1 - h_2}{R}\right]^{\frac{1}{2}} \quad \text{---------- (9)}$$

where h_α is the thickness of the bar at the neutral plane and α the angle between the neutral plane and the plane of exit.

For a given reduction, calculated values of $\dot{\bar{\varepsilon}}$ based on sticking friction assumptions are generally higher than those based on slipping friction assumptions. The maximum difference between the two occurs at the plane of entry and reduces to zero at the exit plane. This effect is less pronounced for thicker sections such as slab than for thin materials such as strip, figure 8b. It must also be noted that in industrial hot rolling, μ = ~0.4, and so neither full sticking nor full slipping actually occurs.

2.1.5.2 Strain Rate Variation and Evaluation in the Upsetting Process

During hot cylinder upset-forging, strain rate variation generally occurs as the deformation progresses. If a constant strain rate is desired, the cam plastometer, designed by Orowan[95], which has a cam with a logarithmic profile, may be used.

No standard relationship seems to have been developed for evaluating $\dot{\varepsilon}$ in the upsetting process. Thus for any upsetting operation, $\dot{\varepsilon}$ is best evaluated from first principles, using the basic definition:

$$\dot{\varepsilon} = \frac{d\varepsilon}{dt} = \frac{V}{h} \quad \text{---------- (10)}$$

where h is the instantaneous height of the sample and V the deformation velocity.

The sensitivities of dynamic flow stress and dynamic microstructural processes to strain rate during hot deformation are reviewed in Section 2.3.2.

2.2 STRUCTURAL CHANGES AND THEIR EVOLUTION DURING HIGH TEMPERATURE THERMO-MECHANICAL WORKING

2.2.1 Dynamic Structural Changes and Evolution

2.2.1.1 Substructure Development

Deformation during thermo-mechanical processing introduces defects,

predominantly dislocations, and to lesser extents, lattice vacancies and stacking faults. In general, the dislocations increase rapidly at first with strain, becoming entangled and forming a cellular structure. Then more gradually, the dislocation tangles accumulate into walls separating regions of low dislocation density[96], the cells decreasing in size and also becoming more sharply defined[97] as the strain continues to increase. Ultimately, a steady state is attained at which the dislocation density ρ, as well as the cell size d, may be presumed to remain constant. Theoretical considerations[98-101] indicate that ρ is uniquely related to the flow stress σ, in the steady state by a relationship of the form:

$$\sigma = \sigma_o + \alpha\mu b\rho^{\frac{1}{2}} \quad \text{---------- (11)}$$

where σ_o is a friction stress which often approximates to zero, α is a geometrical constant which approximates to unity, μ is the shear modulus, and b the Burgers vector. Similarly, d has been related[102-105] to σ in the hot working range of strain rates by:-

$$\sigma = \sigma_o + Kd^{-m} \quad \text{---------- (12)}$$

where σ_o is normally zero[105], K a constant and m also a constant of ~1.5 in value. At a higher strain rate, the strain to the steady state becomes larger and the substructure developed finer.

Several workers[106-110] have shown that the dislocations generally form a closely-knit, three-dimensional, network, the average spacing of which increases with decreasing stress but decreases with alloying additions at the same stress[109]. Decreasing the stacking fault energy increases the dislocation density while decreasing the sharpness of the cell walls. Thus in metals with high stacking fault energies, such as aluminium and α-iron, the subgrains (cell walls) are well formed and sharply defined, the boundaries being simple arrays[111], while in metals with low stacking fault energies, such as austenitic stainless steel[112] and α-brass[113], the substructures are highly tangled[114], forming irregular forests[112]. Solute atoms often decrease the stacking fault energy and so the observed[115-117] decrease in cell size with increasing solute atom concentration may well be due to this decrease in stacking fault energy. However, recent investigations with aluminium[118], iron[119,120], copper[121] and nickel[122] indicate that, regardless of

the stacking fault energy value, increasing the solute content of an alloy inherently increases the dislocation density thus reducing the sharpness and size of the substructure developed.

Dispersed second-phase particles create dislocation sources[104] and provide barriers to dislocation movement. They also influence the type and size of the substructure developed by the plastic deformation, the extent of this influence being largely determined by the particle size and spacing. For instance, it has been observed[114] in steels containing carbide particles that, for a given set of deformation parameters, the cell size becomes finer as the inter-particle spacing of the carbides decreases. Though it has been reported[123] that the cell size is independent of the initial grain size, there is evidence to show that, for a given strain, the dislocation density in iron[124] and copper[123] increases as the initial grain size decreases. The influence of decreasing the temperature upon substructure has been reported[123,125] to be similar to the effect of increasing strain rate: that is, the dislocation density increases and the cell size becomes ill-defined and finer. In particular, studies on iron[126] indicate that raising the deformation temperature increases the cell size. As a rule, those factors which decrease the dislocation spacing also decrease both the size and the sharpness of the substructures.

Observations by several workers suggest that mechanical properties such as yield strength, hardness[105,127,128] and micro-hardness[129] are related to substructure size (d) by a relationship of the form:-

$$P = P_o + K(d)^{-\frac{1}{2}} \quad \text{---------- (13)}$$

where P is the property of interest while P_o and K are constants.

Although mechanical property improvement by substructure refinement and preservation is not normally encountered in steel processing, it is a widely utilised technique in the processing of nickel-thoria alloys[130,131] where stabilisation of the dislocation density is achieved by thoria particles so that its contribution to strength even at high temperatures is quite significant.

2.2.1.2 Dynamic Recovery

Dynamic recovery is a microstructural restoration process which operates

while the deformation is taking place. It involves dislocation climb, node detachment, and cross-slip leading to polygonisation during which dislocations of opposite signs annihilate each other while those of the same sign are rearranged to form walls. In high stacking fault energy materials, notably aluminium[132], the dislocation climb, glide and cross-slip proceed unimpaired and so dynamic recovery occurs quite readily while in low stacking fault energy materials such as austenitic iron[132], the tangled nature of the substructures developed (section 2.2.1.1) make climb, glide and node unpinning difficult thus confining the dislocations to their original slip planes and rendering the dynamic recovery difficult. Dynamic recovery requires no incubation time and does not involve the formation of new grains. It is inhibited by solute atoms from alloying additions while itself it inhibits dynamic recrystallisation by reducing the energy available for the latter to occur.

A consideration of the various theories[106,107,133-135] suggested for dynamic recovery falls outside the scope of the present work. Jonas et al[111] have carried out an extensive review of the theories, highlighting their inadequacies.

2.2.1.3 Dynamic Recrystallisation

Dynamic recrystallisation, like dynamic recovery, is a softening process which operates while the deformation is taking place. It differs from dynamic recovery in that it involves the nucleation of new strain-free grains. Although there is no unanimity in classifying materials into clear-cut groups of those which undergo dynamic recrystallisation and those which do not, especially at high strains, materials with low stacking fault energies tend to recrystallise dynamically more readily. Such materials, in ascending order of difficulty to recrystallise dynamically, include lead, gold, silver, copper, nickel and austenitic iron. These metals generally have low recovery rates which in turn give rise to dense dislocation substructures which promote the nucleation of dynamic recrystallisation. In general, high strains are needed to initiate dynamic recrystallisation. Luton and Sellars[136] and Roberts[21] have suggested that the critical strain (ε_c) with an associated critical stress (σ_c) at which dynamic recrystallisation starts, occurs prior to the strain (ε_p) at the peak stress (σ_p) (see Section 2.3.1 and figure 13b). Solute atoms retard dynamic recrystallisation due to their drag effect on migrating grain boundaries and this explains why α-iron of standard purity does not recrystallise dynamically while vacuum melted, zone-

refined α-iron[137] does.

It should be noted that with the exception of a few materials such as α-iron[132] and aluminium[132] in which dynamic recovery operates exclusively at both low and high strains, dynamic recovery and dynamic recrystallisation normally occur simultaneously at high strains in most common metals and alloys.

Evidence for the occurrence and non-occurrence of dynamic recrystallisation are varied and not always unambiguous. The observation of bent annealing twins[111] and dislocations[114,138,139] in recrystallised grains has been used to support arguments for the occurrence of dynamic recrystallisation. Acceleration of the creep rate[140,141] in lead has been claimed to indicate the occurrence of dynamic recrystallisation, the acceleration being attributed[141] to the primary creep of the new (dynamic) grains. Luton and Sellars[136] suggested that the oscillatory shape of the flow curve obtained at low strain rates in hot working provides evidence for dynamic recrystallisation. They reasoned that work-hardening continues to occur until the critical strain (ε_c) is reached where new grains form. This is then followed by alternate cycles of recrystallisation and strain hardening, thus accounting for the oscillatory shape of the stress-strain curve.

Among the techniques employed to disprove the occurrence of dynamic recrystallisation is the texture technique. From their observations that the texture developed in hot-worked copper (deformed in torsion at 300°C and 500°C) was similar to that developed during room temperature deformation, Drube and Stüwe[114] postulated that dynamic recrystallisation is impossible in copper, a view quite contrary to the popular belief that copper undergoes dynamic recrystallisation readily[132,142]. Their[114] conclusion was based on the fact that when cold worked copper is annealed its deformation texture changes as a result of recrystallisation. Thus, they[114] argued that if hot worked copper underwent dynamic recrystallisation, its deformation texture should not have resembled that of cold worked copper. However, the similarity in the texture of hot and cold worked copper might well be due to differences in the mechanisms which govern dynamic recrystallisation and static recrystallisation. For instance, no differences in texture will be expected if dynamic recrystallisation is solely controlled by grain boundary migration.

The observation that nucleation of dynamic recrystallisation occurs predominantly at prior γ-grain boundaries[143-145], albeit intragranular nucleation[144] has been reported, has led to the suggestion that the mechanism for the nucleation is strain induced grain boundary migration. This mechanism essentially requires that local regions of the boundary should be pinned at their periphery to allow boundary bulging to occur. McQueen and Bergerson[146] suggested that if the strain is suitably high, some substructure tangles build up into high misorientations resulting in nucleation of new strain-free grains, the density of the nuclei being highest at grain boundaries where strains are locally highest. Gifkins[147] attributed dynamic recrystallisation during creep of high purity lead at 100°C to a sub-grain growth mechanism in which the dynamic nuclei form at grain boundaries with the greatest misorientations and which do not migrate during the deformation. During hot torsion deformation of stainless steel at 1175°C, Nicholson[148] observed dynamically formed grains at both grain boundaries and within the deformed grains and he attributed the formation of the intragranular grains to a subgrain coalescence mechanism which involves subgrain rotations (section 2.2.3.2.5). It would appear from these observations[143-148] that there is yet no unanimity as to the mechanism governing dynamic recrystallisation.

Studies of the dynamically recrystallised grain size are scarce. Results of the limited investigations[143,144,149] available indicate that the refinement of the dynamically recrystallised grain size, d, with increasing flow stress σ, can be quantitatively correlated by a proportional relationship of the form

$$\sigma \propto d^{-n} \quad \text{---------- (14)}$$

2.2.2 METADYNAMIC STRUCTURAL CHANGES

Metadynamic, also called post-dynamic, recrystallisation is a microstructural restoration mechanism, first recognised by Djaic and Jonas[150] for which, unlike all the other restoration processes, there exists no parallel in the annealing of cold worked materials. It occurs only after some previous dynamic recrystallisation has taken place and so a heavy reduction is necessary for its occurrence. Djaic and Jonas[150] reported that while classical recrystallisation requires an incubation period, metadynamic recrystallisation does not. This is to be expected on account of the pre-existing dynamic nuclei and the high strain with the associated high driving force.

The technological importance of metadynamic micro-structural processes has not yet been appreciated and even laboratory investigations are difficult to come across in published literature. This is probably because of the zero incubation time which renders its direct observation difficult. If the suggestion [151] that metadynamic grains are finer than dynamic grains at relatively low temperatures and coarser at high temperatures can be unequivocally established, an important contribution towards understanding of the mechanisms governing grain size heterogeneities in hot worked products may have been made.

2.2.3 STATIC STRUCTURAL CHANGES

2.2.3.1 Static Recovery

Static recovery is the microstructural modification process involving a more orderly arrangement of substructures [127] and removal of vacancies and dislocations without any new grains nucleating. No incubation period is required and so it starts to operate as soon as the applied forces are removed, the rate decreasing as the process proceeds. The driving force arises from the internal energy associated with the mechanical deformation.

In general, the rate of static recovery is increased and the time available for the recovery to occur before the onset of primary recrystallisation is decreased by an increase in temperature, strain, and strain rate. However, Capeletti et al [152] found that, for type 304 stainless steel, static recovery is temperature independent. Increasing the stacking fault energy increases the rate of static recovery because dislocation rearrangement processes, particularly climb, occur more readily. Solute atoms from alloying additions retard static recovery probably due to solute drag effect on dislocations and/or a decrease in stacking fault energy. Precipitate particles, particularly when present on dislocation networks, retard static recovery. Petkovic et al [153] found that 0.07% Nb drastically retarded static recovery in plain carbon steel. They attributed this effect partly to the solute effect of niobium in solution decreasing the stacking fault energy and partly to the precipitation of niobium carbonitride particles on dislocation networks.

The occurrence of static recovery in hot working may normally be detected by changes in mechanical properties, particularly hardness and flow stress. In this connection, Kozasu and Shimizu [154] inferred the occurrence of static recovery in austenitic stainless steel from the decrease

in hardness of a series of rapidly quenched samples. The pitfall of this technique is that it cannot be used for steels which undergo $\gamma \rightarrow \alpha$ transformation on cooling[152] and in such situations a flow stress method is used[150]. In this technique, specimens are annealed for different times after the first deformation and then deformed again. Small changes in peak stress indicate static recovery while much larger changes indicate static recrystallisation.

It is traditionally believed that static recrystallisation starts only after static recovery has ceased. However, evidence for simultaneous occurrence of static recovery and static recrystallisation has been obtained[142,155] from results of studies of the rate of stored energy release[142] and changes in microhardness[155] upon annealing of cold worked high-purity aluminium. A similar simultaneous recovery and recrystallisation will be expected in hot working.

2.2.3.2 Static Recrystallisation

Static recrystallisation, also termed primary recrystallisation, requires for its occurrence, a minimum strain which varies from 5-10% reduction, and an incubation period. Basically, the process involves the nucleation of new strain-free grains and the growth of these new grains at the expense of the deformed matrix. Therefore, it can be satisfactorily described in terms of nucleation and growth.

2.2.3.2.1 Nucleation and Various Nucleation Theories

Nucleation for static recrystallisation in hot working has not been extensively studied. However, it is believed that the mechanisms which operate during the primary recrystallisation of cold worked material upon annealing also operate during static recrystallisation of hot worked material. In this context, four major nucleation theories have been proposed.[109,156-165]. The essential aspects of these theories will now be briefly examined and other models[170-173] of lesser significance will also be noted.

2.2.3.2.2 The Classical Nucleation Theory

The classical theory, traditionally applied to conventional phase transformations[157,174] was first successfully applied to nucleation of recrystallisation in plastically deformed material by Burke and Turnbull[156]. Essentially, the theory defines a critical radius (r_c) of an embryo by:

$$r_c = -\frac{2\gamma}{Z} \qquad \text{---------- (15)}$$

where γ is the specific interfacial energy and Z the strain energy of the deformed material. Any strain-free region which develops into an embryo of radius equal to or greater than this critical value becomes a viable nucleus and so grows into the matrix. On the other hand, if the embryo has a sub-critical radius, it is destroyed. The time lapse for the viable nucleus to develop accounts for the incubation time observed experimentally. Thus the classical theory provides explanation for incubation time during static recrystallisation. Predicted[156] values of nucleation frequency and minimum size of a viable nucleus from the theory are also in reasonable accord with experimental values. Furthermore, the theory explains preferential nucleation at severely deformed regions of the material.

However, the theory predicts low misfit angles between the new strain-free grains and the deformed matrix while in practice the orientation of the new grains are significantly different from those of the matrix. Also, it predicts rather too high[175] an amount of local deformation in order to produce a viable nucleus. Furthermore, Byrne[175] pointed out that the classical theory does not take into account impurities which are important in recrystallisation.

2.2.3.2.3 The Strain-Induced Boundary Migration Mechanism

Strain-induced grain boundary migration[158-162] was first observed by Beck and Sperry[158] in cold worked high-purity aluminium, then by Bailey[159] and later developed in greater generality by Bailey and Hirsch[160]. Beck and Sperry[158] postulated that a high misorientation across the boundary between two grains A and B (Fig. 9) as a result of deformation leads to a high mobility of the boundary. Grain B which has smaller subgrains is more deformed than grain A, Fig. 9b, and the difference in stored energy resulting from this strain difference provides the driving force for the process. The migration initiates at a zone such as s (Fig. 9b) which corresponds to that part of the grain boundary length that forms a common boundary with one of the large subgrains in the less deformed grain A. The direction of the migration was believed by them to be away from the less deformed grain into the more heavily deformed one, Fig. 9c.

Bailey[159] offered an alternative explanation by postulating that a grain boundary segment of length 2L may bulge out into a spherical cap of radius R, Fig. 10, and that this cap will grow into a viable recrystallisation nucleus if

$$L > \frac{2S}{\Delta E} \qquad (16)$$

where S is the surface energy of the migrating boundary and ΔE the difference in stored energy, per unit volume, across the boundary. The growth stages are 1→2→3, fig. 10. In a later detailed analysis of the model, Bailey and Hirsch[160] showed that the growth rate passes through a minimum when $\alpha = 180°$ and that predictions from the model are generally in accord with the normal kinetics of recrystallisation.

Using kinetic experiments, Beck[176] later indicated that no incubation period is involved in this mechanism probably because no nucleus of a new orientation has to be formed.

2.2.3.2.4 The Subgrain Growth Mechanism

The subgrain growth model was proposed by Cahn[163] and Beck[177]. They postulated that some of the strain free cells which are produced by polygonisation in regions of high lattice curvature, where the rate of increase of boundary misorientation is greatest, grow by migration into their immediate surroundings. As these subgrain boundaries migrate, they absorb dislocations in their path, thus further increasing their boundary misorientations relative to their neighbouring sub-boundaries. When the interface of a subgrain with the matrix attains a high angle boundary misorientation, that subgrain becomes a viable nucleus for recrystallisation. The time required to form the viable nucleus accounts for the incubation period[161]. Also, observation of recrystallisation at preferential sites, particularly where strains are highest is well accounted for by this model. The reduction in strain energy, that is, the difference between the decrease in volume free energy and the increase in surface free energy, provides the driving force for the process.

2.2.3.2.5 The Sub-Grain Coalescence Model

After analysing the results of recrystallisation studies in 3% silicon-iron single crystals[167,178], Hu[166,168] believed that subgrain growth occurs by coalescence rather than by sub-boundary migration. According to the coalescence mechanism, the disappearance of dislocations, probably by climb, from the boundary of any two adjacent subgrains and the diffusion of atoms along the boundary, will cause one of the subgrains to rotate relative to the other. This rotation continues until the lattices of the two subgrains coincide. Continued constant adjustment of the boundary geometry of the coalesced subgrain ultimately results in the formation of a single viable nucleus for recrystallisation. The driving force for the process is believed to come from the difference between the high energy of dislocations

in a low-angle boundary and the lower energy associated with a high-angle boundary.

There are reports that nucleation by subgrain coalescence has been observed experimentally in silicon iron[167,169], low carbon steel[179] and aluminium alloys[180]. Li[181] examined theoretically the energetic factors and the possible kinetic processes involved in sub-grain coalescence. He showed that a sub-grain rotates naturally in such a direction that low angle boundaries decrease their angles of misfit to allow high-angle boundaries to increase theirs. Further, he indicated that, depending on the misfit angle of the boundary, either the co-operative movement of dislocations in the boundary or the co-operative diffusion of vacancies in the lattice, is the rate controlling process. However, Li's theoretical analysis[181] predicts a considerably slower rate of subgrain development than the rate observed experimentally[182].

2.2.3.2.6 Other Nucleation Models

One of the earliest nucleation theories was the block nucleation theory proposed by Burgers[183]. It assumes that blocks of low and high energies which pre-exist inside the deformed matrix ultimately become viable nuclei for recrystallisation. Lack of experimental evidence for this mechanism led to its rejection. Nielson[171] proposed a geometric coalescence model which stipulates that any two adjacent subgrains having similar orientations may coalesce, each retaining its orientation in the coalesced state. In addition to the theory predicting too large a subgrain for the formation of a viable nucleus, it is not supported by practical observations in that, in practice, coalesced subgrains have the same orientation. Davies et al[172] have suggested that ledges developed on grain boundaries cause the boundaries to migrate; and King and Smith[173] have proposed that the formation of a bulge on the grain boundary for boundary migration is due to the separation of grain boundary dislocations with steps at their cores. These models[172,173] require further elucidation.

Burgers and Verbraak[170] and Verbraak[184] proposed a Martensitic nucleation model which they used to account for the cube texture produced when heavily strained copper is annealed. This model stipulates that a nucleus completely bounded by high angle interfaces is spontaneously produced by a quasi-martensitic shear within a small volume of the deformed lattice. So far, there is no metallographic evidence in support of this mechanism.

2.2.3.2.7 Particular Case of Nucleation in Hot Deformation

Metallographic observation of bowed grain boundaries has been reported[127] as evidence for nucleation by a strain-induced boundary migration mechanism in the hot deformation of aluminium. Experimental observation of nucleation by subgrain growth has been reported in hot worked aluminium[127]. During hot deformation of stainless steels, Nicholson[148] attributed experimentally observed nucleation of recrystallisation at grain boundaries to a strain-induced boundary migration mechanism while nucleation found within the grains was attributed to the subgrain coalescence mechanism.

Considering nucleation sites, recrystallisation nuclei have been observed to occur preferentially at grain boundaries after hot deformation of types 304 and 316 austenitic stainless steel[185], molybdenum-containing austenitic stainless steel[186], α-iron and aluminium[127]. It may therefore be concluded that nucleation of recrystallisation after hot working occurs by similar mechanisms to those which lead to nucleation when cold-worked material is annealed.

2.2.3.2.8 Growth of Recrystallisation Nuclei by Boundary Migration

A viable recrystallisation nucleus is bounded by high angle boundaries. A high angle boundary, defined by Aust and Rutter[187] as the interface along which two crystals of different orientations are joined, is very mobile and so the nucleus grows into a strain-free, equiaxed, recrystallised grain by boundary migration. Theoretical prediction of the mechanisms involved in high-angle boundary migration necessarily requires intimate knowledge of the atomistic nature and structure of such boundaries. In this connection, various models have been proposed to describe grain boundary structure. Notable among these are the super-cooled liquid model[188, 189], the island model[190,191], and the coincident-site model[192,193]. Based on these models, theories of grain boundary migration rate have been suggested. Mott[190] proposed the first theory which was later developed in a more acceptable form by Turnbull[194].

Mott's theory, referred to as group process theory, assumes the "island" structure of a grain boundary in which the grain boundary merely consists of islands of alternate good fit and misfit between the grains. Atoms are activated in groups during the transfer process across the boundary and the basic transfer process involves the melting of a group of atoms which belong to one crystal and the transfer of these to the other crystal(the growing

grain) where they re-solidify. Turnbull[194] suggested an alternative mechanism which is similarly based on Mott's absolute reaction rate theory, but which assumes that atoms are transferred singly across the migrating boundary to the recrystallising grain. This theory[194] is referred to as "the single process theory"[195,196]. In the theory[194], Turnbull assumed that each stom has to overcome an activation entropy barrier (ΔS_a) in crossing the boundary. If ΔF is the driving force and ν the frequency of atomic jumps, then the grain boundary migration rate, G, as given by Turnbull, is:

$$G = \frac{e\nu b}{KT}.\Delta F \exp\left(\frac{\Delta S_a}{R}\right) \exp\left(-\frac{Qg}{RT}\right) \quad \text{---------- (17)}$$

where e is the base of natural logarithms, b the local movement of the grain boundary by the transfer of one atom, K the Boltzmann constant, T the temperature in Kelvin, R the Universal gas constant, and Qg the activation energy (per mole) for the growth process. The frequency ν may be replaced by (KT)/h in reaction rate theory, h being Planck's constant. Usually, $\Delta S_a \ll R$ and so equation (17) reduces to:

$$G = G_o \exp\left(-\frac{Qg}{RT}\right) \quad \text{---------- (18)}$$

where $G_o = \frac{e\nu b}{KT}.\Delta F$

The single process theory has been generally accepted[187,197] for describing migration kinetics, particularly in pure metals[198]. There has been no sound theoretical justification for the group theory[197].

2.2.3.2.9 Effects of Solute Atoms on the High-Angle Boundary Migration Rate

Impurities tend to segregate preferentially to grain boundaries and have the general effect of reducing the boundary energy. Thus the activation energy for growth, Qg, which is generally close to that for boundary self-diffusion[199] in pure metals, has been observed[200] to be different to the boundary self-diffusion value when impurities are present and solute boundary interaction occurs. Since the Turnbull's single process theory does not take impurities into account, its predictions differ from experimental results[198]. Among the various theories subsequently proposed to take impurities into account is the Lucke and Detert[200] theory.

The Lucke and Detert theory assumes that the solute-boundary interaction is elastic in nature with the boundary acting as an energy sink for solute atoms. The theory stipulates that at high impurity concentrations

or at low temperatures, the migrating boundaries are held back by the solute atoms; thus the rate of diffusion of impurity atoms behind the boundary controls the boundary migration rate. In this case, activation energy for boundary migration is close to that for volume diffusion of the solute atoms. On the other hand, if the impurity concentration is low or the temperature is high, the impurity atmosphere "boils off" from the boundary, leaving it to migrate independently of the solute atoms. Under these conditions, the activation energy should be close to that for boundary self-diffusion as in pure metals.

Gordon and Vandermeer[201] modified the basic migration rate relationship developed by Lucke and Detert[200] to reflect their own[201] interpretation of the nature of the lattice in which the foreign atoms migrate. Lucke and Stüwe[202] re-interpreted Lucke and Detert's theory more rigorously by considering the influence of large solute concentrations. Cahn[203] accepted Lucke and Detert's basic theory of impurity-controlled boundary migration with diffusion occurring normal to the boundary. He then considered the detailed nature of the diffusion of atoms in the potential field of the boundary by depicting the migrating boundary as a moving, one-dimensional, potential well in an infinite medium. The massive amount of data which would be needed to validate Cahn's theory[203] experimentally has probably limited its discussion so far to only theoretical[197] analysis.

Li[189] proposed a theory basically different from Lucke and Detert's by assuming that solute atoms segregate to the boundary to reduce the porosity and hence the migration rate of the boundary. Abrahamson and Blakeney[204], and subsequently Abrahamson[205,206], suggested that electronic interactions, either between solute and solvent atoms, or between solute atoms and grain boundaries, have a greater influence on boundary migration than elastic interactions, particularly in transition metals. Disappointingly, this theory is entirely qualitative.

After evaluating all available evidence, one may reasonably conclude that, with appropriate modifications, the Lucke and Detert[200] theory can adequately describe the grain boundary migration kinetics during the growth stage of viable recrystallisation nuclei. However, very rigorous analyses of the nature, structure and behaviour of grain boundaries have recently been presented by several authors in a recent conference[207], and a symposium[208], on Grain Boundary Structure and these provide new bases for further research into boundary migration kinetics.

2.2.3.2.10 Formal Recrystallisation Kinetics

Johnson and Mehl[209] and Avrami[210] were the first to present a formal Mathematical treatment of recrystallisation kinetics as a nucleation and growth process. The initial work[209,210] was later refined by Avrami[211,212]. Essentially, the derivation starts with the basic relationship,

$$v = f.G_x G_y G_z (t - t_o)^3 \quad \text{---------- (19)}$$

where v is the volume of a new grain formed at time t, measured from the origin; G_x, G_y, G_z are the growth rates in the x, y, z directions respectively; f is a shape factor; and t_o is the incubation time. As the growth process goes on, new nuclei form and proceed to grow as well. If d_n is the number of nuclei formed in a time interval dt before impingement occurs, then the volume fraction, X, is related to the nucleation density $\dot{N}$ by

$$d_n = \dot{N}(1 - X)dt \quad \text{---------- (20)}$$

Johnson and Mehl's major contribution[209] to the derivation was the introduction of the concept of an extended volume fraction in order to take into account the "ghost nuclei" which would have formed if impingement had not occurred and new grains had continued to nucleate everywhere in the sample including the recrystallised volume. However, the three equations ultimately derived by Johnson and Mehl to describe the three limiting conditions, namely, three-, two-, and one-dimensional recrystallisation, which would exist if t_o is negligibly small and $\dot{N}$ does not vary with t, were very complex. Avrami avoided this complex treatment by making a more stringent allowance for the "ghost nuclei". He arrived at the more popularly known relationship:

$$1 - X = \exp(-Bt^k) \quad \text{---------- (21)}$$

where B and k are constants, with k taking a value of 4 for three-dimensional recrystallisation.

The analyses presented above assume that nucleation occurs randomly in the material at a constant rate. Although Cahn[213] assumed also that nucleation and growth rates are constant and that growth is isotropic, he considered preferential nucleation at grain boundaries, grain edges, and grain corners. Cahn's equations were very complex but could be put in the form of equation 21. The k-value predicted by his equations prior to site saturation agrees with that predicted by Avrami's equation, although lower values are obtained[213] after site saturation. Sandström and Lagneborg[214] derived a model quite similar to the Avrami's equation

although they took into account prior occurrence of recovery (dynamic or static), dynamic recrystallisation, and metadynamic recrystallisation.

It would therefore appear from the available evidence that Avrami's equation can be used for accurate fitting of experimental data, albeit subsequent analyses[213,214] seem to be more realistic. Using Avrami's equation, Roberts and Ahlblom[149] found that, for a number of micro-alloyed and stainless steels tested over a wide range of temperatures, strains, and strain rates, k varies from 0.8 to 1.3 only. From these results, they concluded that k is independent of deformation variables and dependent only on nucleation mode and hence nucleation sites. On the other hand, Le Bon et al[24] reported values of k = 1 to 2 for hot deformed 0.17%C/1.36%Mn steel. The wide variation in this case suggests that k depends on the hot deformation variables. Wusatowski[215] found that k decreases with increasing strain in hot rolling of austenitic stainless steels between 900°C and 1100°C. Towle and Gladman[185] observed a temperature effect. In general the practical significance of k in terms of its dependence on working variables is presently ill-understood.

2.2.3.3 Effects of Variables on Static Recrystallisation Kinetics

2.2.3.3.1 Effects of Prior γ-Grain Size and Reheating Temperature

The precise relationship between incubation time and prior γ-grain size is not clear. However, it has been observed that, once recrystalisation has started[149], the rate markedly increases[215] with decreasing prior γ-grain size probably because of the associated increase in grain boundary area.

Increasing the reheating temperature will retard recrystallisation in plain carbon steels[14,15] by increasing the prior γ-grain size. In micro-alloyed steels however, increasing the reheating temperature may not appreciably increase the prior γ-grain size but it will increase the micro-alloying addition super-saturation in the steel. This will in turn retard recrystallisation, either through the solute drag[24,25,26,216] and/or the strain-induced precipitation[15,21,217] effects on grain boundary mobility and dislocation rearrangement.

2.2.3.3.2 Effects of Deformation Temperature, Holding Temperature and Isothermal Holding Time

A higher deformation temperature accelerates static recrystallisation

probably because of the accelerated diffusional drift of dislocations although, for a given strain, the temperature effect has been reported[149] to be less than what would be expected solely on the basis of accelerated diffusion.

Holding the deformed material at the deformation temperature increases the recrystallisation rate. However, Leguet et al[218] reported that, relative to the recrystallisation rate of the material deformed and held at the deformation temperature, the material which is deformed at a higher temperature than the holding temperature shows a decrease in recrystallisation rate while the material deformed at a lower temperature than the holding temperature shows an increase in recrystallisation rate. The higher dislocation density and hence higher driving force associated with the lower temperature deformation is the probable reason for the higher recrystallisation rate in the latter case.

In general, the amount of material recrystallised at a given holding temperature increases with time, though the recrystallisation rate tends to fall off towards the end of the recrystallisation process. In a multi-deformation sequence however, it has been reported[215,219] that inter-deformation holding time generally leads to a decrease in the growth rate of recrystallising grains, presumably due to a lowering of the driving force by concurrent recovery. For dynamically recovered structures, Glover and Sellars[219] reported that the growth rate of recrystallising grains is independent of inter-deformation holding time.

2.2.3.3.3 Effects of Strain, Strain Rate, and Deformation Texture

Increasing strain increases the rate of recrystallisation due to an increase in dislocation density[149] which decreases the incubation time by decreasing the critical nucleus size. Also, the higher dislocation density results in an increase in driving force for the acceleration of recrystallisation rate after nucleation. The increase in recrystallisation rate with increasing strain has been well documented for the strain-hardening range of the stress-strain curve[215,219,220]. In the steady state regime of the stress-strain curve, the recrystallisation rate is independent of strain[219] because the stored energy in this region is constant. However, Cotner and Tegart[128] reported a continued increase in recrystallisation rate with strain in the steady state regime. But this effect may well be associated with the influence of heat generated by mechanical deformation as a result of the additional strain after the

steady state has been attained.

Recrystallisation rate increases with increasing strain rate[215,219,221]. However, Wusatowski[215] pointed out that this increase in recrystallisation rate is not a direct proportionality but rather strain dependent. Morrison[222] reported that in low carbon steels, deformed in the austenite range, no change in recrystallisation rate occurs with increase in strain rate in the strain range of 0.05 to 0.25.

In considering the effect of deformation texture, it has been reported[223] that certain austenitic stainless steels develop different rolling textures during hot rolling. Also, transformation textures observed in controlled rolled high tensile steels[224-226] have been related to rolling textures. The dependence of recrystallisation kinetics on strain may be modified by the influence of strain on texture. This phenomenon has not been studied systematically.

2.2.3.3.4 Effects of Solute Atoms and Second-phase Particles

Direct studies of the effect of solute atoms on static recrystallisation after hot deformation seem to be generally lacking. The sparse information[24-26] available indicates that, similar to the effect on primary recrystallisation when cold worked material is annealed, solute atoms retard static recrystallisation after hot deformation. This effect may be broadly attributed to the solute atom drag effect inhibiting the migration of high-angle boundaries and/or the solute atoms restraining the diffusional drift of point defects.

As explained in Section 2.1.2, finely-dispersed second phase particles retard recrystallisation by exerting a Zener drag on grain boundaries and/or by pinning individual dislocations, subgrain walls, and grain boundaries. This phenomenon has been observed in cold[227,228] and hot[21,28-32] worked materials - particularly during hot deformation of steels micro-alloyed with niobium[21,28-32,229-231]. If the second-phase particles are widely spaced, they may, depending on their size, shape, and plasticity relative to the matrix, enhance nucleation for recrystallisation.

Experimental evidence from cold rolling of iron[232], copper[233], and aluminium[234,235] alloys containing hard, widely spaced particles indicates that the minimum size of a particle on which nucleation for recrystallisation can occur is ~1 μm. More recently, Rolf Sandström[236]

suggested a critical particle size of ~2μm, pointing out that to form nuclei around a 4μm particle requires at least 50% cold reduction. The critical particle size generally increases if the strain is reduced, fig. 11[236], and/or if recovery lowers the stored energy in the deformed matrix. Nucleation may occur around particle groups[232,234,237] even if the individual particles are of sub-critical size. A single grain normally nucleates around a particle of 1-5 μm size[235] while multiple nucleation typically occurs around particles larger than ~10 μm[234,237]

The familiar explanation for nucleation around second-phase particles is that the high dislocation densities and large lattice misorientations generated around non-deforming particles in a deforming matrix enhances recrystallisation. For an elongated particle, the misorientations are greatest at the ends[237] of the particle. Humphreys[235] suggested that nucleation occurs, by sub-boundary migration, at a pre-existing subgrain within the highly misorientated region (the deformation zone) around the particle and not necessarily at the particle surface and that the nucleus growth may stop after the deformation zone has been consumed. Rolf Sandström[236] gave a detailed quantitative analysis of the three major stages involved in the process: formation of a nucleus, growth of the nucleus in the deformation zone, and growth of the nucleus outside the deformation zone. He[236] confirmed that initial growth outside the deformation zone critically determines the continued existence of the nucleus.

When nucleation occurs around large particles as discussed above, the overall recrystallisation kinetics may not be adequately described by Avrami's equation. Recently, Rolf Sandström[236], based on his recrystallisation studies of an Al-0.8%Fe alloy containing large particles, derived an expression for the fraction recrystallised, X, by considering only nucleation at particles. The relationship is given as

$$X = 1 - \exp\left[-\frac{4\pi}{3} R^3(d_\varepsilon, t) N_v(d_\varepsilon)\right] \quad \text{---------- (22)}$$

where $R(d_\varepsilon, t)$ is the nucleus size for a particle diameter d_ε exceeding the critical size at time t, and $N_v(d_\varepsilon)$ is the total number of nuclei. The model covers only particles in the diameter range, $2 < d_\varepsilon < 2.5$ μm. Obviously, the model needs, not only experimental validation, but also extension to cover a wider range of particle diameters.

2.2.3.3.5 Effects of Traditional Alloying

While micro-alloying additions are generally known to retard recrystallisation, no specific trend seems to have been established for the more traditional alloys in steel. For instance, Wray[238] observed that a very high level of manganese in low carbon steel retards recrystallisation probably due to the resulting increase in stacking fault energy. On the other hand, Kozasu et al[239] and Roberts[21] reported an acceleration of static recrystallisation by aluminium in plain carbon[239] and niobium[21] steels, suggesting that aluminium as an alloying element in solid solution, accelerates the process of nucleation[239] and the subsequent boundary mobility.

2.2.3.3.6 Effects of Twins and Deformation Bands

Twin boundaries act as preferential nucleation sites for recrystallisation due to the associated high dislocation densities[124]. The subject has been reviewed by Cahn[240]. Ogle and McHargue[241] have presented metallographic evidence for preferential nucleation at deformation twin interfaces in niobium. They[241] noted that the non-coherent twin boundary has a higher migration rate during annealing than the coherent boundary, probably because of the higher interfacial free energy of incoherent, relative to coherent, boundaries. They further showed that twin intersections also act as preferential sites provided that the intersecting twins are large rather than thin.

The only experimental evidence for preferential nucleation at annealing twin boundaries seems to be the observation made by Yakutani et al[242] in α-brass. However, since the structural characteristics of annealing[242] and deformation[124,158-160] twins are similar, and, in particular both have dislocation-rich boundaries, they will be expected to behave identically towards recrystallisation.

Preferential nucleation at twin boundaries and twin intersections suggests that twins generally accelerate recrystallisation through increasing the rate of nucleation although Klein and Rough[243] reported a retardation of recrystallisation by twins.

Deformation bands, also termed transition bands, being regions of high local deformation, also act as preferential nucleation sites for recrystallisation. Therefore, they will be expected to accelerate the kinetics of recrystallisation in a more or less similar manner to twins.

Information on this is generally lacking in hot working of steels.

2.2.3.3.7 Effect of Recovery

When static recovery occurs concurrently with static recrystallisation, the driving force for recrystallisation decreases by an amount equivalent to the driving force for the recovery.

From their studies in aluminium alloys, Vandermeer and Gordon[244] found that the residual stored energy was proportional to the growth rate of recrystallising grains thus indicating that recovery resulted in a decrease in stored energy. The experimentally observed[244-247] decrease in growth rate of recrystallising grains during the annealing of cold worked materials has been attributed[244-249] to recovery taking place concurrently with recrystallisation. Wusatowski[215] also observed a decrease in growth rate after the hot deformation of austenitic stainless steel and he attributed this to competing recovery taking place simultaneously with static recrystallisation.

2.2.3.3.8 Effect of Multiple Deformation Sequences

With the exception of extrusion, and to a reasonable extent planatory mill schedules, where the total strain is achieved in one operation, in commercial hot working schedules, the total reduction is generally achieved in several small contributory strains. The final structure of the worked product is significantly influenced by the microstructural restoration processes occurring between passes.

Results of studies of multiple deformation sequences in thermo-mechanical processing of austenitic stainless[149], aluminium-killed[149] silicon-killed[149] and niobium-microalloyed[14,15,149,250] steels indicate that if partial recrystallisation occurs between deformations, the mixed structures developed are not easily eliminated by subsequent processing. An explanation offered[15] for this effect is that the locally recrystallised regions deform more readily than the neighbouring unrecrystallised matrix resulting in repeated recrystallisation in the same zone with less chances of recrystallisation occurring in the unrecrystallised regions. If, however, the unrecrystallised grains are deformed further to a total strain greater than or equal to the critical strain for dynamic recrystallisation, complete recrystallisation may occur[14-16]. Recently however, Tanaka et al[251] argued that repeated

recrystallisation of the previously recrystallised and subsequently deformed zones does not occur. The subject needs elucidation and so will be examined in the present work.

2.2.3.4 The Statically Recrystallised γ-Grain Size

The recrystallised γ-grain size depends upon the nucleation rate, density of nuclei, critical nucleus size, and the rate of growth of recrystallising nuclei. These parameters, as discussed in section 2.2.3.3, depend in turn on both the material and thermo-mechanical working variables. Material variables such as prior γ-grain size, solute atoms and finely-dispersed second-phase particles will be expected to refine the recrystallised γ-grain size through their effects on increasing nucleation density and/or retarding the growth of the recrystallising γ-grain. However, Roberts and Ahlblom[149] discounted any effects of prior γ-grain size.

The major thermo-mechanical processing variables which influence the recrystallised γ-grain size, in the work-hardening range of the flow stress curve, are temperature, strain and strain rate. An increase in the deformation temperature increases the recrystallised γ-grain size due to increased boundary migration rate. This effect is well documented[14,15,149,250]. There is lack of published direct information on the effect of strain rate on the recrystallised grain size. Roberts and Ahlblom[149] suggested that the strain rate effect may be insignificant but they provided no conclusive evidence in support of this view. At low strains, the density of nucleation is low and this leads to a large recrystallised grain size[149]. In particular, if the reduction is less than ~8%, grain coarsening rather than grain refinement will occur[14]. As the strain is increased, the nucleation rate increases and the critical nucleus size decreases: both of these tend to decrease the recrystallised γ-grain size.

When steady state deformation is reached, the stress and hence the driving force, remain constant as strain is further increased. Consequently, the recrystallised grain size will be expected to become independent of strain in this regime. Tanaka et al[14] suggested that the steady state is reached after ~60% reduction in plain carbon and niobium steels. Rossard and Blain reported an increase in recrystallised γ-grain size with increase in strain in the steady state regime during the deformation of Fe-25% Cr material. It is possible that their observation may in fact

be more accurately related to adiabatic heating resulting from the additional deformation rather than to increase in strain per se.

2.2.3.5 GRAIN GROWTH AFTER RECRYSTALLISATION

2.2.3.5.1 Fundamental Principles and Types of Grain Growth

At the completion of recrystallisation, the material may be considered to be structurally stable in that the internal energy and γ-grain size attain their lowest practical values for that particular set of processing conditions. However, metastability still exists because the internal energy of the material can still be decreased further by reducing the total grain boundary area per unit volume through continued isothermal holding. This continued holding leads to the migration of the grain boundaries through the recrystallised structure, thus resulting in larger grains and smaller total grain boundary area per unit volume. This phenomenon is termed grain growth and is categorised into two types, namely, primary and exaggerated grain growth.

2.2.3.5.2 Primary Grain Growth

Primary grain growth, also referred to as "normal" or "continuous" grain growth involves a gradual increase in the average grain size with the equiaxed grain structure and the general distribution of grain size and shape remaining approximately invariant. As a consequence of complex interactions between the requirements for surface-energy minimisation, space-filling and balance of surface-tension forces at grain boundary junctions, grain boundaries are habitually curved[252,253]. Vogel[254] showed that grain boundaries migrate in such a way that they tend to decrease their curvature during growth. During the growth stage of primary recrystallisation (section 2.2.3.2.8), a grain boundary migrates away from its centre of curvature while during normal grain growth, Sutoki[255] observed that the grain boundary migration is towards the centre of its curvature. The driving force for primary grain growth is essentially supplied by the reduction of the total grain-boundary area in the recrystallised structure.

Burke and Turnbull[156] pointed out that normal grain growth occurs by cannibalisation and not by coalescence and that a grain consuming a neighbouring grain on one side may itself be subjected to consumption by other grains on its other sides. It has been indicated[253,256] that the Kelvin tetrakaidecahedron[257] which has eight hexagonal faces and six square ones, is the most appropriate model that characterises the

three-dimensional shape of a grain. Given this configuration of a minimum surface area and hence minimum interfacial energy, equilibrium between grain boundary tensions is obtained when the grain boundaries meet at 120°. If grain boundaries meet at angles other than 120° due, presumably, to variations in the value of the grain boundary tension, or interfacial energy, or the associated capillary forces, the grain which is included by the more acute angle is consumed. The rate of consumption suddenly increases rapidly just before the grain disappears[156], the disappearance of the grain tending to bring all the angles to 120°.

Kinetic theories of grain growth are normally based on defining the mobility, M, of the boundary in terms of the boundary velocity, V, and driving force, P, by the relationship:

$$V = MP \quad \text{---------- (23)}$$

Experimentally-based derivations of kinetic relationships to describe primary grain growth were pioneered by Beck et al[258,259] and Beck[260]. These workers[258-260] showed that the average grain diameter, D_g, during normal grain growth under isothermal annealing conditions, can be related to the annealing time, t, by

$$D_g = Kt^n \quad \text{---------- (24)}$$

where K and n are constants which are determined by the material composition and annealing time. If the initial (pre-growth) average diameter, D_o, of the grain is not negligibly small compared with D_g, they suggested the more generalised relationship:

$$D_g^{1/n} - D_o^{1/n} = ct \quad \text{---------- (25)}$$

where c is a constant.

Burke[261] used rigorous theoretical interpretations to formalise the concept of boundary curvature as the controlling factor in the kinetic process and then proposed the kinetic relationship:

$$\frac{dD_g}{dt} = \frac{k}{D_g} \quad \text{---------- (26)}$$

the term, k, being defined by $k = C_1 \exp[\frac{-Q_g}{RT}]$

where C_1 is a constant which incorporates the grain-boundary specific interfacial energy, Q_g is the activation energy for growth, R is the universal gas constant and T the temperature in Kelvin. Integration

of equation (26) gives:

$$D_g^2 - D_o^2 = 2C_1 t \exp[\frac{-Q_g}{RT}] \quad \text{---------- (27)}$$

Clearly, equation (27) is similar to that derived by Beck et al[258] as can be seen by putting the value of n = 0.5 (as evaluated experimentally by various workers[259,261,262]) into equation (25).

Experimental observation shows that the rate of normal grain growth decreases with increasing annealing time and stops effectively under the particular processing conditions when the residual grain-boundary area is no longer sufficient to provide an adequate driving force for the process to continue. An earlier stoppage may however be induced by factors such as solute atoms[261,263,264], second-phase particles[261,265,266], sharp preferred orientation textures[267,268] and a free surface[258,269,270].

2.2.3.5.3 Exaggerated Grain Growth

Exaggerated grain growth, also termed "abnormal grain growth", "grain-coarsening","discontinuous grain growth" and "secondary recrystallisation", is a non-uniformly distributed growth process and involves the rapid growth of a few grains while the rest are virtually unaltered until they are consumed. It usually starts only after some normal grain growth has taken place though Simpson et al[271] have reported its occurrence prior to any normal grain growth. For a given material composition, some well defined temperature, "the grain coarsening temperature", must be exceeded for exaggerated grain growth to commence. A definite incubation period is also required for the process to start. Rosi et al[272] reported that a grain has to be at least twice as large as its neighbours before it can grow abnormally. This then accounts for the incubation period. The driving force for abnormal grain growth is similar to that for normal grain growth. When the process is completed, any textures developed differ from the texture pre-existing prior to the start of the process.

Following the results of earlier investigations by Feitknecht[273] and Karnop and Sachs[274], Burke and Turnbull[156] established in great generality the similarities between exaggerated grain growth and primary recrystallisation. In particular, as in nucleus growth during primary recrystallisation, the exaggerated grain growth rate, G_A, is related to temperature, T, by an Arrhenius type of exponential relationship:

$$G_A = G'_o \exp[\frac{-Q_{Ag}}{RT}] \quad \text{---------- (28)}$$

where G_o' is a growth constant and Q_{Ag} the activation energy for abnormal grain growth. In fact, Burke and Turnbull's work[156] accounts for the widespread acceptance of the term, "Secondary Recrystallisation" to describe exaggerated grain growth.

Detailed treatment of exaggerated grain growth mechanisms are well documented[156,175,262]. The inhibition of grain growth by second-phase particles through the pinning of grain boundaries was first systematically analysed by Zener[275]. This inhibition breaks down once particle coarsening occurs. Hillert[276] and Gladman[32] presented detailed treatments of the situation. In his analysis, Hillert[276] assumed a spherical grain shape while Gladman[32] assumed the tetrakaidecahedral grain shape. Gladman[32] considered pinning particles of radius, r, and volume fraction, f, uniformly distributed within a matrix of tetrakaidecahedral grains of radius R_o, into which a large tetrakaidecahedral grain of radius R, is growing. Under these conditions, grain growth is inhibited only if the particle size remains less than a critical radius, r_c, defined by

$$r_c = \frac{6R_o f}{\pi} \left(\frac{3}{2} - \frac{2}{Z}\right)^{-1} \quad \text{---------- (29)}$$

where $Z = R/R_o$. This relationship clearly shows that particle coarsening and grain size heterogeneity are important factors influencing the incubation time for exaggerated grain growth. In a more recent publication, Gladman[277] extended his theory and Hazzledine et al[278] considered the situation where some of the particles are inhibiting grain boundary motion while others are aiding it.

2.2.3.6 STRUCTURAL INHOMOGENEITY OF HOT ROLLED STEEL

There is lack of published investigations into structural heterogeneities in hot rolled steel which should be expected from, among other factors, the heterogeneities of: temperature distribution (section 2.1.3.1), and deformation (section 2.1.4.2). A few studies made in cold rolling using austenitic stainless steels[279], copper, brass and aluminium[280], clearly indicate that the structures developed after rolling are inhomogeneous.

Although there are no reported systematic direct studies of structural inhomogeneities in hot rolled steel, the observation by Forbes and Jones[281] on hot rolled steels which was reported by Jones and Walker[282], as well as the observations of Collins and Honeycombe[283] on hot rolled and drawn

brass, concerning the variabilities of deformation and recrystallisation in hot rolling, clearly indicate that the structures developed after hot rolling are inherently inhomogeneous. Certainly, this subject requires a systematic investigation and clear elucidation. This is taken up in the present research.

2.3 MATERIAL FLOW STRESS DURING THERMO-MECHANICAL WORKING

2.3.1 Variation of flow stress with Hot Working Variables

In general, the flow curve, whether obtained from torsion[132,229,238,284-286] or from tension[287] or from compression[150,230,231,288-291] testing, possesses an initial work-hardening portion, a peak stress value, and a steady state stress regime at large strains. In the steady state regime, it is presumed that the two mutually opposing phenomena, namely, work-hardening and dynamic softening mechanisms, balance each other.

If only dynamic recovery operates as in α-iron and aluminium, the work hardening rate gradually decreases and is finally balanced by the rate of softening, leading to a steady state stress without a pronounced peak, fig. 12[111]. If dynamic recrystallisation operates, as in lead, copper, nickel and austenitic stainless steels, the flow curve has a pronounced peak, fig. 13a[111]. At a high strain rate, the steady state flow stress drops below the peak stress (σ_p) (fig. 13b) in a smooth manner, while at a low strain rate, the steady state flow stress, though still nominally below σ_p, takes up an oscillatory shape of constant frequency and diminishing amplitude resulting from alternate cycles of dynamic recrystallisation and strain hardening (Section 2.2.1.3).

Extensive research by Rossard[292,293] indicates that the critical strain (ε_c) which marks the onset of dynamic recrystallisation, is related to the strain ε_p to the peak stress σ_p (fig. 13b) by:

$$\varepsilon_c \cong 0.83\ \varepsilon_p \qquad \text{(30)}$$

More recently, Le Bon et al[25] modified this to:

$$\varepsilon_c = 0.67\ \varepsilon_p \qquad \text{(31)}$$

2.3.2 Quantitative Relationships between flow stress and Hot Working Variables

Investigations carried out with tool steels[294], titanium and uranium alloys[295], and commercial high purity aluminium[296] clearly reveal that the flow stress (σ_f) is sensitive to strain rate($\dot{\varepsilon}$), that

is, σ_f increases as $\dot{\varepsilon}$ increases. The effect of a low deformation temperature on σ_f is similar to that of a high $\dot{\varepsilon}$ and this led MacGregor and Fisher[297] to propose the velocity modified temperature, T_m, which presumes to combine the effects of temperature and strain rate and is given by

$$T_m = T(1 - k \ln\frac{\dot{\varepsilon}}{\dot{\varepsilon}_o}) \quad \text{----------} \quad (32)$$

where T is the absolute temperature of the deformation, k is a constant, $\dot{\varepsilon}$ the true strain rate of the test and $\dot{\varepsilon}_o$ a unit strain rate. A better known version of this is the temperature compensated strain rate, Z, which, although it has become popularly known as the Zener Hollomon parameter, was in fact the result of a re-formulation[298] of Zener and Hollomon's[299] concept of a mechanical equation of state which was proved to be non-valid by several workers such as Orowan[300]. By definition,

$$Z = \dot{\varepsilon} \exp(\frac{Q_{def}}{RT}) \quad \text{----------} \quad (33)$$

where R is the Universal gas constant and Q_{def} is the activation energy for the hot deformation, defined by

$$Q_{def} = -R[\frac{\partial \ln \dot{\varepsilon}}{\partial(1/T)}]_{\sigma_k} \quad \text{----------} \quad (34)$$

where σ_k is some chosen constant stress value. The restoration mechanism operating at low values of Q_{def} is believed to be dynamic recovery[102] and since, in this case, diffusion of vacancies may be the rate controlling process, Q_{def} may be quite close to the activation energy for self-diffusion, ΔH. On the other hand, higher values[301,302] of Q_{def} are associated[102,302] with the occurrence of dynamic recrystallisation. The results of Roberts[21] and Ahlblom[303] contradict this trend in that their Q_{def} values for recovery exceed their Q_{def} values for dynamic recrystallisation.

The dependence of the steady state flow stress (σ), on strain rate ($\dot{\varepsilon}$) at low and high strains, was actually first recognised in steady state creep[304]. This led to the creep power law for low stress:

$$\dot{\varepsilon} = A\sigma^n \exp[\frac{-Q_{def}}{RT}] \quad \text{----------} \quad (35)$$

and to the exponential relationship:

$$\dot{\varepsilon} = A_1 \exp(\beta\sigma) \exp[\frac{-Q_{def}}{RT}] \quad \text{----------} \quad (36)$$

which is used to correlate data at high stresses. A, A_1, n and β are temperature independent constants .

The similarity between steady state creep conditions and hot deformation led Sellars and Tegart[102] to propose a hyperbolic sine relationship for hot working, viz:

$$\dot{\varepsilon} = A_2 \ (\sinh\alpha\sigma)^n \exp[\frac{-Q_{def}}{RT}] \quad \text{---------- (37)}$$

where A_2, α, and n are temperature independent constants and α, β and n are related by:

$$\beta = \alpha n \quad \text{---------- (38)}$$

At low stresses ($\alpha\sigma < 0.8$), equation (37) reduces to the power law (equation 35) and at high stresses ($\alpha\sigma > 1.2$), it reduces to the exponential relation (equation 36). It is interesting to note that equation (36) can be re-arranged to give the Zener-Hollomon[299] temperature compensated strain rate

$$Z = \dot{\varepsilon} \exp\ (\frac{Q_{def}}{RT}) = A_1 \exp(\beta\sigma) \quad \text{---------- (39)}$$

and equation (37) can also be similarly re-arranged, viz:

$$Z = \dot{\varepsilon} \exp(\frac{Q_{def}}{RT}) = A_2 (\sinh\alpha\sigma)^n \quad \text{---------- (40)}$$

2.3.3 Evaluation of Flow Stress under Hot Working Conditions

2.3.3.1 Tensile, Torsion, Axisymmetric Compression and Plane Strain Deformation Routes

The more traditional testing techniques for evaluating flow stress are tensile[287,305,306], torsion[132,229,238,284-286,305], and axisymmetric compression[230,231,288-291]. Each of these techniques has some drawbacks. For instance, tensile testing has the disadvantage that at relatively small strains, localised necking takes place prior to failure by fracture. Torsion testing permits the use of larger strains but suffers from inhomogeneities of strain and stress in the axial and through-thickness directions of the specimen. Axisymmetric compression involves finding a practical means of obtaining homogeneous deformation as well as ensuring that the strain rate remains constant during the testing by incorporating a logarithmic cam as in the cam plastometer[95].

Plane strain compression[305-309] testing is gaining increased recognition as a viable testing technique following Ford's[306] comparative demonstrations that it furnishes results which are as accurate as the other testing methods above, see figs. 14 a & b. However, this is so

only provided that certain basic conditions are met when employing the plane strain deformation technique.

2.3.3.2 Plane Strain Deformation Technique

2.3.3.2.1 The Basic Theory and Practice of Plane Strain Deformation

During compression, the vertical strain (ε_z), normally results in strains ε_x and ε_y in the breadth (x) and length (y) directions. If $\varepsilon_x = 0$, then the deformation is termed plane strain deformation. It can readily be shown that under plane strain deformation, the principal stresses σ_1, σ_2, σ_3 in the x, y, and z directions respectively, are related by:

$$\sigma_2 = \tfrac{1}{2}(\sigma_1 + \sigma_3) \quad \text{---------- (41)}$$

where σ_1 and σ_3 are the greatest and smallest stresses respectively. The Von Mises and Tresca yield criteria give the same results for yielding in plane strain, viz:

$$\sigma_1 - \sigma_3 = 2k \quad \text{---------- (42)}$$

where k is the yield stress in pure shear. From equations (41) and (42) it can be shown that

$$\sigma_1 = \sigma_2 + k \quad \text{---------- (43)}$$

and, $\sigma_3 = \sigma_2 - k$

which suggests that plane strain deformation occurs under the influence of a pure shear, k, plus a superimposed hydrostatic stress σ_2. However, equation (42) shows that yielding is entirely due to the pure shear component, k, without any contribution from the hydrostatic stress σ_2. The triaxial state of strain in compression as opposed to the uniaxial strain in simple tension necessitates the use of an equivalent or effective strain (and equivalent stress too). The stress S, measured in plane strain (termed constrained yield stress) is normally related to the equivalent uniaxial stress Y (to be denoted here by $\bar{\sigma}$), as measured in tension, using the Von Mises yield criterion by the expression:

$$S = \sigma_1 - \sigma_3 = 2k = \frac{2}{\sqrt{3}}\bar{\sigma} \quad \text{---------- (44)}$$

Thus the true stress, S, obtained in plane strain must be multiplied by $\frac{\sqrt{3}}{2}$ to obtain the equivalent true stress $\bar{\sigma}$, i.e.

$$\bar{\sigma} = \frac{\sqrt{3}}{2} S \quad \text{---------- (45)}$$

Similarly, the equivalent true strain, $\bar{\varepsilon}$, in plane strain is given by:

$$\bar{\varepsilon} = \frac{2}{\sqrt{3}} \varepsilon \quad \text{---------- (46)}$$

where ε is the true strain measured in the plane strain deformation.

The practical implementation of plane strain deformation involves eliminating ε_x. This can be done by using external lubricated walls to restrict lateral spread or by deforming only the central portion of a wide, rigid block so that the rigid material outside the plastic zone provides the constraint to sideways spread. The second principle is utilised in the Ford test[309] whose principles are shown schematically in Figs. 15 a & b. In this test[309], a metal strip of width b and thickness h is compressed between a pair of overlapping tools of width w. The Ford design requires that:- the tools should be accurately ground square and parallel and mounted rigidly; the specimen breadth (b) should be 5 to 10 times the tool width (w) so as to minimise spread; and the w/h ratio should not be less than 2 in order to avoid excessive tool pressures and not greater than 4 so as to minimise frictional effects. The methodology of the test for flow stress evaluation[309] involves re-lubricating the sample after every 2-5% reduction and finally extra-polating[307] to zero strain to obtain the material yield stress. Obviously the technique as outlined cannot be applied to hot working because the extremely light strains and the numerous interruptions for relubrication will result in a complex and adverse structural development in the material being deformed. The Ford design also has no device for ensuring a constant strain rate. In addition, friction cannot be ignored at high strains of industrial significance because at such strains, the w/h ratio cannot be constrained not to exceed 4.

2.3.3.2.2 Effect of Friction

The yield criteria given by equations (42) and (44) do not apply under frictional conditions because interface friction, μ, raises the load required for yielding which in turn results in an apparent flow stress which is higher than the true flow stress. Hill's[310] expression for the distribution of the vertical stress (σ_1) when friction is operative is given by:

$$\sigma_1 = 2k \exp(2\mu \frac{x}{h}) \quad \text{---------- (47)}$$

This expression, shown schematically in figure 16a as the familiar

Friction Hill, has been reported[311,312] to give good results under slipping (coulomb) friction conditions (Fig. 16a) where μ is small. At full sticking friction, the specimen moves relative to the tools by shearing of the material and no more by sliding. This implies that

$$\mu\sigma_1 = k \quad \text{---------- (48)}$$

For the case of sticking friction, it can be shown that the distribution of the vertical stress (σ_1) obeys the relationship:

$$\sigma_1 = 2k(1 + x/h) \quad \text{---------- (49)}$$

In practice however, the pressure distribution is such that while some regions of the specimen surface (such as near the edge, x = 0) may be under full slipping frictional conditions and some regions (usually at positions x = w/2) are subjected to full sticking friction, the rest of the specimen surface experiences frictional conditions which are intermediate between the full slipping and full sticking regimes. This implies that there exists a point where transition from full slipping to full sticking occurs. If this point is located at a distance x_o measured from the edge of the specimen (fig. 16b), then x_o can be evaluated by eliminating σ_1 between equations (47) and (48). This operation gives

$$x_o = \frac{h}{2\mu} \ln(\tfrac{1}{2}\mu) \quad \text{---------- (50)}$$

This expression reveals that x_o is a function of both friction and specimen thickness. By relating h to μ, then w/h can also be related to μ. Equations (47) and (49) may then be modified to incorporate x_o so that the slip-stick frictional conditions at regions $x > x_o$ are also taken into account in evaluating the material flow stress. This approach has been adopted in the plane strain deformation work carried out in the present research work. The situation is represented diagrammatically in Fig. 16b.

2.3.3.2.3 Effect of Lateral Spread

For a wide specimen, spread may be presumed to be negligible for practical purposes but if the specimen breadth is less than ~6 to 8 times its thickness, spread is no longer negligible. The spread relaxes the friction at the specimen ends resulting in the end lines of the Friction Hill becoming curved, cutting off the triangular corners. Orowan and Pascoe[47] suggested incorporating a spread coefficient as a correction factor. Although the spread coefficient, s, is formally defined[313] by:

$$s = \frac{\text{True Strain in Breadth Direction}}{\text{True Strain in Thickness Direction}} = \frac{\ln(b/bo)}{\ln(h_o/h)} \quad \text{--------} \quad (51)$$

the geometry of the deformed specimen makes measurements required for evaluating s from this expression extremely difficult. Consequently, values of s used in particular working processes are obtained from empirical relationships[314,315].

It must be noted that if the specimen breadth is less than ~1.5 to 2 times its thickness, no valid expression can be derived because[47] the fundamental plane strain conditions cannot be satisfied.

2.3.3.2.4 Effect of Tool Width to Specimen Thickness (w/h) Ratio

It has been shown theoretically[310,316] and experimentally[307] that the pressure exerted by the tools during plane strain deformation varies with the ratio of the tool width (w) to the specimen thickness (h). This phenomenon is presumably associated with the dependence of the redundant work done during the deformation on the w/h ratio.

Quantitative evaluation[317] of the redundant work is normally done by applying slip line field theory[317] to plane strain deformation of a material assumed to be isotropic and rigid-plastic. Theoretical slip line solutions by Green[316], experimentally validated by Watts and Ford[307] for values of w/h > 1, indicate that the pressure exerted by the tools passes through maximum values between integral values of w/h.

2.4 CORRELATIONS OF MECHANICAL PROPERTIES WITH STRUCTURE; AND OF STRUCTURE WITH THERMO-MECHANICAL PROCESSING VARIABLES IN STEEL

2.4.1 Prediction of Mechanical Properties as a Function of Composition and Microstructure

Following the Hall-Petch relationship[318,319] between yield stress and grain size, numerous investigations[320-325] have been carried out to correlate, quantitatively, various mechanical properties such as yield strength[320-325], 0.2% proof stress[320,324,325], formability[321] and toughness[322] of steels, to compositional and structural factors. These correlations have been carried out for a wide range of steels, notably, plain carbon and HSLA steels[323], low carbon bainitic steels[324], austenitic stainless steels[321,325], ferrite-pearlite structures[321], and silicon killed carbon manganese steels[322]. The various relationships derived clearly show that mechanical properties of steels are

determined by composition and structure.

Compositional factors however, have practical limits above which any further increase in their amounts will impair some properties while improving others. For example, in addition to the harmful effects of high carbon content to corrosion resistance in stainless steels, the relationships[320-325] indicate that increasing carbon content increases the yield strength, 0.2% proof stress and work-hardening rate, but decreases both the maximum uniform strain and the total strain at fracture (total ductility). The relationships developed for HSLA steels[323] also show that an increase in Mn content increases the yield strength. But, as explained earlier (section 2.1.2), if Mn is increased beyond a certain level, it will result in the formation of bainite, although a higher Mn can be accommodated at low carbon contents.

The structural factor of greatest importance is grain size. Though dislocations and low angle boundaries contribute to strength, they impair toughness because they do not resist crack propagation. Grain size refinement remarkably improves yield strength, formability, total ductility, and toughness without leaving any residual harmful effects. In fact only the maximum uniform strain is indifferent to grain size.

2.4.2 Prediction of Recrystallised γ-Grain Size as a Function of Thermo-Mechanical Processing Variables

The ultimate grain size of the finished product is determined by the recrystallised γ-grain size after working. Even if the steel is transformable, the transformed α-grain size will be expected to reflect the size of the parent γ-grain size. Since the recrystallised γ-grain size depends on the material and thermo-mechanical processing variables (section 2.2.3.4), it will be of considerable Metallurgical and Engineering significance if quantitative relationships can be established for predicting the recrystallised γ-grain size as a function of these variables. Disappointingly, such studies are generally lacking. The only published studies of this kind seem to be those by Sellars and Whiteman[326,327], Barraclough and Sellars[328], Towle and Gladman[185], and Sellars[329].

Sellars and Whiteman[326,327], after analysing various published data on hot rolling of austenitic and a range of other steels, proposed that the recrystallised γ-grain size, d_{rex} could be related to hot working

variables by the relationship[326,327]:

$$d_{rex} = 25\ \varepsilon^{-1}(d_o^{\frac{1}{2}})(\frac{1}{\beta}\ \ln\frac{Z}{A})^{-0.67} \quad (\text{for } \varepsilon < \varepsilon_c)^{(327)} \text{ ------- (52)}$$

where ε is the true strain, d_o the initial γ-grain size prior to deformation, Z is the Zener-Hollomon temperature compensated strain rate, and β and A are constants which, for a strain of ~0.2, were assumed[326,327] to be 6.7×10^{-2} mm²/N and 8.5×10^{-19} s^{-1} respectively for mild steel, and for niobium steels at temperatures greater than 1000°C. They[326,327] also assumed that all normal conditions of plate rolling are covered by values of $Z > 3 \times 10^{11} s^{-1}$.

Barraclough and Sellars'[328] relationship, based on torsion tests with type 304 stainless steel, carried out in the temperature range of 950-1150°C, stipulates that d_{rex} is given by:

$$d_{rex} = \frac{B(d_o^{\frac{1}{2}})(Z)^{-0.1}}{1.15 - \exp[-2.5\ (\frac{\varepsilon^{-0.08}}{\varepsilon_p})^2]} \text{ ---------- (53)}$$

where B is a constant equal to 125 with units $s^{0.1}\ \mu m^{0.5}$; ε is the applied strain while ε_p is the strain to the peak stress. From the results of their plane strain rolling of types 304 and 316 austenitic stainless steels at 900, 1000 and 1100°C, Towle and Gladman[185] proposed that, for austenitic steels and possibly all other austenitic materials, d_{rex} may be expressed by

$$d_{rex} \propto \varepsilon^{-\frac{1}{2}}(d_o^{1})\ Z^{-0.06} \text{ ---------- (54)}$$

where the constant of proportionality = $2.24\ s^{-0.06}$ and the effect of temperature, assumed[185] to be small, is absorbed in Z.

Sellars[329] analysed hot working data available in the literature for a range of C-Mn and niobium-microalloyed HSLA steels and then proposed that the relationships obeyed by d_{rex} are of the following forms:
for C-Mn steels,

$$d_{rex} = D\varepsilon^{-1}d_o^{0.67} \quad (\text{for } \varepsilon < \varepsilon_c) \text{ ---------- (55)}$$

and for niobium-microalloyed steels

$$d_{rex} = D'\varepsilon^{-0.67}\ (d_o^{0.67}) \quad (\text{for } \varepsilon < \varepsilon_c,\ T > 950°C) \text{ ------- (56)}$$

where D and D' are constants. Sellars[329] reported that D varies from 0.35 to 0.83 with a best average of $0.5\ \mu m^{0.33}$ while D' varies from 1 to 1.86 with a best average value of $0.9\ \mu m^{0.33}$. In the steady state,

he[329] had no data for analysing Nb-microalloyed steels but for C-Mn and low alloy steels, he suggested that d_{rex} is independent of d_o and may be given by:

$$d_{rex} = D^* Z^{-u} \quad (\text{for } \varepsilon > \varepsilon_c) \qquad \text{(57)}$$

where u takes values of 0.16 and 0.13 for C-Mn and low alloy steels respectively and D* is related to D in equation (55) by:

$$D^* = 3.6 \times 10^3 D \qquad \text{(58)}$$

Sellars[329] assumed a mean value of u = 0.15 and then suggested relationships for evaluating ε_p and ε_c (fig. 13b) respectively as:

$$\varepsilon_p = 4.9 \times 10^{-4} (d_o^{\frac{1}{2}}) Z^{0.15} \qquad \text{(59)}$$

and,
$$\varepsilon_c = 0.57 (d_o^{0.17}) \varepsilon_p \qquad \text{(60)}$$

Recently, T. Siwecki, Alf Sandberg and William Roberts[330], in an unpublished work, suggested the empirical relationship:

$$d_{rex} = 3.32 + 53.51 d_o^{0.5} \varepsilon^{-0.65} \{\exp[\frac{42100}{T}]\}^{-0.1} \qquad \text{(61)}$$

for the prediction of the recrystallised γ-grain size (d_{rex}) in a hot worked Ti-V steel.

From the foregoing expressions, it seems obvious that there is no unanimity by the various workers[185,326-330] on a unique relationship between the recrystallised γ-grain size and thermo-mechanical processing variables. The subject requires elucidation and this will be attempted in the present research work.

CHAPTER 3: EXPERIMENTAL WORK

3.1 Objective and Design of the Research Programme

The objective of the present research was to investigate the influence of thermo-mechanical processing variables on the structure of rolled steel and to assess the extent to which the heterogeneities of these variables lead to structural inhomogeneities in the as-rolled steel product. The investigation was mainly based on recrystallisation and grain size measurements on hot rolled and upset-forged samples. The rolling and upsetting work were supplemented with plane strain deformation on a computer-controlled servo-hydraulic machine in order to obtain additional data, such as the activation energy for hot deformation, which are necessary for building a model for the prediction of recrystallised γ-grain size as a function of processing variables. Limited work on isothermal transformation of austenite to ferrite was carried out primarily to ascertain the effects of inhomogeneities of deformation and of recrystallisation of austenite, as well as of the austenite morphology just prior to the $\gamma \rightarrow \alpha$ transformation reaction, upon the size and homogeneity of the ensuing α-grains. The rolling, upsetting, plane-strain servo-testing, and $\gamma \rightarrow \alpha$ isothermal transformation programmes are presented schematically in figure 17.

The major work outlined above was supported by a number of ancillary investigations designed:- to establish a lubrication technique which ensures uniform deformation during upset-forging; and, to identify more accurately the distributions of temperature and strain in the through-thickness direction of the material during thermo-mechanical working, particularly in hot rolling.

For the quantitative analysis of the experimental results, statistical methods were extensively employed. The most important of these methods are outlined in Appendices 6a-e and 7.

3.2 Experimental Material

3.2.1 Materials used and their Chemical Compositions

Two classes of steel were used for the major investigation:

(i) An austenitic stainless base steel and similar austenitic stainless steel with varying amounts of niobium additions.

(ii) A C-Mn base HSLA steel with varying amounts of niobium additions. The relative merits of Nb as a micro-alloy have been discussed in

the case study in Appendix 1 and its choice here was particularly based on its strong inhibition of recrystallisation.

The ancillary investigations concerned with temperature distribution were carried out using the same materials ((i) and (ii) above) which were used for the major investigation. On the other hand, strain distribution studies were conducted with mild steel containing Type I MnS inclusions, intentionally produced to act as internal inserts; and with a lead-selenium alloy.

The various materials used and their chemical compositions are shown in Tables 1(a-d).

3.2.2 Melting Practice for the Steels

A high purity bar iron of composition shown in Table 2 was used for producing air melts of the various steels in a 15 kg capacity induction melting unit. The standardised sequence of steel making practice adopted for the production of each class of steel is summarised below:

(i) Austenitic stainless steels

Melt down high purity bar iron plus Nickel and slag off.
Add 100 gm ferro-silicon.
Add ferro-chromium.
Add rest of ferro-silicon; and add all ferro-manganese.
Deoxidise with aluminium and repeat slagging off.
Adjust temperature to 1560°C.
Add micro-alloying element as ferro-niobium.
Cast UVAQ sample for analysis.
Teem remainder of metal into a cast iron mould to produce a 15 kg ingot of 75 mm x 75 mm square section.

(ii) Carbon-Manganese-Niobium Steels

Melt down high purity bar iron and slag off.
Add 80 gm ferro-silicon.
Add rest of ferro-silicon; and all ferro-manganese.
Deoxidise with aluminium and slag off again.
Adjust temperature to 1590°C.
Add ferro-niobium, and as soon as dissolution of FeNb is assured, cast the UVAQ sample for analysis.
Teem into cast-iron mould to produce a 15 kg ingot of 75 mm x 75 mm cross-section.

In both (i) and (ii) an exothermic powder, EP 6810, was used to minimise ingot piping. In addition, a tapered mould was used to teem later ingots and this drastically reduced piping and increased the yield.

In order to obtain good yield from the FeNb addition, it was necessary to wrap the FeNb in pure iron foil on the end of a 6.35 mm diameter mild steel rod. This was then plunged to the bottom of the melt and vigorously stirred. Casting of UVAQ sample and teeming then followed immediately.

(iii) Mild Steel rich in rounded Manganese Sulphide Inclusions

Melt down high purity bar iron.
Add ferrous sulphide (to give 0.3%S).
Add just sufficient FeSi to "kill" the metal, after adding FeMn.
Cast into dried sand moulds of various sizes (cross-sections of 44 mm x 44 mm, 25 mm x 25 mm, and 25 mm x 15 mm), prepared from Mansfield Red Sand.

3.2.3 Preparation of Samples for Experimental Deformation

After cropping off the top ends of the ingots to clear piping, they were machined on all faces to remove surface defects. Each ingot for the experimental rolling and forging programmes was divided into two. One half was rolled to 22 mm square section and the other half was rolled to 22 mm gothic (round) bar. Steel ingots for plane strain deformation were rolled to flat bars of 65 mm x 13 mm. After these preliminary rolling operations, all the austenitic stainless steels were homogenised at 1000°C for one hour while all the C-Mn and HSLA steels were homogenised at 950°C for one hour, followed by air cooling in each case.

The sectional bars for rolling were ground to a constant width of 20 mm but various thicknesses: 20 mm, 16 mm, 13 mm, and 10 mm which, after different percentage reductions in thickness (60%, 50%, 38.46%, 20% respectively), resulted in specimens of the same thickness, viz, 8 mm. The 22 mm diameter round bars for upset-forging were turned to 20 mm diameter round bars and cut into short cylinders of different heights: 20 mm, 16 mm, 13 mm, and 10 mm, with or without grooves scribed on the flat circular faces. As in the rolling programme, after different reductions by upsetting, the specimens were reduced to the same thickness of 8 mm. The constancy of the final thickness was necessary in order to achieve a constant cooling rate from sample to sample in both the rolling and the upset-forging programmes.

The flat bars for plane strain testing were ground to 50 mm wide by 10 mm thick flat pieces with two holes, 40 mm apart, drilled at the central region of each test piece (see Fig. 18). The C-Mn and HSLA steels for this test were chromium-plated to minimise oxidation. After getting rid of ingot piping from the sand cast mild steel rich in MnS inclusions, they were ground to sectional bars of 40 mm x 40 mm, 20 mm x 20 mm, 20 mm x 16 mm, 20 mm x 13 mm and 20 mm x 10 mm. Sectional bars of similar dimensions were also machined from the lead-selenium alloy ingot, purchased in the as-cast ingot form.

3.3 DETAILED EXPERIMENTAL TECHNIQUES

3.3.1 Assessment of Effect of Solution Treatment on Starting Structure

In order to assess the effect of high temperature solution treatment on the size and morphology of the starting grains, some C-Mn-Nb steel which was solution treated at 1300°C and part of it not solution treated were both homogenised at 950°C for 1 hour and then air-cooled. Longitudinal sections were examined under an optical microscope and the grain sizes determined.

3.3.2 Determination of Optimum Reheating and Soaking Periods

The time the centre of the sample takes to attain the reheating furnace temperature of 1100°C and the time it takes to cool from this temperature to 1000°C when the sample was subsequently transferred into a second furnace maintained at 1000°C, were determined experimentally by means of a Pt-Pt/Rh thermocouple inserted into a 1.6 mm hole such that its hot junction was at the mid-point of the representative sample whose temperature was being monitored. The reheating temperature (1100°C) was attained in ~6 minutes and when subsequently transferred into the second furnace at 1000°C, 5 minutes elapsed before the specimen cooled to this latter temperature. From these results, it was decided to reheat at 1100°C for 45 minutes to ensure adequate dissolution of carbides and carbo-nitrides and roll or forge at the same temperature, or to reheat at 1100°C for 45 minutes, cool and soak at 1000°C for a further 15 minutes, and then deform by rolling or by forging. The reheating schedule for the plane strain tests was similar to the above but soaking times at deformation temperatures (1100°C, 1000°C and 900°C) were very closely followed by the electronic computer unit (section 3.8.1). On the other hand, the mild steel samples containing Type I MnS inclusions were simply reheated for 1 hour at 1000°C and then deformed, 1000°C being ideal for obtaining $\nu \cong 1$.

3.3.3 Calibration of forging press for Strain Rates

The forging press was calibrated to ensure that the strain rates employed in the rolling process would also be obtained in the forging work. The calibration was based on the relationship:

$$\dot{\varepsilon} = (\ln \frac{h_1}{h_2})/t \quad \text{---------- (62)}$$

where h_1 and h_2 are the initial and final heights of the cylindrical sample and t an experimentally determined time taken to reduce the specimen from h_1 to h_2. Details of the calculations, including all necessary assumptions, are shown in Appendix 4, where a general relationship for the evaluation of $\dot{\varepsilon}$ is also developed.

3.3.4 Investigation of Lubrication Technique for the Hot Upset-Forging Deformation

The primary objective for this investigation was to establish the best lubrication technique for obtaining homogeneous deformation. Initial tests were carried out with material whose chemical composition was similar to that of the experimental steels used for the main research programme. The test specimens were prepared in the form of solid cylindrical pieces of diameter 20 ± 0.02 mm and height 20 ± 0.02 mm corresponding to the largest specimen size which was to be used in the main upsetting work. Initially, the end faces of the cylindrical specimens were made flat with a surface finish of $\nabla\nabla\nabla_8$ (standard notation for surface smoothness of the type achieved by thorough grinding). Starting with these as initial conditions, investigations were carried out to establish the correct type and grit size of the lubricant, the best mode of its application, and an effective method of lubricant entrapment under the specimen throughout the deformation process.

3.3.4.1 Establishing Correct type of lubricant

Lubricants employing fluid as carrier, and solid lubricants were investigated in the deformation temperature range of 900 - 1100°C, with the surface temperature of the platens raised to ~550°C (section 3.5.1). The fluid-based lubricants investigated included: a dispersion of colloidal graphite in water, aqueous solutions of colloidal graphite at different levels of dilution, graphite in oil, and a dispersion and a thick slurry of glass powder in water.

Both brushing and spraying of the fluid-based lubricants were tried with unsatisfactory results. Application of the solid lubricants was

initially by sprinkling the powder evenly over the bottom platen and on top of the heated specimen just prior to deformation. Preliminary tests carried out with two grades of glass powders obtained by separately crushing and powdering broken window pane glass and milk bottle glass indicated that glass was potentially the best lubricant for the deformation. Consequently, the rest of the investigation was continued with lime-soda window glass, pyrex glass, and a mixture of both. Each glass powder was powdered down from the as-received -30 mesh size to finer grits and sieved into different grit size groups ranging from 53 μm to 210 μm for studying the effect of grit size on the lubrication efficiency. The degree of barrelling, quantified by the Barrelling factor, B_f, [see Appendix 5] was used to characterise the efficiency of each lubrication technique.

3.3.4.2 Development of the Best Method of Applying the Glass Powder

Observed harmful effects of scaling were checked by reheating specimens in a protective argon atmosphere while the problem of long dwell-times was tackled by reducing the forging stroke from its original value of 150 mm to only 50 mm and also by replacing the "powder spreading method" by a method involving dipping the two flat end faces of the heated specimen into glass powder and then deforming. As the 'dipping techique' did not pick up sufficient glass lubricant, plastic bonding of the powder on to the specimen was devised. In this technique, the specimen was profusely spray-coated with CHESTERON Clear Acrylic Plastic Coating liquid and the glass powder generously applied all over it at ambient temperature. The powder-covered specimen was left for ~60 minutes for proper bonding to occur and then inserted into the furnace for reheating and subsequent deformation without any further application of glass powder.

The failure of the 'plastic-bonding' technique to furnish flawless results was believed to be due to viscous lubricant squeeze-out prior to the end of the deformation action. The specimen end faces were therefore engraved with different types of marks for lubricant entrapment. The marks investigated included random shallow indentations; a set of parallel, evenly spaced, straight lines, a square grid network; a rhomboidal grid network; a trough-like depression similar to that used by Suzuki et al[87]; and spiral grooves. The depth of the grooves in each case was 0.04 mm. The spacing of the indentations was difficult to regularise but the straight or grid lines were spaced at 0.3 mm. The initial pitch of the spiral grooves was 0.3 mm and further investigation revealed that a pitch of 0.625 mm (Fig. 19), gave the best lubrication efficiency.

In order to increase the amount of molten glass applied to the specimen prior to deformation, the spirally grooved samples were heated in a pool of molten glass maintained in a refractory trough inside the reheating furnace. This practice resulted in the initially clear glass in the trough turning pale green. The cause of this colour change was investigated using line spectra and from the results, presented in Section 4.1.2.3, heating inside molten glass was dropped. Instead, the 'plastic bonding' of glass was carried out merely to prevent oxidation which would otherwise damage the spiral grooves and after reheating, the specimen was fully submerged into a pool of molten glass maintained separately inside the reheating furnace, and then deformed immediately.

3.3.4.3 Investigation into the Effects of Processing Variables on Lubrication Efficiency

The optimised lubrication technique described in the last section was used to investigate the influence of variables such as strain, strain rate, multiple deformation, re-lubrication in a multiple deformation sequence, and scale, on lubrication efficiency.

In addition, tests were conducted to separate the effects of temperature inhomogeneity on the differential expansion of the end faces of upset samples from the influence exerted by frictional effects. In order to study the effects of friction, one face of the heated cylindrical specimen was properly lubricated while one face was not lubricated at all and the sample was deformed. For temperature effects, one end of an unlubricated, uniformly heated sample was dipped into ice-cooled water for 2-5 seconds to induce a steep temperature gradient within the specimen and deformation was then carried out by upsetting.

3.4 HOT ROLLING PROGRAMME

3.4.1 The Rolling Mill

The rolling mill used for the hot rolling work is shown in figures 20 a & b. It is a 2-high, horizontal mill, which is fitted with 254 mm diameter, plain-faced, alloy steel rolls driven by an 80 hp dc motor. A motorised screwdown mechanism, driven through bevel gears, enables the top roll to be lifted so that the roll gap can be accurately set using a scale engraved round the screwdown pin. Front and back tables are provided to facilitate material feed into, and withdrawal from, the roll gap during the rolling operation.

3.4.2 Rolling Technique

Figure 17 incorporates the hot rolling programme. Sectional bars prepared into rolling samples (section 3.2.3) were reheated at 1100°C and rolled either at 1100°C or at 1000°C, argon being used to minimise oxidation in the non-stainless steels. The strain rate was calculated using Larke's relationship (eqn. 8, section 2.1.5.1) for sticking friction. The nominal % reduction was varied from 20% to 60% by reducing starting bars of different thicknesses to specimens of the same thickness (8 mm). The constancy of the final thickness was designed to eliminate cooling rate as a variable. The actual strains, ε, imposed were calculated as true strains using the relationship:

$$\varepsilon = \ln (h_1/h_2) \quad \text{---------- (63)}$$

where h_1 and h_2 are the initial and final thicknesses respectively.

In order to establish the initial structure just prior to rolling, one reheated sample was quenched in iced-brine without deformation. The rolling reduction was carried out either in one or in multiple passes. The sum of the strains in each multiple pass sequence was equal to the strain imposed in the 60% reduction single pass schedule. The inter-pass time adopted was 10 seconds which compares well with the 10-15 secs interpass period used in industrial hot rolling of plates. In particular, this allowed time for the roll gap to be adjusted after the previous pass. Using a manual, lever-operated, hot shear, a short piece was cut off from the rolled sample and quenched in iced-brine after a 10 second interval reckoned from the instant the rolled stock just emerged on the exit plane of the rolls. The rest of the bar was immediately returned into the furnace for isothermal holding at the rolling temperature. After holding for a prescribed time, the bar was brought out and another short piece was hot-sheared, quenched in iced-brine, and the remaining bar returned again into the furnace for further holding. This process was continued until the last piece was quenched in iced-brine.

3.5 HOT UPSET-FORGING PROGRAMME

3.5.1 The Hydraulic Press

The hydraulic press, whose essential features including its hydraulic circuit are shown in figures 21 (a-e), is rated to provide 38 tonne compressive force over a full stroke of 150 mm. Principally, it consists of two parallel flat platens (fig. 21b) made of high speed steel and fitted

with electrical heating elements situated some distance away from the working faces and capable of raising these faces to, and maintaining them at, working temperatures of 550°C; a hydraulic accumulator (fig. 21c) partially filled with hydraulic oil, pre-charged by nitrogen and pressurised by an electrically driven pump; a bobbin-limit switch device (fig. 21d) which regulates the upward movement of the top platen; local and remote buttons for activating the press; and controls for speed and temperature variations. During deformation, the downward motion of the top platen is stopped by means of a circular (deformation) ring, fig. 21b, machined from a 5% Chrome hot die steel. The force build-up due to the presence of this ring activates a pressure switch which in turn causes the top platen to return to its starting position. The hydraulic circuit of the press is shown in detail in Fig. 21e.

3.5.2 Upset-Forging Technique

In order to ascertain the effects which inhomogeneity of deformation has on the structure of rolled samples, homogeneity of deformation was assured in the upsetting process by employing the optimised lubrication technique (section 3.3.4.2). In addition, the same reheating and deformation temperatures, strains, strain rates, deformation sequences and holding times used in the rolling process were employed in the upsetting work.

The % reduction was varied from 20 to 60% (as in the rolling operation) by using cylindrical samples of varying initial heights and reducing each to the same final height of 8 mm to ensure the constancy of cooling rate. For accurate control of the strains, a deformation ring, ground accurately to a height of 8 mm, was used to stop the downward movement of the top platen. For multiple deformations, different rings of varying heights were used in succession, the last ring always being the 8 mm one. Upset samples were iced-brine quenched after a 10 second holding. For longer holding times, the upset sample was immediately returned into the reheating furnace, held isothermally there for the desired length of time, and then quenched in iced-brine. As in the rolling process, the true strain (ε) actually imposed in each case was evaluated using equation (63), section 3.4.2.

Upset samples which were used for $\gamma \rightarrow \alpha$ transformation studies were inserted into a NaCl salt bath maintained at 600°C in less than 2 seconds immediately after deformation or after holding for 20 s at the deformation

temperature, and held there for 20 hours to ensure complete transformation.

3.6 Study of Temperature Changes within the Material during Thermo-Mechanical Working

For monitoring the temperature changes within the material during hot deformation, three holes were drilled at one end face of a sectional bar for rolling in such a way that one hole was at the centre, one very close to the surface in contact with the top roll, and the third hole mid-way between the centre and the surface holes. Chromel-alumel thermocouples were inserted into these holes and their other ends connected to a three-pen chart recorder. This enabled the thermal history of the various zones of the material to be monitored during the reheating, rolling deformation, and quenching stages.

Temperature variations within the material in the upsetting process were similarly monitored with the modification that only two thermocouples - one inserted at the mid-point of the sample and the other very close to one of the end faces - were employed. In the plane-strain deformations on the servo-electronic machine, only the centre plane temperature history could be, and was, monitored.

3.7 Study of Mode of Deformation during Rolling

Two types of investigations were carried out to study the nature of deformation in the through-thickness of the material during rolling. In the first type, each of the mild steel samples containing rounded MnS inclusions was reheated at 1000°C for one hour, rolled over only half its length and the top roll raised so that the partly rolled material was withdrawn and subsequently air cooled. The undeformed and deformed MnS inclusions were later examined metallographically by obtaining appropriate sections, see Section 3.10.2.

In the second type, each sectional bar of the lead (grain-refined by a selenium addition) prepared for rolling, was cut into two halves across its length. The freshly cut end faces were accurately machined flat and further cleaned with a 600 μm silicon carbide paper. Grid lines at a spacing of 2.5 mm were inscribed on one of these cleaned end faces with a vernier scriber. A macrograph of the square grid network was taken at a magnification of x 8. The marked and the cleaned plain ends were painted with Pb/Sn solder paste and lightly held together inside a furnace at 200°C so that the two pieces became firmly soldered together. The

composite bar was later rolled at ~20°C to simulate hot rolling of steel because, as will be discussed later, the grain-refined lead deformed at 20°C simulates the behaviour of steel during hot working. The rolled composite bar was returned into a furnace at 200°C to melt the solder thus separating it into its two composite parts for examination, and taking of macrographs, of the deformed grid-pattern so that the strains suffered by each square (or rectangular) grid could be assessed.

3.8 PLANE STRAIN DEFORMATION PROGRAMME

3.8.1 The Computer-Controlled Servo-Hydraulic Machine and its Auxilliary Facilities

The machine used for the plane strain deformation is hydraulically driven and electronically controlled. It permits tight controls of strain, strain rate, holding time and quenching period after deformation, to be exerted. The major components of the machine are: a hydraulically driven ram capable of attaining a velocity of 1000 mm/s under a full load of ± 450 kN with a maximum stroke of 100 mm; a hydraulic pump which fills the accumulator of the system with oil; a specimen handling unit; and a pair of tools machined accurately to a width of 15 mm for the actual compression. The upper tool is attached to the ram while the lower tool is bolted to the machine bed through a temperature compensated load cell for monitoring load during deformation. The auxilliary equipment comprises a computer unit, a reheating and a deformation furnace, and a quenching unit. The general layout of the equipment is shown schematically in fig. 22.

The computer unit provides a command channel for carrying out the tests. A frequency clock in the electronic circuit enables displacement, load, and temperature to be collected at a desired interval during a test. A 2 Hz constant frequency graph plotter also in the electronic circuit, permits graphical representation of the basic test output results. The reheating furnace is mounted on a track set at 45° angle to the carriage of the specimen holding arms and is easily moved back and forward on this track. The testing furnace on the other hand, is immovable and surrounds the tools so that the deformation is carried out inside it. The quenching unit is located between the testing furnace and the specimen carriage track. It enables programmed quenching of deformed specimens to be carried out by water sprays.

3.8.2 The Plane Strain Testing Procedure

The specimen (fig. 18), of dimensions h_o = 10 mm and b_o = 50 mm, was coated with DAG 2626 lubricant on its central region. A Chromel-Alumel thermocouple was inserted into a 1.6 mm diameter hole drilled in the specimen centre at one end. The thermocouple leads were connected to an amplifier with a gain of 100. The specimen was placed in the slot of the 25% Cr - 20% Ni specimen holder cantilever arm and secured in this position by two pins (fig. 22). The arm was then rotated through 45° to face the reheating furnace and the furnace was in turn brought forward on its track so that the specimen lay in the furnace hot zone (fig. 22).

A temperature-time plotter was connected to monitor the heating temperature history. While the specimen was heating up, the following test data were entered into the computer using the teletype: specimen thickness and breadth, tool width, coefficients of friction and of spread, clock frequency, load range, amount of deformation, deformation velocity V_1, the approach velocity (V_2 = 1.1 V_1), holding time inside the testing furnace after deformation, and duration of water spray quenching.

The specimen attained the reheating temperature of 1100°C in ~6 minutes but soaking was carried out at this temperature for a further 24 minutes in order to take maximum amount of carbides and carbonitrides into solution. At the end of the 30 minutes (heating and soaking time), appropriate electrical connections were made, the hydraulic pump started, and the reheating furnace was pushed back so that the specimen carrying arm was rotated through 45° to face the deformation furnace directly. For a test at 900°C or 1000°C, the specimen was allowed to cool in air for 20 seconds before inserting it into the testing furnace, and for a test at 1100°C, only ~2 seconds of air cooling was allowed. After the appropriate air-cooling period, the computer was given a command to execute the test. This command signal gave rise to the automatic execution of the following actions in the outlined sequence: the specimen entered the testing furnace and stayed freely supported in between the tools for a period specified in the input data (180 secs for tests at 900°C and 1000°C and 60 secs for tests at 1100°C) during which the specimen attained the set test temperature; the upper tool pushed the specimen down on to the lower tool with a velocity V_2 and deformed it at a velocity of V_1 and then moved up so that the specimen springs up back to its original freely supported position between the tools; the specimen remained in this position for a specified time of 20 secs and is then moved out of the furnace to the

quenching position in ~0.2 secs; a microswitch was activated by a solenoid thus turning on a pump for the quenching spray to start; the quenching spray operated for a programmed time of 20 secs and then terminated; and finally the specimen moved back to its starting position.

Displacement, load and centre-plane temperature data were then punched out on paper tape to obtain a permanent record of the test. The final dimensions of the specimen were measured so that the coefficient of spread could be evaluated and used for the final calculations of equivalent true strain (eqn 46, section 2.3.3.2.1) and the converted equivalent flow stress in uniaxial compression (eqn 45, section 2.3.3.2.1) from the data in the paper tape. For stress computation, the computer first evaluates x_o from equation (50), section 2.3.3.2.2, and then selects the appropriate stress relationship based upon whether frictional conditions are fully slipping, fully sticking, or slipping-sticking. For maintaining a constant strain rate, the computer calculates a new velocity for the ram each time a pulse is detected in the variable frequency clock.

3.9 METALLOGRAPHY

3.9.1 Optical Microscopy

Using a water cooled slitting wheel, a longitudinal section of the rolled or upset-forged material was obtained in such a way that the face examined lay approximately in the mid-thickness plane of the deformed sample. Undeformed samples for determining the initial structure prior to deformation were similarly sectioned. The sections were generally cold mounted in resin and later ground and polished by standard manual techniques.

The ferrite-pearlite structure in air cooled or salt-bath quenched samples was revealed by etching in 2% Nital for ~15 to 20 seconds. The austenitic stainless steels were electrolytically etched in 50% concentrated Nitric Acid (after oxalic acid failed to give good results), using a STRUERS ELECTROPOL instrument, at a current density of ~17 mA/mm^2 for 35 to 40 seconds. For revealing the prior austenite grain boundaries from the Martensitic Structure of iced-brine quenched C-Mn and HSLA steel samples, the quenched samples were first aged at 500°C for 10 hours. The resulting precipitation of carbides, and segregation of impurities, at the austenite grain boundaries, facilitated the delineation of these boundaries. Samples so treated were electrolytically etched in a chromic phosphoric acid mixture consisting of: 200 ml of H_3PO_4, 50 gm of CrO_3, and

250 ml of H_2O. Etching for ~6 minutes at a current density of 34 mA/mm^2 gave satisfactory results.

3.9.2 Transmission Electron Microscopy

Thin foils were used to carry out transmission electron microscopical studies. Rods of 3 mm diameter with axes lying perpendicular to the face examined during optical microscopy were spark eroded from deformed specimens. Discs of 380 μm thickness were cut from these rods and foils of 200 - 250 μm thickness subsequently prepared from the discs. A solution consisting of 94 parts glacial acetic acid and 6 parts perchloric acid was used for jetting, at a current of 1.8 - 2 Amps at -40°C. Successful foils were examined on a JEM 100B Transmission Electron Microscope. This instrument has a day to day resolution of 50 Å and 1.2 x 10^3 to 500 x 10^3 times magnification potential.

3.9.3 Scanning Electron Microscopy

A Philips Scanning Electron Microscope [PSEM 500] was used to examine the surfaces of metallographically polished and etched samples. The Microscope was also equipped with a non-dispersive (EDAX) analytical device which was used to identify second-phase particles present in the microstructure.

Wavy bands, thought to be segregation, which were also observed in the austenitic stainless steel samples during optical microscopical examination, were analysed quantitatively on a Cambridge S4 Scanning Electron Microscope which incorporates a fully quantitative Energy Dispersive X-ray analyser linked to a mini-computer. An accelerating potential of 20 kV was used in the investigation.

3.10 QUANTITATIVE MEASUREMENTS

3.10.1 Grain Size and Subgrain Size Measurements

Grain size determinations were carried out on a Zeiss Optical Microscope using the mean linear intercept method. A set of eleven horizontal and eleven vertical lines inscribed on the screen of the microscope were used for the measurements so that several grains were covered at any one position examined. The measurements were made across the specimen's polished and etched face to determine grain size variation from surface to centre of the sample. At each depth from surface to centre, several positions were investigated longitudinally until 500-600 intercepts

were counted at that particular depth, care being taken not to count intercepts made by twin boundaries. The number of intercepts counted generally decreased with decreasing fraction recrystallised.

A tetrakaidecahedral grain shape was assumed and thus the grain size, d, was computed from the relationship:

$$d = 1.75\ (L/N) \quad \text{---------- (64)}$$

where L is the sum of the length of all the lines laid out and N is the total number of intercepts on L.

At the 95% confidence level, the relative error of these measurements was in the range ±1% to ±5%, the larger value being associated with measurements in materials with low fractions recrystallised.

The mean linear intercept method was also used to determine the average size of subgrains. Measurements were made on electron micrographs and computations were based on equation (64). In these measurements, the lines laid out were orientated in different directions to alleviate the effects of directionality of the subgrains.

3.10.2 Strain Distribution Measurements

In order to assess strain distribution in rolled and upset-forged samples, the aspect ratio of unrecrystallised grains, A_r, was determined from surface to centre of fully unrecrystallised specimens using the relationship

$$A_r = D_L/D_t \quad \text{---------- (65)}$$

where D_L and D_t are the average longitudinal and transverse diameters respectively of the pancaked γ-grains, determined using a relationship similar to equation (64).

The strain distribution in the rolled, gridded Pb/Se alloy, was computed by evaluating the strains suffered by each grid, from surface to centre of the sample, using the relationships:

$$\varepsilon_z = \ln(z_f/z_o) \quad \text{---------- (66)}$$

and

$$\varepsilon_x = \ln(x_f/x_o) \quad \text{---------- (67)}$$

where ε_z and ε_x are the true strains in the z and x directions

respectively, z_o and x_o are the initial and z_f and x_f are the final, dimensions of the grid in the z and x directions respectively, see Appendix 2.

For using the deformation of the Type I MnS inclusions in the mild steel samples to evaluate strain distribution in the steel, the MnS inclusions were assumed to deform into ellipsoidal volumes (see Appendix 3). The major and minor axes, a and b respectively, of the elliptical faces obtained from a longitudinal section of the inclusion ellipsoids were measured on a series of optical photomicrographs (printed to x 410 magnifications) taken at various positions within the sample. The measurements were made using an Anastigmatic Loupe having graticules graduated from 0 to ±25 mm. The Anastigmatic Loupe is fitted with a x 4 magnifier which has been corrected for aberrations. Thus, a flat field over the entire viewing area of the photomicrograph was obtained at a total magnification of x 1640 Generally, 200 to 300 inclusions, involving large and small ones were measured at each depth of the material to obtain a result at that depth. The plasticity index, ν, was evaluated using the relationship:

$$\nu = \frac{2/3 \ln \lambda}{\ln h} = \frac{\varepsilon_i}{\varepsilon_s} \quad \text{---------- cf eqn (4)}$$

where $\lambda = a/b$, $\varepsilon_i = 2/3 \ln \lambda$ being the true strain suffered by the inclusion and ε_s that suffered by the steel matrix (Appendix 3). The distribution of ε_i was used to characterise the distribution of ε_s for those deformation conditions where it was found that $\nu \cong 1$, that is, where the inclusion phase and the steel matrix deform by equal amounts.

3.10.3 Measurements of fractions Recrystallised

The fraction recrystallised X, denoted by f_x in the present work, was determined with an optical microscope fitted with a travelling stage which is controlled by a digital counter. By counting the number of points (P_x) lying in the recrystallised region using one unit cell of the counter and counting the number of points (P_{1-x}) lying in the unrecrystallised region using a separate cell of the counter, and obtaining the total of all points counted ($P = P_x + P_{1-x}$) in a separate cell, the fraction recrystallised, f_x, was evaluated from the relationship:

$$f_x = P_x/P \quad \text{---------- (68)}$$

Measurements were made from surface to centre, the value of P at each

depth being ~500. This produced a relative error of ±2% to ±5% at the 95% confidence limit, the higher relative error being associated with very low and very high values of f_x where the distinction between recrystallised and unrecrystallised gains is difficult.

3.10.4 Measurements of Migrating Boundary Area (S_{V_x})

The migrating boundary area per unit volume of austenite (S_{V_x}) was computed from the relationship:

$$S_{V_x} = 2\ (N'/L) \quad \text{---------- (69)}$$

where N' is the number of intercepts of boundaries separating the recrystallised and the unrecrystallised grains and L the total length of all lines laid out. This parameter S_{V_x}, has been utilised in the present work to deduce the distributions of the density of nucleation and the growth potential of recrystallisation nuclei, in the through-thickness of hot worked samples, at specified times after the hot deformation.

Equation (69) was also adapted to evaluate the prior γ-grain boundary interfacial area per unit volume of prior austenite (S_{V_o}), which is utilised later for correlating the recrystallised γ-grain size (d_{rex}) to initial structure of the material.

3.10.5 Hardness Measurements

Micro-hardness traverses were made from surface to centre of selected polished and etched specimens on a Reichert Mef equipment using a 30 gm load. Macro-hardness measurements were also made on polished and etched specimens on a Vickers diamond pyramid indenter with a 30 kg load.

In both the micro- and macro-hardness determinations, every single result was computed from the average of at least five readings.

CHAPTER 4: EXPERIMENTAL RESULTS AND THEIR INTERPRETATION

4.1 RESULTS OF LUBRICATION INVESTIGATION IN UPSET-FORGING

4.1.1 Fluid-Based Lubricants

Both the brushing and spraying methods of application of fluid-based lubricants failed to provide effective lubrication as adherence of lubricant onto the hot platens could not be achieved. Additionally, the graphite in oil generated objectionable fumes as the volatile matter in the mixture evaporated.

4.1.2 Solid Lubricants

4.1.2.1 Comparative Study of Graphite and Glass Lubricants

Fig. 23a shows a representative undeformed sample used for the investigation. With the end faces of the starting samples ground flat to $\nabla\nabla\nabla_8$ surface finish (see Section 3.3.4), the typical barrelled shapes are shown in figs. 23(b)-23(e) after upset-deformation without lubrication (23b), with a thin layer of graphite powder as lubricant (23c), with a thick layer of graphite (23e), and with glass powder lubricant (23d). It can be seen that the sample deformed with glass lubricant barrelled least, indicating that glass is a more effective lubricant than graphite. The high degree of barrelling of the sample deformed without lubrication (23b) or with a thin layer of graphite powder lubricant (23c), shows that these samples suffered the severest inhomogeneities of strain. This is substantiated by the external cracks which are visible in these specimens (Figs. 23b & c, arrowed features, A & B). Increasing the amount of the graphite layer resulted in a marginal improvement (fig. 23e), reflected only by the absence of external cracks and not the degree of barrelling.

The results presented qualitatively above are quantified by the barrelling factors, B_f, listed in Table 3 which show that B_f decreases with increasing lubrication efficiency, being least for the glass lubricated sample.

Deformation at various temperatures using a lime-soda window glass, pyrex glass, and an intimate mixture of both window and pyrex glass powders showed that the lime-soda window glass was most suitable for deformation in the 900-1000°C temperature range, the mixture of window and pyrex glass best for deformation in the temperature range of 1000-1100°C while the pyrex glass was most suited for deformation at temperatures above 1100°C.

4.1.2.2 Mode of Application of Glass Lubricant and the Influence of Glass Powder Grit Size

Investigation with various combinations of different grit size groups (Section 3.3.4.1) revealed that when the glass lubricant was applied by sprinkling over the bottom platen and on top of the heated sample, the grit size of the glass powder was important. The powder obtained by combining different grits whose composite size may be defined as d_g such that

$$75\ \mu m \leqq d_g \leqq 150\ \mu m \quad \text{---------- (70)}$$

gave better lubrication than all other grit sizes. The 'sprinkling' method however resulted in a build-up of ridges of sticky residues on the platen faces after sample deformation. In addition, the top face generally expanded more than the bottom face, fig. 23f.

Dipping the specimen end-faces into glass powder just prior to deformation produced unsatisfactory results because of insufficient pick-up of glass. Application of the glass powder by the plastic bonding method eliminated the problem of a build-up of sticky debris on the platen faces and also resulted in both end-faces of the upset sample expanding by equal amounts (fig. 24b).

The most significant improvement in the results was associated with the specimens whose end-faces were grooved, the spiral grooves furnishing the best results. It was found that the pitch of the spirals affected the lubrication efficiency, optimum performance being obtained with spirals of 0.625 mm pitch. Fig. 24c shows a spirally grooved sample which was lubricated by the plastic bonding technique. It can be seen that the amount of barrelling in the specimen is quite small compared with that in the ungrooved but similarly lubricated sample (fig. 24b). Fig. 24d shows the result obtained when the spirally grooved sample was lubricated using the optimised technique detailed in Section 3.3.4.2 which essentially consists of reheating the sample with glass powder plastically bonded to it and submerging it, after reheating, into a pool of molten glass maintained separately inside the furnace and then deforming the sample immediately. The absence of any observable barrelling in this sample indicates that it underwent homogeneous plastic deformation.

4.1.2.3 Transfer of Elemental Species from the Steel into the Glass Lubricant while Reheating Specimen in Glass

Results of the investigation into the change in colour of the molten glass from clear to pale green revealed the presence, inside the pale green glass, of about 2 ppm (2 parts per million) of Mn, 5 ppm of Fe, 10 ppm of Ni, and 10 ppm of Cr. Since the window glass used consists only of Fe_2O_3, SiO_2, Al_2O_3, Na_2O, K_2O, CaO, MgO and SO_3 (Table 4), it is clear that the Mn, Ni and Cr found in the glass came from the specimen into the molten glass during the reheating practice. Considering that the pyrex glass consists only of SiO_2, B_2O_3, Al_2O_3, Na_2O and K_2O, (Table 4), Fe, in addition to Mn, Ni and Cr must also have been introduced into the glass lubricant from the steel sample. As will be discussed, these elements probably came from oxide scale dissolved in the glass during reheating.

4.1.2.4 Effects of Strain, Temperature, and Strain Rate, on Heterogeneity of Deformation

Samples deformed to high or low strains in single deformation blows using the optimised lubrication technique underwent homogeneous deformation. However, from Fig.25 it can be seen that when deformation is carried out in single blows without applying any lubricant, inhomogeneity of deformation is highest at the highest strain of 60% reduction (fig.25b) and consistently lower as the strain is lowered(figs.25c&d). It must be noted that even at 20% reduction(fig.25d),the sample is significantly barrelled,showing that deformation is definitely,not uniform at that low strain. Table 3 shows that,for the stainless steel,a decrease in the deformation temperature from 1100°C to 1000°C increased barrelling(B_f) from 0.1065 to 0.1175;and a decrease in strain rate from $3.6s^{-1}$ to $0.97s^{-1}$ increased B_f from 0.1065 to 0.1356.

4.1.2.5 Effects of Scale and Material Type on Lubrication Efficiency and Homogeneity of Deformation

The results showed that interaction of undissolved scale with the viscous glass lubricant resulted in lubrication breakdown and hence inhomogeneous deformation. Considering material composition, it was found that, provided the scale was eliminated, the mild steel and C-Mn-**Nb** steel samples underwent homogeneous deformation more readily than the austenitic stainless and HSLA steels when subjected to the same deformation variables and lubrication conditions. Indeed, it can be seen from Table 3 that the B_f value for a mild steel sample is lower

than that for a stainless steel sample deformed under identical conditions.

4.1.2.6 Effects of Strain Rate, Multiple Deformation and Relubrication during a Multiple Deformation Sequence, on Lubrication Efficiency

A higher strain rate was found to enhance the efficiency of the glass lubricant probably due to the associated higher hydrodynamic action.

Samples lubricated in the optimised way and deformed in two or more blows without any relubrication between these individual blows underwent homogeneous deformation more readily than those deformed in single blows to the same strains provided that interdeformation times were small. Long periods between blows resulted in an increase in the viscosity of the molten glass lubricant and hence a lower lubrication efficiency. As will be discussed, temperature and scale/glass interaction can be invoked to explain this.

Fig. 26 illustrates the effect of relubrication during a multi-deformation sequence. Fig. 26b represents the homogeneously deformed sample obtained by deforming in one blow a specimen lubricated in the optimised way, 26c shows a sample deformed in two blows with relubrication in between the two deformation blows and 26d typifies the results obtained when deformation was carried out in three upsetting blows with relubrication after the first and the second deformation blows. It can be seen that the relubrication practice resulted in "reverse barrelling" of the samples, this effect increasing with the number of relubrication and deformation operations.

An interesting observation associated with the re-lubricated samples was the development of a shallow dish-like depression of up to 4 mm in depth at each end face (fig. 26e).

4.1.2.7 Effects of Friction Coefficient (μ) and Temperature Variations on the Expansion of the Specimen End Faces

Fig. 27ai shows the effect of maintaining a differential friction coefficient between the specimen's two end faces by lubricating the top face and leaving the bottom face unlubricated. It can be seen that the lubricated face expanded more than the unlubricated face. When a differential material/platen interface temperature was maintained by heating the top platen and not heating the bottom one, the specimen

end face in contact with the heated platen expanded only marginally more than the end face in contact with the cold platen. However, when a temperature gradient was induced into the material from only one end region (the bottom end) by dipping this end into ice-cold water for 2 seconds, the upset sample, shown in fig. 27aii, acquired a differential end region expansion similar to that observed in the differentially lubricated sample, fig. 27ai. The cooled end expanded significantly less than the uncooled end, fig. 27aii.

It can be seen that the sample in Fig. 27aii is slightly less deformed than the sample in fig. 27ai. This was because, although the same 8 mm high deformation ring was used in both cases, the through-thickness temperature gradient resulted in a relatively high increase in the material mean flow stress (resistance to deformation) and so deformation to the ring height did not occur before the force-build up on the press exceeded the pre-set compressive force capacity (section 3.5.1). Increasing the one-sided temperature gradient by dipping in the ice-cold water for 5 seconds reduced further the extent of deformation suffered by the material (fig. 27bi), keeping the pre-set applied compressive force unchanged. A further reduction in deformation occurred when the dipping period was increased to 10 s (fig. 27bii). It may be seen that a better defined conical shape accompanied the longer cooling periods, figs. 27bi & bii. A repeat showed that the results were reproducible (compare fig. 27bii with fig. 27biii). It must be noted that all samples used for studying the differential temperature effects were deformed without lubrication.

4.1.2.8 Condition of the Specimen End Faces before and after Upset-Deformation

The flat, end surfaces of the specimens prior to deformation in the ungrooved, $\nabla\nabla\nabla_8$ surface finish condition,and the 0.625 mm pitch spirally grooved condition,are shown in figs. 28ai and aii respectively. Figs 28bi and 28bii show the ungrooved and grooved faces respectively after both samples had been identically lubricated and subsequently deformed to the same strains. It can be seen that the expansion of the ungrooved face (fig. 28bi) is much less than that of the spirally grooved face (fig. 28bii) despite the entrapped glass lubricant under the former's face. This indicates that the lubrication role of the spiral grooves is not merely to entrap lubricant under the specimen during deformation as will be discussed later.

Another feature of the ungrooved surfaces is the development of a circular band near the periphery, fig. 28bi. Similar bands also occurred in spirally grooved samples which were not efficiently lubricated, figs. 28biii and 28ci. Fig. 28biii suggests that these bands are not part of the original end faces but rather formed by the rolling over of the vertical sides. However, the region marked P in fig. 28ci reveals that grooves placed on the specimen end face prior to deformation are observed in the circular bands after deformation thus contradicting the above suggestion.

Figs. 28di and dii show the lubricated (top) and the unlubricated (bottom) faces respectively, of the sample shown in fig. 27ai. It can be seen that the unlubricated face (28dii) was severely restricted from expansion while the lubricated face (28di) expanded much more freely albeit not to the same extent as would be expected if deformation were homogeneous (fig. 28cii). It may be noted that despite the drastic rolling over of the vertical sides towards the bottom (unlubricated) face, these vertical sides did not form part of the deformed end surface, fig. 28dii.

4.2 RESULTS OF INVESTIGATIONS INTO TEMPERATURE DISTRIBUTION WITHIN THE MATERIAL DURING HOT WORKING

4.2.1 Temperature Changes during Hot Rolling

The temperature histories of the surface skin, sub-surface, mid-plane between the centre and the surface, and the centre-plane of the material under various rolling conditions and using different specimen dimensions, are summarised graphically in figs. 29-34. The maximum (and minimum) temperatures attained at the various planes are listed in Tables 5a and 5b. In all the cases, a temperature difference of ~10 - 12°C exists between the centre and the sub-surface (0.5 mm below the surface) just before the material enters the rolling pass.

Fig. 29 and Table 5a show that rolling at 3.6 s^{-1} to 60% reduction in one pass after reheating to ~1100°C resulted in temperature rises of ~27°C and ~16-18°C at the centre and intermediate planes respectively; and temperature falls of 300°C and 675°C at the sub-surface (fig 29a) and surface (fig. 29b) planes respectively. It can also be seen that holding in air after deformation led to a recuperation process which ultimately resulted in thermal equilibrium between the centre, intermediate and sub-surface planes, at a temperature in excess of 100°C below the entry temperature.

The surface skin did not attain thermal equilibrium with the other planes during the air-cooling although its temperature drop of ~675°C recovered by ~32°C.

The effect of strain on the temperature changes is illustrated in fig. 30 from which it can be seen that reducing the strain reduces the temperature rise at the centre and intermediate planes and also the drop in sub-surface temperature. From figs. 29a and 30a-c, and Table 5a, it can be seen that reducing the strain from 60% reduction(fig.29a) to 50%(fig.30a) 38.5% (fig. 30b) and 20% (fig. 30c) resulted in reductions in the centre-plane temperature rise from 27°C to 19°C, 14°C and 2°C respectively and also reductions in the intermediate-plane temperature rise from ~17°C to 13°C, 2°C and 0°C respectively. The sub-surface temperature drop was equally reduced, from 300°C to 175°C, 69°C and 88°C respectively. In all cases however, thermal equilibium between the various planes was attained upon subsequent holding in air.

Fig. 31 illustrates the influence of strain rate. Comparing each of figs 31a & b with fig. 29a, it can be seen that increasing the strain rate from 3.6 s^{-1} (fig. 29a) to 18 s^{-1} (fig. 31a) increased the centre and intermediate plane temperature rises from 27°C and 17°C respectively to 63°C and 50°C respectively (Table 5a). In addition, the sub-surface temperature, instead of falling immediately on entry into the pass (fig. 29a), exhibited an upward transient, of ~38°C, for an extremely small time interval and then dropped to a minimum value of 25°C below the mean entry temperature (fig. 31a). Air cooling ultimately resulted in the attainment of thermal equilibrium of all the planes at only 20°C below the entry temperature but prior to this thermal equilibrium, the temperature of the intermediate-plane tended to overshoot the centre-plane temperature which had all along been higher (fig. 31a). Rolling at a lower strain rate (0.97 s^{-1}), fig. 31b, had reverse effects in that there was only a mere 12°C temperature rise at the centre-plane, a fall (rather than a rise) of 180°C at the intermediate-plane and a severe temperature drop (355°C) of the sub-surface plane (0.5 mm below the surface), see table 5a. In addition, thermal equilibrium during air cooling was attained at a much lower temperature, 200°C below the entry temperature, fig. 31b.

The effects of a multi-pass rolling sequence are illustrated by the graphical results of a four-pass schedule shown in fig. 32. The maximum

and minimum temperatures attained at each plane during each deformation pass are included in Table 5a. From this Table, it can be seen that the centre-plane temperature rose by 12°C, 20°C, 32°C, and 39°C in the 1st, 2nd, 3rd and 4th deformation passes respectively. Similarly, the temperature rise at the intermediate-plane increases consistently from the first to the last deformation pass, Table 5a. Also, the temperature drop at the sub-surface plane gets bigger from the first to the last pass, being 105°C, 119°C, 129°C and 133°C in the 1st, 2nd, 3rd and 4th deformation passes respectively. On the other hand, the difference between the entry temperature to each pass and the recuperated thermal equilibrium temperature after that pass consistently decreases from the first to the last pass, being 60°C, 50°C, 43°C and 25°C for the 1st, 2nd, 3rd and 4th deformation passes respectively.

The results presented so far were obtained using the normal rolling samples of 20 mm width and varying thickness of 20 mm to 10 mm (Section 3.2.3). In order to study the effect of specimen size, tests were carried out with specimens of 65 mm width x 16 mm thickness. The results obtained for single and multiple pass rolling schedules are included in Table 5b and graphically presented in figs. 33 and 34 respectively. Considering the single pass schedule, it can be seen that, as in the previous results (fig. 29), the surface skin temperature dropped drastically (by ~600°C), fig. 33b; the sub-surface temperature also suffered a significant drop while the intermediate and centre planes experienced temperature rises of ~22°C and 35°C respectively, Table 5b and fig. 33. Air cooling resulted in the thermal equilibrium of all planes except the surface skin, fig. 33. In the multiple pass (fig. 34) the temperature rise at the intermediate and centre planes increases from the first to the last pass, being 16°C and 6°C respectively in the first pass and 22°C and 20°C respectively in the last (2nd) pass. On the other hand, the sub-surface temperature drop relative to the entry temperature to the pass diminishes from the first to the last pass, being 92°C and 51°C in the 1st and 2nd passes respectively. Also, the difference between the equilibrium temperature during air-cooling and the entry temperature to the pass decreases from the first to the last pass, being 41°C and 21°C in the 1st and 2nd passes respectively. These results, apart from the decrease in the sub-surface temperature drop from the first towards the last rolling pass, are in good agreement with those obtained in the multiple-pass rolling schedule using the smaller samples (compare fig. 34 with fig. 32).

4.2.2 Temperature Variations during Hot Upset-Forging

The temperature variations at the centre and sub-surface planes of the material during upset-forging under various deformation and lubrication conditions are summarised in Table 6, and presented graphically in figs. 35-40. As in the rolling process, a temperature difference (of $\leqq$~10°C) develops between the centre and the sub-surface prior to the onset of the upsetting-deformation.

Figs. 35a-c illustrate typical results obtained when deformation was carried out in single blows with cold platens and no lubrication. Similar to the rolling results (fig. 30), the centre-plane temperature rise decreases with a decreasing strain, being 32°C, 14°C, and 2°C for 60%, 38.5% and 20% reductions respectively, Table 6. Also, as in the rolling process, the sub-surface temperature drastically falls, although, in contrast with the rolling process, this sub-surface temperature drop seemed not to be affected significantly by reductions in strain, fig. 35. Fig. 36 shows that lowering the strain rate [from 3.6 s^{-1} to 0.85 s^{-1}] drastically reduced the temperature rise at the centre while increasing the sub-surface temperature drop. Distributing the total strain (60% reduction) into five smaller contributary strains in a multiple deformation schedule, fig. 37, reduces both the temperature rise at the centre and the temperature drop at the sub-surface during each deformation. In all these cases (figs. 35-37), air cooling gradually leads to thermal equilibrium.

Fig. 38 shows that deformation without lubrication but with the platens heated to 550°C resulted in a temperature rise (32°C) at the centre-plane equal to that observed in the sample deformed with cold platens (fig. 35a). However, the sub-surface temperature drop was drastically reduced, being only 25°C as against ~110°C in the cold platen case. In addition, the sub-surface temperature overshoots the centre-plane temperature during the very early stages of air cooling and then gradually falls so that thermal equilibrium between both planes is ultimately attained.

The results obtained when deformation was carried out to different strains using the optimised lubrication technique (and with the platen surface temperatures maintained at 550°C) are shown graphically in fig. 39 and included in Table 6. It can be seen from these that the application of lubrication did not alter the magnitudes of the centre-plane temperature rises, these remaining at 32°C and 14°C for 60% and 38.5%

reductions respectively as for the unlubricated cases (figs. 35 a & b, and fig. 38). On the other hand, the sub-surface temperature drop was significantly reduced, with the result that air-cooling led to the sub-surface temperature becoming higher than the centre-plane temperature (figs. 39 a & c) prior to the attainment of thermal equilibrium. When however the sample was left to dwell on top of the bottom platen after deformation, the sub-surface temperature continued to fall (fig.39b) instead of rising to exceed the centre-plane temperature.

The results presented so far in this section were obtained using type 304 austenitic stainless steel samples (cast 9). Tests were conducted using mild steel samples (cast 11) to investigate the influence of material type on the internal temperature variations during hot upsetting. The results obtained using cold and heated platens but no lubrication in either case, are presented graphically in figs. 40a-c and incorporated into Table 6. It can be seen that the results are essentially similar to those obtained with the stainless steels, one significant difference being that the drop at the sub-surface plane is larger in the mild steel than in the stainless steel.

Fig. 40c shows that a dwell-time of ~2.5 seconds of the upset sample on the hot (550°C) platen after deformation resulted in a further drop in the sub-surface temperature of ~44°C.

4.2.3 Temperature Variations during Plane Strain Deformation

The temperature measuring device of the electrohydraulic machine used for the plane strain deformation tests was designed to be able to monitor only the centre-plane temperature of the material. Consequently, only the centre-plane temperature histories were monitored in these tests.

Fig. 41 illustrates a typical centre-plane temperature variation for a material reheated to 1100°C (point A), cooled in air for ~36 seconds (A to B) and then inserted into a furnace held at 900°C where it gradually attained the deformation temperature (B to C). In the figure, CD represents the steep temperature rise which occurred during the deformation, DE the gradual fall in temperature down to the furnace temperature (900°C) within 20s of isothermal holding of the deformed sample, and EF represents the steep fall in the temperature during water-spray quenching outside the deformation furnace.

The variation of the centre-plane temperature rise (during the deformation) with strain rate is illustrated in fig. 42 which shows the results for deformations at 1000°C with strain rates of 1 s^{-1} (fig. 42a), 13 s^{-1} (fig. 42b) and 26 s^{-1} (fig. 42c) respectively. It can be seen that increasing the strain rate increases the amount of temperature rise. It can also be seen(fig.42c) that the 20s isothermal holding time was not enough for the centre of the material deformed at the highest (26 s^{-1}) strain rate to return to thermal equilibrium with the furnace. A further characteristic of each of the tests at a higher strain rate (> 1 s^{-1}) is that the centre-plane temperature rise is depicted as a vertical straight line (figs. 42 b & c) as a result of the low speed of the temperature pen recorder compared with the high rate of plastic deformation and the associated high rate of temperature rise. Thus figs. 41 and 42 cannot give any meaningful direct information about the progressive rise in temperature as deformation proceeds. Such information is given in figs. 43-47 which show the temperature rise during the plastic straining as a function of true strain, for different materials, each tested under various combinations of hot working variables.

In general, the figures (figs. 43-47) show that the centre-plane temperature rises with increasing straining due mainly to work done by mechanical deformation and to a lesser extent heat released by dynamic recrystallisation. Also, close examination of each set of the curves in figs. 44-47 reveals that the magnitude of the temperature rise is raised by a higher strain rate at a given deformation temperature, and a lower deformation temperature at a given strain rate. Comparing the curves for the niobium-free austenitic stainless steels (fig. 44) with their corresponding curves for the 0.45% Nb-bearing austenitic stainless steel (fig. 45), it can be seen that the addition of Nb also raises the magnitude of the temperature rise under a given set of deformation conditions. A similar conclusion applies when the results for the Nb-free C-Mn steel (fig. 46) and the 0.055% Nb-C-Mn steel (fig. 47) are compared. It may further be seen that the temperature rises associated with the stainless steels are higher than those associated with their non-stainless steel equivalents (compare fig. 44 with fig. 46, and fig. 45 with fig. 47). As will be discussed later, these higher temperature rises can be related to higher flow stresses. It should be noted that the centre-plane temperature rise does not attain its maximum value at the peak stress (σ_p) but rather continues to rise until a much higher strain with an associated lower stress ($< \sigma_p$) has been reached,

fig. 43. Ultimately, a steady state centre-plane temperature, corresponding to the steady state flow stress, is attained and so the centre-plane temperature remains practically constant as strain is further increased (figs. 43-47).

4.3 RESULTS OF STUDIES INTO THE MODE OF PLASTIC DEFORMATION AND MATERIAL FLOW DURING HOT ROLLING

4.3.1 Aspect Ratios of Unrecrystallised Austenite Grains

Optical microscopical examination of cast 5 rolled at 1000°C in one pass with a strain rate of $3.6s^{-1}$ to a strain of 0.94(60% reduction) showed a marked structural variation from the surface-plane to the centre-plane of the material. This is illustrated in fig. 48, from which it can be seen that the unrecrystallised γ-grains near the surface and the centre are less deformed than those in the intermediate plane. In order to confirm this observation, cast 3 which has a coarser structure than cast 5 was rolled at 900°C with $\dot{\varepsilon} = 1\ s^{-1}$ to various strains in one or two passes. Aspect ratios of the resulting unrecrystallised γ-grains were measured in the surface, intermediate, and centre planes. The results, summarised in Table 7 are presented graphically in fig.49. It can be seen that at low(20%) and high (60%) reductions, deformation is least within the surface region, maximum at the intermediate-plane, and moderate at the centre-plane.

4.3.2 Deformation of Gridded, Grain-refined Lead

After hot rolling (at 20°C with $1\ s^{-1}$) of the composite lead block (fig. 50b) produced by soldering together the plane and marked end faces of the two separate blocks A and B (fig. 50a), the external surfaces of the rolled bars at the regions of joining were examined under a low power microscope and those with cracks indicating a separation at the point of soldering were discarded while those found flawless were separated into their two composite parts A & B (fig. 50c) for detailed studies of the deformed grids. It was also observed that, after separating the bars which had no surface defects, a very close fit existed between the two end faces at the plane of soldering.

As shown in fig. 50c, the plane of soldering which was vertical prior to rolling (fig. 50b) became curved after rolling, in a direction opposite to the rolling direction. All the vertical lines such as CC (fig. 50d) of the gridded end face became curved opposite to the rolling direction resulting in a depression in the gridded part, B. In addition,

the vertical lines on either side of the central one, bulged outwards somewhat symmetrically about this central line. Each line bowed out more at its centre than at its ends, resulting in the plan view of the gridded face which was initially square (fig. 50d) taking up a barrel-shape (fig. 50e). Examination of the lines such as XX (fig. 50d) which were straight, horizontal and parallel to one another prior to rolling, showed that, after rolling, they moved closer to each other as a result of the vertical compressive force, stretched outwards due to lateral spread, and curved symmetrically about the central line D'D' (fig. 50e) towards the rolled faces.

The inward curvature of the central vertical line C'C' which did not suffer any lateral displacement was investigated by measuring its depth at various positions across the sample face using an S.I.P. (Societe Internationale de Physique) Universal Measuring Machine (Type MU 214B) equipped with a locating microscope. The results, presented in fig. 51, show that the curvature is reasonably parabolic.

The strains ε_x and ε_z in the x and z directions respectively, suffered by the various grids, after a strain of 0.288 (~ 25% reduction) on the bar, were computed. Columns of grids (eg column a_1, a_2, ...a_5 see illustrative diagram Annexed to fig. 52) on either side of the vertical centre-plane were first considered and the strains on each grid in the column as well as the distance of that grid from the rolled surface of the bar were evaluated. These data, summarised in Table 8a, are presented graphically in figs. 52a & b for columns of grids on the left (fig. 52a) and right (fig. 52b) sides of the centre-plane. Apart from differences in the scatter of the points in the two curves, they are basically similar in shape. Both curves show that the plane between the surface and centre planes was the most severely deformed. The centre-plane appears to have deformed more than the surface-plane but this result could have been significantly affected by the relatively higher errors in measuring z_f at the centre where the surface curvature (fig. 51) was greatest, being in fact the vertex of the parabolic curve formed by the surface depression. All the data points in figs. 52a & b were summed up and averaged by evaluating $\bar{\varepsilon}_z$, the mean of all ε_z on all grids such as d_1, c_1...a_1,a_1', ...c_1', d_1' (see diagram Annexed to fig. 52) which form a row. The results, shown in Table 8b, are presented graphically in fig. 52c. As expected, fig. 52c has a similar shape to those of figs. 52a & b. Values of ε_x, also included in Tables 8a & b, are similarly presented graphically

in figs. 52 d & e as functions of grid distances from the rolled faces of the sample. Fig. 52d is the counterpart of fig. 52a and so each curve represents the variation of ε_x from centre to surface for each column of grids considered. Fig. 52e is the graphical average of all the data points in Fig. 52d and those for the right hand side grids (figure not shown). It can be seen (from figs. 52 d & e) that each of ε_x and $\bar{\varepsilon}_x$ varies parabolically within the sample thickness, rising from a minimum value at the surface-plane to a maximum at the centre-plane. Fig. 52d also reveals that the values of ε_x for grid columns near or at the centre-plane of the sample are lowest while the values for grid columns (such as c_1, c_2, ...c_5 and c_1', c_2', ...c_5' (see diagram annexed to Fig. 52) which are located ~3/4 away from the centre are highest. ε_x values on the grid columns nearest to the specimen sides generally lie between the ε_x values of the centre and intermediate planes.

The foregoing procedures were repeated for the sample rolled to a bulk strain of 0.509(39.9% reduction)and that rolled to ε=0.94(60.9% reduction). Results for the 39.9% reduction are summarised in Tables 9a & b and presented graphically in figs. 53a-c while those for the 60.9% reduction are listed in Tables 10a&b and shown graphically in figs. 54a-d. Comparing figs. 53a&b and 54a with figs. 52a&b, and also figs. 53c and 54b with fig. 52c,it can be seen that at the higher strains,ε_z at the centre tends to be higher than the ε_z values at the surface-plane, the ε_z in the intermediate plane still being the maximum.A comparison of figs.53d&e and 54c&d with figs. 52 d & e reveals that increasing the bulk strain simply reduces the scatter in the variation of ε_x within the sample thickness: the parabolic shape of the curve is not altered.

In general, it can be seen from the results(Tables 8-10)that ε_z values are consistently higher than the corresponding ε_x values at all bulk strains. The standard deviations of the computed ε_z and ε_x values were found to be reasonably small.

4.3.3 Deformation of Inclusions in Hot Rolled Mild Steel

4.3.3.1 Type, Morphology, and Size of Inclusions Present in the Steel

Figs. 55a & b show that type I MnS inclusions predominantly formed. It can also be seen from fig. 55a that, although a few oval-shaped (B) MnS inclusions are present, most of the others are practically spherical (A & C). Also, while majority of the MnS inclusions are single-phase (fig. 55a, A and fig. 55b, E) some others contain a dark sport (features C & D

in figs. 55a and 55b respectively) which was identified by EDAX analysis techniques as Manganese Silicate. It was also observed that the distribution of the MnS inclusions within the steel bulk was fairly uniform. The size, with the associated standard deviation and coefficient of variation, of the spherical MnS inclusions in each cast ingot is summarised in Table 11. It can be seen that the mean size increases with increasing cross-section of the cast ingot and that although the standard deviations vary, the coefficient of variations from cast to cast are practically similar.

In addition to the MnS inclusions, silicate inclusions were occasionally observed despite the small amount of silicon added to the steel. Some of these manganese silicate inclusions contained lighter coloured phases in their interior while at their exterior a similar lighter coloured phase forms a circumscribing case broken at a few points. These special features are not of direct relevance to the present work and will therefore not be discussed any further in this thesis.

4.3.3.2 Deformation Characteristics of the Inclusions

At the low matrix strain of 0.23, the few manganese silicates remained rigid. Increasing the matrix strain led only to the formation of conical voids around bigger inclusions. As the strain was increased further (to ~0.92), some of the inclusions fractured, the fragments of the fractured inclusions generally being aligned parallel to the plastic flow direction. Some others still remained rigid with their associated conical voids. These observations will not be discussed further in the present work as they are not directly relevant to the general theme of the research and, the subject has been treated exhaustively elsewhere.[60]

In contrast to the silicates, the MnS inclusions deformed plastically into ellipsoidal volumes at strains of 0.23 to 0.49, the ellipsoidal shape being approximately maintained even at the high matrix strain of 0.92 (fig. 56a). At higher strains (> 1.0), the MnS inclusions were generally deformed into elongated ribbons (fig. 56b). Other special features observed were the coalescence of adjacent MnS inclusions (fig. 57) at high matrix strains ($\varepsilon > 1.1$) and the bending of some MnS inclusions in the direction opposite to the rolling direction (fig. 58) at intermediate values of matrix strain ($\varepsilon = 0.49$).

Computed mean values of the inclusion aspect ratios $\bar{\lambda}$, true strains ε_i, and

plasticity indices ν, for bulk (steel matrix) strains, ε_s = 0.10 - 1.61 (9.5 - 80% reduction) are shown in Table 12. The influence of inclusion size variation from cast to cast (Table 11) was eliminated by varying ε_s along the same sample through making measurements at different positions from entry to the exit plane of the sample rolled only to half its length (see sketch incorporated into Table 12). It can be seen from Table 12 that ν is highest (3.48) at the lowest matrix strain (ε_s = 0.1) indicating greater deformation of the MnS inclusions relative to the steel matrix. Increasing ε_s decreased ν and at ε_s = 1.16 (~ 68.8% reduction), ν was just above unity (1.04) while at ε_s = 1.61 (~80% reduction), ν was just less than unity(0.94). Thus the inclusions and the steel matrix deform by practically equal amounts in the region of the sample where $1.0 < \varepsilon_s < 1.6$. A similar analysis on the sample with a smaller starting cross-section (20 mm x 20 mm) for a 60% rolling schedule showed that ν approximates to unity only in the fully rolled region where ε_s = 0.92 (~ 60% reduction).

4.3.3.3 Pattern of Deformation of the MnS Inclusions at Various Positions from Surface to Centre of the Steel Sample

In order to obtain a complete description of the pattern of deformation during the rolling process, the longitudinal sections of the samples rolled to half their lengths in the 60% and 80% reduction schedules were examined in detail from the plane of entry to the plane of exit. At each plane considered values of ε_i were evaluated in the through-thickness direction of the sample (from one surface to the other).

The results, summarised in Tables 13 & 14 show that, within about 0.1 - 0.3 mm of the plane of entry (where $\varepsilon_s \leq$ 9.5% reduction), only the MnS inclusions within 0 - 0.5 mm from the rolled surface underwent plastic deformation, the elongation axis being generally aligned with the curvature of the arc of contact. The MnS inclusions below this depth from the surface remained undeformed. As ε_s progressively increased (towards the exit plane), the MnS inclusions in the surface region suffered relatively smaller additional deformation while those in the central regions became more deformed. Thus, as illustrated by figs 59a-c for the 80% reduction scheme, the MnS inclusions became generally drawn out into ribbons in the portions of the material which had passed fully out of the exit plane. It can also be seen from fig. 59 that the MnS inclusions at the surface (59a) are less elongated than those in the central region (59 b&c).

Graphical representations of the variations of ε_i in the through-thickness direction of appropriate samples for matrix strains where ν were found to be close to unity (Table 12), are shown in figs. 60a-c. It can be seen from these curves that, in each case, the MnS inclusions at or near to the surface deformed least, those situated between the surface and the centre generally deformed most, and those at the centre deformed more than those at the surface but less than those at the intermediate plane between the surface and the centre. It can also be seen that the scatter in the data points decreased as ε_s increased. At the highest ε_s value (1.61) examined, where ν is indeed less than unity, deformation tended to be concentrated more around the central regions, thus resulting in a curve almost parabolic in shape (fig. 60c). It must be noted that the aspect ratios (λ) of the MnS inclusions exhibited similar variations within the sample as their associated ε_i but the data points showed considerably higher scatter.

Transverse sections at various positions of the rolled bars showed the MnS inclusions as elliptically shaped. The mean aspect ratios and the true strains (termed lateral strains), determined in such sections, were denoted by $\bar{\lambda}_x$ and ε_{ix} respectively and summarised in Table 15. The data is presented graphically in fig. 61 from which it can be seen that the variation of ε_{ix} within the sample is essentially similar to that of ε_i (compare fig. 61 with fig. 60). It can also be seen from fig. 61 that the variation of $\bar{\lambda}_x$ within the sample is somewhat similar to that of ε_{ix}, characterised by low values at or close to the surface and generally higher values towards the central zones, with a downward dip at the centre-plane proper. The higher amount of scatter of individual points in the $\bar{\lambda}_x$ variation accounts for the use of the shaded band-graph, fig. 61, $\bar{\lambda}_x$.

4.4 RESULTS OF MICROSTRUCTURAL STUDIES

4.4.1 Microstructural State of the Material Prior to Reheating

Fig. 62 shows the ferritic structure with uniformly dispersed areas of unresolved pearlite of a C-Mn-0.095%Nb steel (cast 16) homogenised at 950°C for one hour and air cooled. It can be seen that the structure (fig. 62a) developed when the homogenisation was preceded by solution treatment at 1300°C is coarser, with mean grain size of 28 μm, and also more heterogeneous than the structure (fig. 62b) developed when no previous solution treatment was carried out, the mean ferrite grain size being 23 μm in this latter case.

Due to the above effect which was observed even in a relatively high Nb-steel, then, subsequently, in order to avoid the coarse and non-uniform initial grains associated with the high temperature solution treatment, the austenitic stainless and C-Mn-Nb steels were homogenised at 1000°C and 950°C respectively without prior solution treatment. This resulted in the presence of undissolved niobium carbide/nitride particles (fig. 63) in the Nb-bearing austenitic stainless steels.

4.4.2 Microstructural State of the Material after Reheating at 1100°C for Deformation

4.4.2.1 Dissolution of Nb(C,N) Particles and Uniformities of Austenite Grain Size and Macro-Hardness within the Sample

After reheating to 1100°C, the large Niobium Carbide/nitride particles in the stainless steels (fig. 63) were no longer observed. As illustrated in figs. 64a & b for the 0% and 0.48%Nb stainless steels respectively, the austenite grain size developed from surface to centre of the sample was practically uniform. However, highly segregated, Nb-rich areas, surrounded by ultra-fine austenite grains, were occasionally observed in the stainless steels with $\geq$0.20%Nb.

The C-Mn base and 0.045%Nb steels also exhibited surface-to-centre prior austenite grain size uniformity. Figs. 65a & b illustrate typical structures observed from surface to centre of the base steel and the niobium steel respectively. The C-Mn-Nb steel however contained a few areas of mixed grain size (fig. 65c). The macro-hardness values in the through-thickness of each sample were also found to be practically uniform.

4.4.2.2 Influence of Reheating Temperature, Niobium Addition, and Preliminary Ingot-Rolling Schedule on the Prior Austenite Grain Size

Typical variation of prior austenite grain size, d_o, with reheating temperature is summarised in Table 16 for a Nb-free stainless steel, cast 9, and presented graphically in fig. 66. The figure shows that d_o increases with increasing reheating temperature, the increase being gradual in the 1000-1150°C temperature range and more rapid in the 1200-1300°C temperature range. The associated grain boundary area per unit volume of prior austenite, S_{V_o}, and the mean macro-hardness, H_v, also included in Table 16, are shown in figs. 67a & b respectively as functions of d_o. It can be seen that both S_{V_o} and H_v decreased exponentially as

d_o increased, with H_v tending to a constant value at $d_o \geqslant \sim 200$ μm.

The micrographs in figs. 64 & 65 show that niobium refined d_o in both the stainless steels (figs. 64a & b) and the C-Mn steels (figs. 65a & b), the refinement increasing with increasing amount of Nb-additions. This effect, summarised in Table 17, is illustrated graphically in figs. 68a&b for the stainless steels and C-Mn steels respectively. Nb additions also led to increased twinning frequency (compare fig. 68ci with 68cii) and to a progressive increase in mean hardness (fig. 69).

For casts of identical chemical composition, the preliminary ingot rolling schedule had effects on d_o even after subsequent identical thermal treatments. Figs. 68a & b illustrate this effect for the stainless steels (68a) and the C-Mn steels (fig. 68b). In each figure, materials rolled to square sections (curves A_1&A_2) acquired larger d_o than those rolled to flats (curves B_1 & B_2). Even materials rolled to identical dimensions but with different rolling schedules developed different d_o values. This, as discussed in section 5.4.1.1 explains the wide difference in d_o values of cast 1 and cast 9 which have identical chemical composition, even when both were rolled to identical dimensions (Table 17).

4.4.3 Dynamic Structural Changes during Hot Working

Typical substructures and subgrains developed in the stainless steels after rolling at three different temperatures to a strain of 0.94 in one or two passes are illustrated in figs. 70a-e for cast 5. It can be seen that rolling at 1000°C resulted in a higher dislocation density (fig. 70a) than a rolling temperature of 1100°C (70b) and at the former temperature, the dislocation was also more tangled and cellular. A comparison of fig. 70c with fig. 70b shows that a multiple pass has a similar effect to a low rolling temperature. In all cases, the dislocations were concentrated at the sub-boundaries. Apart from the cellular arrays of dislocations, other sub-structures observed included: networks of dislocations at sub-boundaries (at rolling temperatures $\geqslant$1050°C) and deformed sub-structures (at temperatures $\leqslant$ 1000°C).

The subgrain size, d_{sg}, summarised in Table 18 for the single and double pass rolling sequences, is presented graphically in fig. 71 which reveals an inverse linear relationship between $\ln d_{sg}$ and $(1/T)\times10^4$ °K.

Figs. 70d & e show recrystallised grains containing dislocations.

4.4.4 Static Structural Changes during Hot Working

4.4.4.1 Static Recovery

Static recovery was monitored in the stainless steels by Vickers hardness measurements. Typical hardness variations with isothermal holding time, t, are listed in Table 19 and presented graphically in fig. 72a for casts 1 and 3. It can be seen that the hardness decreased with increasing t, the decrease being small and gradual up to 100s and then very sharply from t = 100s to t ≅ 300s. From t ≧ 300s, the hardness values tended to level out. Static recovery accounts for the initial gradual decrease while static recrystallisation and grain growth account for the sharp decrease and constant value respectively. This is substantiated by the micrographs in figs. 72b(i-iii) which show that static recrystallisation just started to occur after 100s holding (72bii) and that grain growth had indeed occurred after recrystallisation (fig. 72biii).

4.4.4.2 Static Recrystallisation of the Austenitic Stainless Steels after Hot Rolling or Hot Upset-Forging

4.4.4.2.1 Nucleation and Growth of new, strain-free, γ-Grains

Typical preferred nucleation sites observed in the stainless steels are illustrated in fig. 73 for cast 1 deformed by rolling in one reduction schedule to 60% (73Ia-c) and to 38.5% (73II), and by upset-forging to 60% (73III). It can be seen that nucleation occurred predominantly at serrated γ-grain boundaries (fig. 73Ia) and triple junctions of deformed γ-grains, the latter being more important at the lower strain (fig. 73II). Nucleation also occurred at non-coherent interfaces of twins (fig. 73Ib), deformation bands (fig. 73Ic), within the grain interior (fig. 73Ic), and around second-phase particles (figs. 73Ic and 73III).

As can be seen from fig. 73III, obtaining homogeneous deformation via the upset forging route did not alter the observed nucleation sites. Nor did niobium additions, changes in strain rate, deformation temperature or number of passes to obtain a given total reduction (60%), alter the preferential nucleation sites observed. However, at lower strains ($\varepsilon \leq 0.49$), twin interfaces, deformation bands and grain interiors became less significant and the prior γ-grain boundaries and triple junctions almost completely dominated as viable nucleation sites (fig. 73II).

In all the steels and under all deformation conditions studied, the new grains grew anisotropically, growing more in the direction of the deformed

grain boundaries (fig. 73Ia) and ultimately linking up to form grain chains (figs. 73II & III).

4.4.4.2.2 Variation of Recrystallisation from Surface to Centre of Hot Rolled Samples

A typical surface-to-centre recrystallisation trend observed in hot rolled stainless steel samples is illustrated in figs. 74a-c for cast 1 rolled to $\varepsilon = 0.94$ (60% reduction) in one pass at 1100°C with $\dot{\varepsilon} = 3.6s^{-1}$ and held for 10s before quenching. The figure shows that recrystallisation is drastically retarded at and close to the surface-planes (74a) and accelerated in the centre-plane (74c). Also, the deformed γ-grain boundaries, which are essentially straight in the surface region become increasingly serrated towards the central region. Occasionally, an isolated local spot of a high amount of recrystallisation was observed in the surface region (74d) but just below such a spot, the amount of recrystallisation drastically dropped again (74e).

The effect of increasing isothermal holding time on the surface-to-centre recrystallisation pattern is illustrated in figs. 75(ai & aii) to 75(ci & cii). Holding for 100s resulted in an increase in the percentage of material recrystallised, f_x, at every position but f_x at the centre still exceeded that at every other plane away from the centre(figs 75ai&aii). The regions of high recrystallisation, eg fig. 74d, expanded substantially (fig. 75bi), the area below this region remaining practically unrecrystallised(fig 75bii).Holding for 300s resulted in complete recrystallisation and significant grain growth from surface to centre (figs. 75ci & cii).

A similar surface-to-centre recrystallisation gradient to the one described above was observed under all the various conditions of rolling studied and in the presence of Nb. However, the local recrystallisation high spots were not observed at low strain rates ($\leqslant 0.97\ s^{-1}$), low strains ($\leqslant 0.49$) and multi-pass rolling schedules; nor in the steels containing $\geqslant 0.20\%$Nb. In addition, the surface-to-centre recrystallisation gradient was made steeper by Niobium additions (fig. 48), a low strain rate (fig. 76), multiple pass rolling (fig. 77) and a low rolling temperature. In these cases, it can be seen that no recrystallisation occurred at the surface while the centre-planes substantially recrystallised. On the other hand, figs 78ai-aiii show that at a lower strain(0.49),the surface started to recrystallise more readily (fig. 78ai) albeit the centre was still more recrystallised (fig. 78aiii). The net result was the lowering of the

recrystallisation gradient although, as shown by figs. 78bi-biii, the surface plane (78bi) ultimately was the last to attain complete recrystallisation. When the strain was lowered still further (to $\varepsilon = 0.23$), the surface-plane remained unrecrystallised (fig. 79ai) while some recrystallisation had occurred at the centre-plane (fig. 79aii) and, at the completion of recrystallisation (figs. 79bi & bii), a few large γ-grains formed at certain regions of the surface-plane (fig. 79bii).

The variation of f_x (% of material recrystallised), from surface to centre under the various rolling conditions presented above are described graphically in figs. 80 a & b where the difference, $f_c - f_s$, between the percentage of material recrystallised at the central plane (f_c) and that recrystallised in the surface plane (f_s) is plotted as a function of isothermal holding time, t, using the data in Table 20. In all the cases ($f_c - f_s$) rises with increasing time, t, attains a maximum value and then falls sharply to zero at completion of recrystallisation. It can be seen from fig. 80a that rolling in two passes or at a lower temperature in a single pass increases the gradient as well as the maximum point of the ($f_c - f_s$) vs. lnt curve. Fig. 80b shows that a low strain rate has similar effects to a low rolling temperature or a two-pass rolling schedule. Lowering the strain lowers the peak of the curve (fig. 80a) but leaves the slope practically similar to that at a higher strain. Increasing the number of rolling passes from two to three and to four progressively lowers the maxima and the slopes of the curves (fig. 80b). It can also be observed (figs . 80a & b) that the ($f_c - f_s$) vs. lnt curve is generally shifted to the right (higher times) by: lowering the rolling temperature, or strain rate, or strain and by increasing the number of reductions for a given total strain.

The variation of recrystallisation from surface to centre of the material described in this section will henceforth be referred to as Macro-Inhomogeneity of Recrystallisation (see Discussion Section 5.4.3.2.2b).

4.4.4.2.3 The Use of Upset-forging Techniques to Isolate and Eliminate the factors responsible for Macro-Inhomogeneity of Recrystallisation

Optical microscopical examination of inhomogeneously upset-deformed samples (characterised by barrelling, eg fig. 25b), revealed surface-to-centre recrystallisation gradients similar to those observed in the rolled samples illustrated by figs. 74-80. On the other hand, homogeneously deformed

samples, obtained by upsetting under the optimised lubrication technique (section 3.3.4.2), were characterised by uniformity of recrystallisation from surface to centre. This macro-homogeneity of recrystallisation, illustrated by fig. 81, develops at short holding times, t, ($t \leq 10s$, figs. 81ai-aiii), and is maintained till the end of the recrystallisation process (figs 81bi-biii). The structural uniformity is maintained even into the grain growth regime, figs. 81ci-ciii.

It was shown in section 4.1.2.7 that non-uniform temperature distribution and material/tool interface friction were the primary causes of inhomogeneous deformation. Studies were carried out to ascertain the contribution from each of these factors to the observed inhomogeneity of recrystallisation. For ascertaining the contribution from interface friction, the sample shown in fig. 27(ai) which was obtained by deforming with equally heated top and bottom platens, but with only one face lubricated,was sectioned and examined metallographically. The results, presented in figs. 82a-d, show that the unlubricated bottom end-face was practically undeformed and completely free from any recrystallisation nuclei (fig. 82a). Only at a distance of ~2 mm (mid-way between this surface and the material centre) was there seen some evidence of deformation in the form of elongation of the prior γ-grains. The amount of deformation and, subsequently recrystallisation (fig. 82b), progressively increased (figs. 82b & c) towards the lubricated face at which recrystallisation was >90% complete (fig. 82d).

The contribution from temperature variations was assessed by examining metallographically, first the sample deformed under good lubrication but with only the top platen heated, and then the sample (fig. 27aii) deformed after cooling one end for 2s. Results from the sample deformed with only the top platen heated are shown in figs. 83 Ia&b from which it can be seen that recrystallisation was retarded at the end region in contact with the cold platens (83Ia) and then steadily increased towards the face in contact with the heated platen where it acquired its maximum value (83Ib). However, the recrystallisation gradient resulting from this interface temperature difference is less than that from differential interface friction shown in fig. 82. On the other hand, the sample deformed after cooling one end for 2s exhibited a very complex macro-inhomogeneity of recrystallisation (figs. 83IIa-d). The cooled end, like the unlubricated end in fig. 82a, was practically undeformed, and free from recrystallisation (83IIa). Evidence for deformation became pronounced only at ~2 mm from

this end face, progressively increasing towards the uncooled face. A band with its central axis lying at a distance of ~2/3rd from the cooled end face of the sample was observed with the naked eye (fig. 83II Annex, Schematic). Very close to this band, recrystallisation and grain-boundary serrations became prominent (fig 83IIb). This predominance continued within the band and recrystallisation became maximum at the band's centre, fig. 83IIc. Outside the band, towards the uncooled end region, the amount of deformation and recrystallisation started to decrease again, recrystallisation becoming practically nil at 2 mm to this end face (83IId) and deformation progressively decreasing further towards the face at which it was virtually nil. A similar deformation pattern to that shown in figs. 83IIa-d was obtained when the sample in fig. 27bi with a 5s bottom-end cooling time was studied metallographically. In this case however, there was no recrystallisation anywhere after a 10s post-deformation holding time, figs. 83III(a-f). After holding for 200s (figs. 83IVa-e) none of the end regions recrystallised (figs. 83IVa & e) although the region of the band had completely recrystallised (83IVc). The considerable variation of recrystallised grain size (compare 83IVc with 83IVb & d) must be noted although this is taken up in detail later (Section 4.4.4.4.4).

A quantitative description of these complex heterogeneities of recrystallisation (figs. 82 & 83) are listed in Table 21 and presented graphically in fig. 84 against a background of homogeneous recrystallisation of a homogeneously upset-deformed sample.

4.4.4.2.4 Variation of Migrating Boundary Area within the Thickness of Rolled or Upset-forged Samples

The variation of migrating boundary area per unit volume of austenite (S_{V_X}), within rolled or upset sample thicknesses after 10s isothermal holding following deformation under various combinations of thermo-mechanical working variables, are listed in Table 22 for cast 1 and presented graphically in fig. 85. It can be seen that in each of the rolled samples, S_{V_X} rises parabolically from a low value at the surface-plane of the sample to a maximum at the centre-plane and then falls again, progressively along a parabolic path towards the reverse surface plane where it acquires the lowest value once more. Although this effect occurs at the high temperature (1100°C) and at the lower temperature (1000°C) for a single and a multiple pass sequence, and at a high strain (0.94) and lower strains (0.49 and 0.23), the curve is lowered by any one of the following factors: a low rolling temperature, a multiple pass

rolling schedule,and a low strain. A low strain additionally lowers the slope of the curve while a low deformation temperature has the opposite effect (fig. 85). In contrast to the rolling results, the S_{V_X} values within homogeneously upset-deformed samples are practically constant (fig. 85).

4.4.4.2.5 Overall Kinetics of Static Recrystallisation of the Nb-free Steels including the effects of Thermo-Mechanical Working Variables

The percentage of material recrystallised (f_x) at various isothermal holding times (t) after hot deformation of two of the niobium-free stainless steels (casts 1 and 10) studied in this work is summarised in Table 23 and presented graphically in figs. 86-90 in Avrami types of plots, $\ln [\ln(\frac{1}{1-f_x})]$ vs lnt with the associated f_x vs lnt curves. All the Avrami plots have statistically determined regression coefficients, r, (see Appendix 6a), very close to unity ($0.95 \leq r \leq 1.0$), Table 23, indicating strong linearity of the graphs. Also, all the f_x vs lnt curves are sigmoidal in shape and reveal the existence of a definite incubation time for static recrystallisation. Values of the time-exponent, k, evaluated by applying a least-squares fit regression analysis (see Appendix 6c) to each Avrami graph, are included in Table 23.

Fig. 86 shows that lowering the rolling temperature from 1100°C to 1000°C increased the incubation time, reduced the amount of material recrystallised at any given time, and prolonged the time for completion of recrystallisation. The effects of reducing the strain rate from $3.6s^{-1}$ to $0.97s^{-1}$ at a given rolling temperature (1100°C) can be seen from fig. 87 to be similar to those of lowering the rolling temperature. Similarly, reducing the strain from 0.94 to 0.49 and to 0.23 consistently slowed down the recrystallisation kinetics by increasing the incubation time, reducing the recrystallisation rate and shifting completion of recrystallisation to a longer time, fig. 88. Considering k-values, Table 23 shows that k = 0.8 at both the 1100°C and 1000°C rolling temperatures for $\varepsilon = 0.94$ while it increased to 1.3 by lowering $\dot{\varepsilon}$ to $0.97s^{-1}$. Lowering strain (ε) to 0.49 and 0.23 increased k to 0.9 and 1.3 respectively.

The influence of multiple pass rolling sequences, illustrated in figs. 89a-c, is complex. It can be seen that increasing the number of passes for a given total reduction (60%) progressively delayed the

initiation of recrystallisation but accelerated the recrystallisation rate once the initial sluggish progress was overcome. This state of affairs resulted in the recrystallisation-curve of the material rolled in two passes crossing over that of the material rolled in a single pass and hence coming to completion earlier(figs.89a&b). Fig.89c shows that while recrystallisation did not occur between passes(or even immediately after the last pass)in the materials rolled in three or four passes(89ciii), inter-pass recrystallisation occurred in the material rolled in two passes (89cii) with the result that the recrystallised grains formed were subsequently deformed (89cii) during the last pass. The single pass schedule produced the highest amount of recrystallisation (89ci)within the first 10s after deformation. As discussed in section 5.4.3.2.6.4 these observations can be invoked to explain the differences in the recrystallisation curves(fig.89a&b). Table 23 shows that k increased with the number of passes, being 0.7,1.4,1.8 and 2.9 for one,two, three and four passes respectively.

The effect of prior austenite grain size(d_o) is listed in Table 24 from which it can be seen that decreasing d_o by lowering the reheating temperature from 1300°C to 1000°C in steps of 50°C consistently increased the amount of material recrystallised for a given time (20s).

The recrystallisation kinetics presented so far(figs.86-89) are for rolled samples which were shown earlier(section 4.4.4.2.2)to be characterised by macro-inhomogeneity of recrystallisation due to inhomogeneities of temperature and strain distributions. The recrystallisation-time data of homogeneously upset-deformed samples(for cast 1) are incorporated into Table 23 and graphically presented in figs.90a&b. A comparison of fig.90b with fig.88b shows that the upset-forged samples recrystallised more rapidly than the rolled samples. However, deformation temperature, strain rate, strain and multiple deformation had similar effects on the kinetics of recrystallisation of the upset-forged samples as they had on those of the rolled samples. In particular, a multiple deformation,relative to a single deformation,initially slowed down recrystallisation and later accelerated it albeit the single and double deformation curves did not cross over (fig. 90b)as they did in the rolling process(fig.89b). Fig.90c shows that, as in the rolling process,the recrystallised γ-grains,in the double deformation sequence,immediately after the second reduction,were deformed (fig.90cii), indicating that these grains had formed after the first forging blow. These deformed grains were not seen after a 60s holding time(fig.90ciii)indicating that they recrystallised again.The k-values for the homogeneously

deformed samples, included in Table 23, increased with increasing number of reductions, being 0.7 for a single deformation and 1.0 for a double. Also, k increased as strain was decreased, taking the values, k = 0.7, 1.1 and 1.2 for ε = 0.94, 0.49 and 0.23 respectively, other working variables remaining constant. These were similar to the trends observed for k in the rolled samples.

4.4.4.2.6 Overall Kinetics of Static Recrystallisation of the Nb-bearing Steels including the Effects of Thermo-Mechanical Working Variables

The recrystallisation-time data of the 0.042%, 0.20% and 0.48% Nb stainless steels are summarised in Tables 25(a-c) and presented graphically in figs. 91-93. The Avrami and f_x vs lnt curves in figs. 91-93 are similar in shape to those obtained for the Nb-free steels (figs. 86-90), the effect of the Nb addition being mainly to retard recrystallisation, generally by increasing the incubation time and shifting completion of recrystallisation to longer times.

The addition of 0.042%Nb was not effective in retarding recrystallisation when rolling was carried out at 1100°C with $\dot{\varepsilon}$ = $3.6s^{-1}$ to a high strain (0.94) or even to a moderate strain of 0.49 (fig. 91I). However, as can also be seen from fig. 91I this amount of Nb became significantly effective in retarding recrystallisation at a lower rolling temperature (1000°C), a low strain rate ($0.97s^{-1}$), a low strain (0.23), or any combination of these three factors. Values of k, summarised in Table 25a, increased, as in the Nb-free steels, with decreasing strain, being 0.7, 0.9 and 1.2 for ε = 0.94, 0.49 and 0.23 respectively. Also, decreasing $\dot{\varepsilon}$ from $3.6s^{-1}$ to $0.97s^{-1}$ for a strain of 0.23, raised k from 1.2 to 1.6. Also, k increased when rolling temperature was decreased. Fig. 91II shows that, as in the Nb-free steels, multiple-pass rolling gave rise to an initial slow rate of recrystallisation followed by a fast rate, resulting in the cross-over of the curves for single and multiple passes. The figure (91II) also shows that homogeneously upset-deformed samples showed faster recrystallisation than their rolled counterparts. In addition, a comparison of fig. 91II with fig. 91I reveals that the retarding effect of a low rolling temperature on recrystallisation is more at a low strain (fig. 91I) than at a high strain (fig. 91II) in this steel. It can be seen from Table 25a that, as in the Nb-free steels, k increased with an increasing number of deformations. Also, as in previous results, values of k were lower for upset-forged than rolled samples, being 0.5 and 0.7 for upset-forged and

rolled samples respectively at a deformation temperature of 1100°C and $\dot{\varepsilon} = 3.6s^{-1}$ in this case.

The addition of 0.20%Nb resulted in a significant retardation of recrystallisation even at a high rolling temperature of 1100°C. However, as in the 0% and 0.042%Nb steels, decreasing strain slowed down recrystallisation (fig. 92I) while the homogeneous deformation (upsetting) process accelerated it (fig. 92I). Multiple deformation (fig. 92II), whether by rolling or by upsetting, had a similar effect on the recrystallisation of this steel as it had on that of the 0% or 0.042% Nb steels. Lowering the rolling temperature retarded the recrystallisation rate at high(0.94)and low (0.23) strains (fig. 92III). It can be seen from fig. 92III that the retardation effect of a low deformation temperature in this steel was limited to the early stages of the recrystallisation, the recrystallisation rate later becoming rapid. As in the 0% and 0.042% Nb steels, k-values (Table 25b) increased with decreasing strain, increasing number of deformations, or decreasing deformation temperature. Also k-values for upset-forged samples were lower than for rolled ones under similar combinations of deformation variables. For example, double-pass rolling increased k from 1.0 to 2.4 while a double-blow upsetting increased it from 0.8 to 1.4. It must be pointed out that changes in working variables produced more pronounced effects on the recrystallisation kinetics of this (0.20%Nb) steel than in the 0% or 0.042% Nb steels.

The severest retardation of recrystallisation was observed in the 0.48%Nb steel. In fact, even for a high strain of 0.94 (60% reduction) with $\dot{\varepsilon} = 3.6s^{-1}$ at 1100°C, complete recrystallisation was not achieved after holding isothermally for 1000s (fig. 93Ia). This is substantial when compared with recrystallisation completion times of 200s and 400s for the 0% and 0.20% Nb steels respectively under identical processing conditions. Fig. 93II shows that decreasing the rolling reduction (strain) progressively decreased the rate of recrystallisation. From Table25c,it can be seen that k-values increased as strain was reduced. This was also observed in the 0-0.20%Nb steels. The recrystallisation kinetics after deformation by upsetting, presented in fig. 93III, generally exhibit similar trends to those for rolled samples (fig. 93II) in that the rate of recrystallisation progressively decreased as strain decreased. Also, k-values increased as strain decreased (Table 25c). A comparison of fig. 93III with fig. 93II shows that the upset-forged samples recrystallised faster than their rolled equivalents. It can also be seen from fig. 93III that double deformation,

as in previous results, increased the incubation time, but later gave rise to a fast recrystallisation rate.

4.4.4.2.7 Variation of the Time for 50% Recrystallisation with Deformation Variables

The time for a given fraction (f_x) to recrystallise, denoted by t_{f_x}, can be used as a measure for assessing the influence of working variables on recrystallisation kinetics. Generally, t_{50}, the time for 50% recrystallisation, is taken. Table 26 shows values of t_{50} obtained for the base and Nb steels under various combinations of working variables. It can be seen that t_{50} is increased by any of the following factors: a reduction in strain, an increase in the number of sequential deformation operations for a given total strain, a reduction in strain rate, a reduction in deformation temperature, and any combination of these factors. As illustrated in fig. 94 for the 0%, 0.20% and 0.48% Nb steels, $\ln t_{50}$ is linearly related to $\ln\varepsilon$. This indicates that t_{50} is related to strain (ε) by a power law of the form $t_{50} \propto \varepsilon^n$, where n is a constant. Using a least squares fit regression analysis (Appendix 6c), n was found, within 95% confidence limits, to be -1.43 ± 0.21 for both the base and the Nb steels considered, in the strain range 0.23 - 0.94.

4.4.4.2.8 Recrystallisation Kinetics under conditions of Macro-Inhomogeneity of Recrystallisation

The progress of recrystallisation (f_x) with increasing isothermal time (t), was monitored separately at the surface and central planes of rolled samples (shown to be characterised by macro-inhomogeneity of recrystallisation in section 4.4.4.2.2) and then f_x vs lnt as well as Avrami plots were drawn for each plane in the same diagram, shading the area enclosed by each set of curves. The procedure is illustrated in figs.95&96 for a 0% Nb steel (cast 10) and the 0.48% Nb steel respectively, rolled under various combinations of working variables. The data presented graphically in figs.95 & 96 are listed in Table 27 where, as in the graphs, f_s and f_c represent the mean fraction recrystallised at the surface and central planes respectively, at a given time.

In all cases, recrystallisation occurred more rapidly at the centre than at the surface. With the exception of the low strain rate results ($0.97s^{-1}$, figs. 95bi and bii) the Avrami plots for the surface and the centre tend to converge as holding time is increased; so do the f_s vs lnt and f_c vs lnt curves. The tendency to converge is greater at high strains(figs.95a&96a)

than at lower strains (figs. 95d and 96d) in both the base and the Nb steels. A double reduction sequence also diminishes the tendency for the curves to converge (fig. 95c).

Values of k, determined statistically, by applying least squares fit regression techniques (Appendix 6c) to the data points of the Avrami plots, are incorporated into Table 27. It can be seen from the Table that under all rolling conditions investigated and for both the 0% and 0.48% Nb steels, the value of k for the surface plane (k_s) is always greater than k_c, where k_c is the k-value for the central-plane.

4.4.4.3 Static Recrystallisation of the C-Mn base and C-Mn-0.045%Nb Steels after Hot Rolling or Hot Upset-Forging

4.4.4.3.1 Nucleation and Growth of new, strain-free, γ-grains

In both the base steel (0% Nb) and the 0.045%Nb steel, casts 11 and 13, respectively, nucleation of new austenite grains was observed predominantly at serrated grain boundaries and triple junctions of the deformed γ-grains. These are illustrated in fig. 97 for the base steel rolled at 1100°C in one pass to $\varepsilon = 0.23$ with $\dot{\varepsilon} = 3.6s^{-1}$. Nucleation at deformation bands was not observed. In a similar manner to the stainless steels, new γ-grains grow more along the prior γ-grain boundaries than into the body of the grains, resulting in a linkage of recrystallised γ-grains into grain chains. These nucleation and growth modes are not altered by varying the hot deformation variables or niobium content in the steel.

4.4.4.3.2 Macro-Inhomogeneity of Recrystallisation of Rolled Samples and the Elimination of this using Upset-forging Techniques

Under all rolling conditions investigated, a steep surface-to-centre recrystallisation gradient was observed in both the base steel and the Nb steel rolled and quenched after $\leq$ 10s. This is illustrated in fig. 98 and fig. 99(ai & aii) for the base and Nb steels respectively. The gradient was made steeper by a low rolling temperature, a low strain rate, a multiple pass rolling sequence, a Nb addition, or any combination of these factors. With increasing isothermal holding, both the centre and the surface ultimately attained complete recrystallisation, the surface always being the last to recrystallise fully and, into larger γ-grains. A special feature associated with the Nb-steel rolled at a low strain rate ($0.97s^{-1}$) is that although the mean γ-grain size at the surface (figs. 99bi and bii) is larger than that at the centre (fig. 99biii) at completion of recrystallisation, the

γ-grains in the surface regions vary considerably from position to position, being fine at some positions (fig. 99bi) and coarse at other positions (fig. 99bii).

A typical distribution of recrystallisation from surface to centre which occurred in both the base steel and the Nb steel after homogeneous deformation by upset-forging followed by quenching within 10s, is illustrated for the base steel in fig. 100. It can be seen that there is virtually no difference in the amount of material recrystallised at the surface (fig. 100a) and the centre (fig. 100b). This macro-uniformity of recrystallisation was maintained with increasing isothermal time till complete recrystallisation occurred at every position within the material.

4.4.4.3.3 Influence of Niobium Additions and Thermo-Mechanical Working Variables on Static Recrystallisation of the C-Mn steel

In general, the C-Mn steels, with or without a Nb addition, recrystallised much faster than the stainless steels even in the absence of any Nb addition. However, the addition of 0.045% Nb significantly retarded recrystallisation in the C-Mn steels even at a high deformation temperature of 1100°C and a moderately high strain of 0.49 with $\dot{\bar{\varepsilon}} = 3.6s^{-1}$. This level of Nb was not effective in retarding recrystallisation in the stainless steels (section 4.4.4.2.6) deformed under identical working conditions.

As in the stainless steels, recrystallisation was retarded by lowering the deformation temperature, lowering the strain rate, lowering strain, or by combining any of these three factors. Multiple deformation had a more complex effect than in the stainless steels as a result of the $\gamma \rightarrow \alpha$ transformation which occurred between passes resulting from large temperature drops in the relatively small test samples.

4.4.4.4 Statically Recrystallised γ-Grain Size of the Stainless Steels

4.4.4.4.1 Variation of Aspect Ratios of Recrystallised γ-Grains with Isothermal holding Time

Typical variations of the mean aspect ratio, $\bar{A}_r$, of recrystallised γ-grains with isothermal holding time, t, are summarised in Table 28 for casts 1&10 deformed under various conditions of rolling. The data are presented graphically in figs. 101a-c. Fig. 101a shows that, 10s after rolling in a single pass to either a strain of 0.94,or 0.49,or 0.23,the recrystallised γ-grains acquired $\bar{A}_r$ of ~1.5 which then decreased exponentially to a const-

ant value of ~1.0 as time(t) increased. Although a higher strain tended to steepen the exponential curve, all the data points for ε = 0.23 - 0.94 fall within a narrow band as shaded (101a). Lowering the strain rate from $3.6s^{-1}$ to $0.97s^{-1}$ at the same strain (0.94) lowered the slope of the curve only marginally (fig. 101b).

Fig. 101c shows the effect of multi-pass rolling on $\bar{A}_r$. Despite the scatter in the individual points, it can be seen that $\bar{A}_r$ and hence the slope of the $\bar{A}_r$ vs t curve (prior to $\bar{A}_r$ attaining the value of unity) is progressively raised by deforming in two and three passes. Increasing the number of passes to four resulted in $\bar{A}_r$ values lower than those of a three-pass schedule and an $\bar{A}_r$ vs t curve (fig. 101c) with a shallower slope than those of the two- and three-pass curves.

4.4.4.4.2 Inhomogeneities of the Recrystallised γ-Grain Size

Recrystallised γ-grain size heterogeneities observed include those caused by compositional factors, characterised by the existence of ultra-fine recrystallised γ-grains around bands of second phase particles and of coarse grains farther away from such bands. This type of grain size heterogeneity was restricted to the steels containing $\geq$ 0.20%Nb. Two other γ-grain size heterogeneities observed and which occurred in all the steels under all rolling conditions are described below. Examination of any optical micrograph (eg fig. 74c or 78biii) shows that the individual recrystallised γ-grains at any given position within the material vary in size. This sort of heterogeneity will be termed micro-inhomogeneity of d_{rex}. Figs. 75ai and aii show that the mean recrystallised γ-grain size (d_s) at the surface-plane (fig. 75ai) is larger than the mean γ-grain size (d_c) at the central plane (fig. 75aii). However, d_c is larger than the mean re-crystallised γ-grain size, d_i, at the intermediate plane between the surface- and the centre-planes, (compare fig. 74b with fig. 74c). This variation of mean d_{rex} values from surface-plane to centre-plane will be termed macro-inhomogeneity of d_{rex}. A quantitative description of the macro-inhomogeneity of the d_{rex} situation is illustrated in Table 29 for cast 1 and presented graphically in fig. 102a, from which it can be seen that d_{rex} is maximum in the surface-plane, minimum in the intermediate plane between the surface and the centre (ie mid-plane), and then rises to a value slightly higher than the mid-plane value at the centre-plane. It can also be seen from fig. 102a that lowering the strain from 0.94 to 0.23 lowered the macro-inhomogeneity of d_{rex}. So does increasing the isothermal holding time (fig. 102a). For each sample, the mean d_{rex} values at various

planes from surface to centre were evaluated and the coefficient of variation, $C_{V_{ma}}$, of these mean values computed (using the statistical method outlined in Appendix 6e) to quantify the macro-inhomogeneity of d_{rex} in that sample. The results are incorporated into Table 30 where the recrystallised γ-grain size data for the stainless steels, with and without Nb additions, which were deformed by rolling, are listed. Coefficients of variations of individual γ-grains from one another at the surface, intermediate between the surface and the centre, and the centre-plane, denoted by C_{V_s}, C_{V_i} and C_{V_c} respectively, were also computed to quantify micro-inhomogeneities and these are also incorporated into Table 30.

Table 30 reveals no systematic variation of C_{V_s}, C_{V_i} or C_{V_c} with working variables. On the other hand, $C_{V_{ma}}$ exhibits some definite dependences on the processing variables. It can be seen from Table 30 that reducing the strain from 0.94 down to 0.23 consistently lowered $C_{V_{ma}}$ within a post-deformation isothermal holding time of 10 s to 30 s. However, as holding time was increased, while $C_{V_{ma}}$ for the material given the highest strain decreased, the $C_{V_{ma}}$ values for the materials given the lower levels of strain (0.49 and 0.23) increased. It can further be seen that $C_{V_{ma}}$ is also raised by a lower (1000°C) rolling temperature as well as by a low ($0.97s^{-1}$) strain rate. The influence of multiple deformation is also illustrated in Table 30, for cast 10, from which it can be seen that within the isothermal holding time, $t \leq 40s$, increasing the number of passes, up to three, consistently decreased $C_{V_{ma}}$. Increasing t to 60s and then progressively from this value to 1000s resulted in a consistent drop in $C_{V_{ma}}$ value in the case of the single pass, but consistent increases in the cases of the two and three-pass schedules. Reliable values of $C_{V_{ma}}$ could not be obtained for the four-pass schedule for $t < 200s$ due to the associated sluggish recrystallisation kinetics. A comparison of the $C_{V_{ma}}$ values of the Nb-steels with those of the Nb-free steels (Table 30) deformed under identical conditions shows that $C_{V_{ma}}$ is raised by Nb additions.

4.4.4.4.3 Elimination of Macro-Inhomogeneity of Recrystallised γ-Grain Size through Upset-forging Techniques

The various d_{rex} heterogeneities described in the last section for rolled samples were also observed in upset-forged samples subjected to inhomogeneous deformation (ie cylinders transformed to barrel shapes after forging). However, as can be seen from the micrographs in figs. 81a-c, homogeneous deformation via the optimally lubricated upset-forging technique resulted

in uniformity of mean d_{rex} from surface to centre of the material (ie $d_s \cong d_i \cong d_c$ and $C_{V_{ma}} \cong 0$). This uniform d_{rex} distribution from the surface-plane to the centre-plane is illustrated in Table 31a and presented graphically in fig. 102b for casts 1 and 5 upset-forged to $\varepsilon = 0.94$ in a single blow deformation sequence using the optimised lubrication technique. It can be seen from the $C_{V_{ma}}$ values included in Table 31a that this macro-uniformity of d_{rex} is preserved, and if anything tends to get better, as isothermal holding time is increased, even into the grain growth regime. This is further substantiated by the series of micrographs in figs 81ai-aiii to 81ci-ciii. Also, this macro-homogeneity of d_{rex} was not altered by changes in the thermo-mechanical working variables provided that deformation was carried out using the optimised lubrication technique. Consequently, only the mean d_{rex} values of the upset-forged samples are listed, in Tables 31b & c for use in quantitative correlations in subsequent sections.

Examination of any of the micrographs in figs 81a-c reveals that although macro-inhomogeneity of d_{rex} was eliminated by obtaining homogeneous deformation, micro-inhomogeneity was not.

4.4.4.4.4 Comparative Importance of Interface Friction and Non-Uniform Temperature Distribution in the Evolution of Macro-Inhomogeneity of Recrystallised γ-Grain Size

No recrystallised γ-grains formed in the unlubricated surface region of the sample upset-forged with only one end face lubricated (fig. 82a). However, the recrystallised γ-grains at the lubricated end region have a finer mean size (19 μm), fig 82d, than the recrystallised γ-grains formed at the centre-plane (22 μm), fig. 82c.

The effect of inducing a steep temperature gradient within the material by cooling only one end-face (section 4.1.2.7) was similar to that of the one-sided lubrication described above in that the cooled end region (fig. 83IIa) like the unlubricated end (fig. 82a), contained no recrystallised γ-grains. A further complication associated with the material deformed after cooling one end in water was the absence of recrystallised γ-grains even in the end region which was not cooled in water (fig. 83IId). After holding for 200 s, it can however be seen from fig. 83IV that, at a position two-thirds of the sample thickness from the water cooled end face, relatively fine recrystallised γ-grains were formed (83IVc). From this position the recrystallised γ-grain size progressively increased towards the two end faces, those towards the water cooled end (83IVb) being coarser than those

towards the uncooled end (83IVd). It can then be concluded that a non-uniform temperature distribution is equally important in the evolution of a macro-inhomogeneous recrystallised γ-grain size.

4.4.4.4.5 Macro-hardness Variation in the through-thickness of Homogeneously and Various Inhomogeneously Upset-Deformed Samples

Results of macro-hardness traverses made across the through-thickness of samples upset-forged under various conditions of interface friction and internal temperature distributions are summarised in Table 32 and presented graphically in fig. 103. The H_v values across the sample just prior to deformation are also plotted in fig. 103. It can be seen that macro-hardness within the sample through-thickness prior to deformation was practically uniform (with a mean value of ~121) and also remained essentially uniform after uniform deformation but with a higher value (mean H_v = 171) although there was a slight tendency for H_v to be higher in the surface-plane in the former case but lower there in the latter, fig. 103. The figure shows that the unlubricated end-region of the sample deformed with only the top end-face lubricated acquired a hardness value of 132 which rose steadily to a maximum value of 165 at the centre-plane and then gradually dropped to ~152 at the lubricated end region.

The sample deformed with only one platen heated acquired a hardness value of 175 at the end-region in contact with the hot platen and a hardness value of 183 at the end in contact with the cold platen. A hardness trough (H_v = 172) occurred at the centre-plane. The mean hardness value within the through-thickness of this sample was 177 which is higher than that of the homogeneously deformed sample. It can be seen (fig. 103) that inducing a temperature gradient into the material prior to deformation by cooling one end resulted in a complex heterogeneity of hardness within the sample. The low hardness value (133) at the cooled end region steadily rose to a peak value of 153 and thereafter started to drop again, reaching a minimum value of 135 at a position two-thirds of the specimen thickness from the cooled end. As it can be seen, the hardness steadily rose once more from this value, reaching a maximum value of 157 at ~1 mm from the uncooled face and then dropped again as this surface was reached.

4.4.4.4.6 Dependence of Recrystallised γ-Grain Size (d_{rex}) on Nb-Additions and Thermo-Mechanical Working Variables

4.4.4.4.6.1 Dependence of d_{rex} on Niobium-Additions

From the recrystallised γ-grain size data in Tables 30 and 31, it can be

seen that Nb, even as low as 0.042%, refined the recrystallised γ-grain size, d_{rex}. This effect is presented graphically in fig.104 from which it can be seen that although d_{rex} steadily decreases as the amount of Nb increases, the decrease in d_{rex} becomes slight at above ~0.2%Nb addition and ultimately tends to disappear. Fig. 104 also shows that the curve for the casts pre-rolled into square sections from their ingots lies higher than the curve for the casts pre-rolled to flats from their ingots (see also section 4.4.2.2).

4.4.4.4.6.2 Dependence of d_{rex} on Prior γ-grain size (or on Grain Boundary Interfacial Area per unit Volume of Prior Austenite)

A typical variation of d_{rex} with prior γ-grain size, d_o, is listed in Table 31c for cast 9. It must be noted that d_o was varied by varying the reheating temperature, from 1000-1300°C. Corresponding values of the prior γ-grain boundary interfacial area per unit volume of prior austenite, denoted by S_{V_o}, are also included in Table 31c. The data in Table 31c are presented graphically in figs. 105a & b as curves of d_{rex} vs d_o (105a) and d_{rex} vs S_{V_o}, (105b).

Fig. 105a shows that increasing d_o increases d_{rex} in a curvilinear fashion. This suggests a power relationship of the form $d_{rex} \propto d_o^n$, where n is a constant. Regression analysis of the data points, using the techniques outlined in Appendix 6c, showed that the ln d_{rex} vs ln d_o graph is a straight line (coefficient of correlation, r = 0.9995) with a slope, n = +0.556, see fig. 105c.

The graph of d_{rex} vs S_{V_o} (fig. 105b) shows that d_{rex} decreases as S_{V_o} increases, again along a curvilinear path and a plot of ln d_{rex} vs ln S_{V_o} (105d) is a straight line with r = -0.9997 and slope, n = -0.574.

4.4.4.4.6.3 Dependence on Strain

From the recrystallised γ-grain size data in Tables 30 and 31, it can be seen that increasing strain (ε) at the same temperature and strain rate decreases d_{rex} in both the base and Nb steels. This is illustrated graphically in fig. 106 for rolled (106a) and upset-forged (106b) samples. Figs. 106a & b show that d_{rex} refinement by increasing ε is large at first and then becomes progressively smaller as ε is further increased.

Figs. 106c & d show that ln d_{rex} is linearly related to ln ε in both the rolling (106c) and the upsetting (106d) processes, confirmed by the computed

correlation coefficients of all the ln d_{rex} vs ln ε curves lying between 0.962 and 0.999. This indicates that $d_{rex} \propto \varepsilon^n$, where n, a constant, was found (Appendix 6c) to take the values -0.50 to -0.56 in the rolling process and -0.56 to -0.60 in the upsetting process. At the 95% confidence limit, a best average value of n found to cover all the stainless steels, deformed either by rolling or by upset-forging, was -0.52 ± 0.03.

4.4.4.4.6.4 Dependences on Deformation Temperature and Strain Rate

The variation of d_{rex} with deformation temperature (T) for rolled and upset-forged samples are illustrated in Table 33. Table 33 also incorporates a summary of d_{rex} variation with deformation temperature(T)and strain rate ($\dot{\varepsilon}$) in the plane-strain deformation process. It can be seen that, for the base and the Nb steels, d_{rex} was decreased by a lower deformation temperature and/or a lower $\dot{\varepsilon}$. This is further substantiated by the micrographs for a Nb-free steel (107ai-aiii) and a 0.45%Nb steel (107bi-biii) deformed in plane strain.

No unique relationship could be found between d_{rex} and $\dot{\varepsilon}$. On the other hand, graphs of d_{rex} vs $(1/T \times 10^4)°K^{-1}$ (fig. 108) for the rolling and upsetting results (fig. 108a) and for the plane strain deformation results (fig. 108b) were straight lines with negative slopes.

4.4.4.4.6.5 Dependence on Temperature Compensated Strain Rate

The effects of deformation temperature (T) and $\dot{\varepsilon}$ described in the last section were combined by analysing the dependence of d_{rex} on the temperature compensated strain rate, Z. The results are incorporated into Table 33 for the rolled, upset-forged, and the plane strain deformed samples. Graphical presentations of these results in the form of ln d_{rex} vs ln Z graphs are shown in fig. 109a for both rolled and upset-forged samples and in fig. 109b for the samples tested in plane strain on the servo-hydraulic machine. In all the cases (figs. 109a & b), the best least square fit lines, found by computer techniques, employing the principles in Appendix 6, have correlation coefficients, r, in the range $0.99 \leq r \leq 1.0$, all significant at the 5% level. This strong linear relationship indicates that $d_{rex} \propto Z^n$ where n, the mean slope of the various straight lines in figs. 109a & b, was found to be -0.134 ± 0.001 at the 95% confidence limit.

4.4.4.4.6.6 Dependence on Number of Reductions in a Multiple Deformation Working Sequence

The variations of d_{rex} with number of reductions for a given total strain,

can be seen from the d_{rex} data presented earlier in Tables 30 and 31b for rolled and upset-forged samples respectively. The data are presented diagramatically, using bar diagrams, in fig. 110a for upset-forged, and in fig. 110b for rolled, samples. It can be seen that in each of the cases (figs. 110ai, aii & b), after holding isothermally for 10s, d_{rex} for a double reduction was larger than the d_{rex} for a single reduction. Increasing the number of reductions to three and above, progressively decreased d_{rex} (figs. 110aii & b) in the same 10s holding time. Fig. 110b shows that the above pattern of recrystallised γ-grain size variation with number of reductions was maintained after holding for 100s, that is, in the primary grain growth regime (see section 4.4.4.6).

However, after 1000s holding, the recrystallised γ-grain size developed in the material deformed in a single pass exceeded the γ-grain size for the double pass reduction, fig. 110b. It can in fact be seen that the recrystallised γ-grain size progressively decreased from a peak value in the single pass deformation to its lowest value in the four pass deformation-schedule.

4.4.4.5 Statically Recrystallised γ-Grain Size of the C-Mn and C-Mn-Nb Steels

4.4.4.5.1 Inhomogeneities of the Recrystallised γ-Grain Size

As in the stainless steels, variation of individual recrystallised γ-grain sizes at any location within the material was observed in both rolled and upset-forged samples. Also as in the stainless steels, there was variation of mean d_{rex} from surface- to centre-plane, that is, macro-inhomogeneity of d_{rex}. This is illustrated by the micrographs in figs. 99bi-biii for the Nb steel from which it can be seen that the mean d_{rex} in the surface regions (99bi & bii) is larger than that in the centre-plane (99biii). This surface-to-centre inhomogeneity of d_{rex} is summarised in Table 34a for the base and the Nb steels.

The variation of individual d_{rex} values did not occur in any systematic fashion as deformation variables were varied. On the other hand, the macro-inhomogeneity of d_{rex}, quantified by the coefficient of variation of d_{rex} from surface to centre [$C_{V_{ma}}$] can be seen from table 34a to be reduced by reducing strain but increased when strain rate was lowered. The strain rate effect was more pronounced in the Nb-steel than in the base steel. It was also observed that rolling in two passes lowered the surface-to-centre heterogeneity of d_{rex}. In general the $C_{V_{ma}}$ values for the C-Mn and C-Mn-Nb

steels were lower than those associated with the stainless steels, a best average value for the C-Mn and C-Mn-Nb steels being ~0.14 as against a mean value of ~0.25 for the stainless steels.

Similar to the results of upset-forging of the stainless steels, upset-forging of the C-Mn and C-Mn-Nb steels using the optimised lubrication technique (section 3.3.4.2) eliminated the macro-inhomogeneity of d_{rex} in both the base and Nb steels, that is, mean values of d_{rex} at various positions from surface to centre of the material did not vary significantly, fig. 100. The d_{rex} data listed in Table 34b for the C-Mn base and Nb steels, homogeneously deformed by upsetting, clearly illustrate this surface-to-centre d_{rex} uniformity.

4.4.4.5.2 Dependence of Recrystallised γ-Grain Size on Nb-Additions and Thermo-Mechanical Working Variables

The d_{rex} data of the C-Mn base and Nb steels, summarised in Tables 34 a & b, reveal that, as in the stainless steels, Nb additions resulted in d_{rex} refinement. Even Nb as low as 0.045% significantly refined d_{rex} despite the high deformation temperature of 1100°C used. Fig. 111 shows a graphical description of the dependence of d_{rex} on Nb-additions. It can also be seen from the figure (fig. 111) that under identical processing conditions, the d_{rex} values developed in the materials pre-rolled from their ingots into flats (Curve C) are generally smaller than the d_{rex} values developed in those pre-rolled from their ingots into square sections (Curve B). This is consistent with the results of the stainless steels (fig. 104).

From the d_{rex} data (Tables 34 a&b), a description of d_{rex} dependence on strain (ε) is presented in fig. 112 for a holding time of 10s. It can be seen that d_{rex} decreases as ε is increased (fig. 112a), the decrease in d_{rex} tending to diminish as ε is increased. Regression analysis showed that $\ln d_{rex}$ is linearly related to $\ln\varepsilon$ (fig. 112b). The slopes of the lines were -0.58 for the base steel and -0.63 for the Nb-steel, the mean slope to cover both steels being -0.60. Hence d_{rex} is related to ε by a power law of the form $d_{rex} \propto \varepsilon^n$ where $n = -0.60$.

The results in Tables 34 a & b show that in both the base and Nb steels, d_{rex} is decreased by a low strain rate and a multiple deformation sequence.

4.4.4.6 Primary Grain Growth of Recrystallised γ-Grains in the Austenitic Stainless Steels

Typical primary grain growth of recrystallised γ-grains observed in the various stainless steels tested are illustrated by the micrographs in fig. 113 for 0% Nb (113ai & aii), 0.042%Nb (113bi & bii) and 0.20%Nb (113ci & cii) steels upset-forged in one blow to $\varepsilon = 0.94$ at 1100°C with $\dot{\varepsilon} = 3.6s^{-1}$, and held isothermally at the deformation temperature (1100°C). It can be seen that the mean recrystallised γ-grain size (to be denoted by d_g in the primary grain growth regime), developed in the Nb-free steel after 100s (fig. 113ai) increased significantly after 1800s (113aii). Similarly, the d_g values developed after 100s (113bi) in the 0.042%Nb steel increased significantly after 1800s holding time (113bii). On the other hand, there is virtually no increase in the d_g values developed in the 0.20%Nb steel in 100s (113ci) after holding for 1800s (113cii). These results show that Nb additions retarded primary grain growth albeit the 0.042%Nb addition was only partly effective in this respect at the 1100°C holding temperature. It must be noted that although fig. 113 depicts primary grain growth after complete recrystallisation has occurred, it can be seen, by comparing figs. 78ai-aiii with figs 78bi-biii, that primary grain growth also occurred prior to the completion of recrystallisation.

The kinetic relationships which describe the primary grain growth processes, as observed in the various stainless steels studied, are illustrated graphically in figs. 114 and 115 for rolled samples and in fig. 116 for upset-forged samples. Fig. 114a shows that, in the rolling process, the growth process is retarded by the presence of Nb as well as by increasing the rolling reduction. Regression analysis revealed that $\ln d_g$ is linearly related to $\ln t$ (fig. 114b), the slope of the lines being 0.51 for the 0% Nb steel and ~0.21 ± 0.04 for the 0.48%Nb steel at the 95% confidence limit for the strain range 0.23 - 0.94. These suggest that in the primary grain growth regime, taken here as generally being the isothermal holding time, $t \geq 40s$, d_g is related to t by a power law of the form, $d_g \propto t^n$ where n = 0.5 for the Nb-free steel and n = 0.2 for the Nb-bearing steel. The influence of multipass rolling is shown in fig. 115a for cast 10. There is a strong linear correlation between $\ln d_g$ and $\ln t$ (fig. 115b), computed slopes of the best fit lines being 0.5, 0.3 and 0.5 for one, two and three-pass reductions respectively.

As shown in figs. 116a & b, the kinetics of primary grain growth in the upset-forged samples are essentially similar to those in their rolled

counterparts (compare fig. 116a with fig. 114a).

4.4.4.7 Primary Grain Growth of Recrystallised γ-Grains in the C-Mn and C-Mn-Nb Steels

The micrographs in fig. 117 illustrate a typical primary grain growth phenomena observed in the C-Mn base steel (117a) and the Nb steel (fig. 117b). Both steels were rolled at the same temperature (1100°C) to the same strain (0.94) and with the same strain rate ($3.6s^{-1}$) and subsequently held at the same temperature (1100°C). Fig. 117 shows that in the base steel (117a), the mean γ-grain size (d_g) developed after 300s (fig. 117ai) increased significantly after 1000s (fig. 117aii) while in the 0.045%Nb steel (fig. 117b), the mean γ-grain size (d_g) developed after holding for 300s (117bi) did not increase by any significant amount after 1000s (117bii). It is interesting to note that this level of Nb-addition was not as highly effective in inhibiting primary grain growth in the stainless steels (fig. 113bi & bii).

Fig. 118a shows that d_g increases with the isothermal holding time, t, in a curvilinear fashion. Figure 118b shows that a plot of $\ln d_g$ vs. $\ln t$ in the grain growth regime, t = 100-1000s, is linear, indicating that d_g is related to t by a relationship of the form $d_g \propto t^n$ where n is a constant. Regression analysis showed that n had a mean value of ~0.33 for the base steel, and ~0.13 for the 0.045%Nb steel, under the various combination of working variables investigated.

As illustrated by figs. 119a & b, the d_g values at and near the surface region (119a) were always larger than the d_g values developed in the central planes (119b) for all rolled samples. This effect was accentuated by a low strain and/or a low strain rate, the d_g values at the surface-plane also varying from one position in the surface to another (figs. 99bi and bii) in the C-Mn-Nb steel. No variation in mean γ-grain sized (d_g) from one plane to another was observed in homogeneously upset-deformed samples.

4.4.5 Some Miscellaneous Observations during the Recrystallisation and Recrystallised γ-Grain Size Studies of the Austenitic Stainless Steels

4.4.5.1 Wavy Bands on Rolled Samples

As illustrated by fig. 120a for a Nb-free steel (Cast 1), rolled samples were characterised by dark wavy bands which were aligned parallel to the rolling direction. Examination of such samples on the Scanning

Electron Microscope (SEM) showed that the banded areas were pitted, fig. 120b. A micro-scan analysis on the SEM showed that the bands were richer in Cr and Ni than the unbanded matrix, Table 35a. Generally the bands occurred more in the Nb steels than in the base steels.

Fig. 120c shows a sample of the same Nb-free steel (Cast 1) upset-forged to the same strain as the rolled sample in fig. 120a. It can be seen that the axisymmetrical upset-forging operation broke up the bands and distributed them into the surrounding matrix. In fact only in the Nb-steels are the outline of the squashed bands well defined (fig. 120d see also fig. 113ci) when upset-deformation was carried out to this high strain (0.94). A comparison of fig. 113ci with fig. 113cii shows that the area covered by the squashed bands tended to thin down as isothermal holding time after deformation was increased.

In order to establish the primary origin of these dark bands, optical metallographic studies of the as-cast Nb-free and Nb-bearing steels were carried out. The structures observed are illustrated in figs. 120e and 120f for the Nb-free and 0.20%Nb steels respectively. The results of micro-scan analyses of these structures, summarised in Table 35b, reveal that the dark networks are consistently richer in Cr and Ni contents than the white islands, thus showing that these dark networks are the interdendritic regions, while the white islands are the primary dendrites, of the cast material. A comparison of the results of the micro-scan analyses of the rolled samples (Table 35a) with those for the as-cast material (Table 35b) clearly shows that the dark wavy bands observed in the rolled samples were actually the interdendritic regions of the as-cast sample, drawn out by the preliminary ingot-rolling operation.

4.4.5.2 Oscillatory Variation of Micro-hardness within the Sample just Prior to Deformation

Typical results of micro-hardness traverses across the thickness of samples quenched in iced-brine after reheating at 1100°C for deformation, are listed in Table 36 for a 0% Nb steel (Cast 1). The data is presented graphically in fig. 121 from which it can be seen that micro-hardness, H_V, in the through-thickness direction of the sample, oscillates about a mean value of ~149DPN with a more or less constant amplitude. As discussed in Section 5.4.1.2, this cyclic variation can be related to the presence of the dark-etching, alloy-rich, interdendritic regions.

4.4.5.3 Occurrence of Large Unrecrystallised γ-Grains

Fig. 122a illustrates typical unrecrystallised austenite grain structures observed in the stainless steels containing ≧0.20%Nb after rolling to a low strain ($\varepsilon \cong 0.23$). It can be seen that the morphology and size of the deformed γ-grains in the surface region (fig. 122ai) are practically uniform. On the other hand, the centre-plane (fig. 122aiii) and the plane between the surface and the centre, fig. 122aii, are characterised by alternate layers of large and small unrecrystallised γ-grains.

The above effects were not observed in the Nb-free and 0.042%Nb steels deformed under identical conditions. Instead, as illustrated in Figs. 122bi-biii, coarse unrecrystallised γ-grains were observed in the surface-planes (fig. 122bi) of the Nb-free steels rolled to a low strain ($\varepsilon = 0.23$) and held for 300s.

As will be discussed later, the above effects can be explained in terms of compositional inhomogeneity, inhomogeneity of deformation, and variations in temperature.

4.4.6 Isothermal Transformation of Austenite to Ferrite

Although the present research is not directly concerned with γ→α transformation, limited isothermal transformation work was carried out primarily to ascertain the effects of inhomogeneities of deformation and of recrystallisation of austenite, as well as of the austenite morphology just prior to the γ→α transformation reaction, upon the size and the homogeneity of the resulting α-grains. For this purpose, samples of the C-Mn base and C-Mn-0.045%Nb steels (casts 11 and 13 respectively) were deformed by upsetting, using various combinations of hot working variables, and subsequently isothermally transformed by quenching for 20 hrs in a sodium chloride (NaCl) salt bath maintained at 600°C, see experimental programme fig. 17. The reason why 600°C is considered an ideal γ→α transformation temperature is discussed in detail in Appendix 1.

Fig. 123a-d show the α-grain structures produced in the base steel (123a&b) and the Nb steel (123c&d), after deforming to a high strain (0.94) at 1100°C and holding for 20s at the deformation temperature to obtain complete recrystallisation of austenite within each sample prior to the transformation. Homogeneous deformation of the base steel resulted in macro-homogeneity of the ensuing α-grains (123a), characterised by the absence of any significant difference between the mean α-grain size in the surface

region (123ai) and those in the central-plane (123aii). On the other hand, samples which underwent inhomogeneous deformation developed large α-grains in the surface planes (123bi) and relatively small ones in the central planes (123bii). The Nb steel exhibited a similar behaviour to the base steel. Fig. 123c shows a typical α-grain structure observed from surface to centre-planes of the Nb steel after homogeneous deformation while fig. 123d shows the structure developed in the surface-plane when deformation was inhomogeneous, the α-grain structure developed at the central plane being similar to that shown in fig. 123c. A comparison of fig. 123c with figs. 123bi & bii shows that the addition of Nb resulted in some α-grain size refinement even at the high deformation temperature of 1100°C. A large number of small, and relatively large, particles can also be seen in the Nb-steel (figs. 123c&d), mainly concentrated at the α-grain boundaries, see also figs. 126 a&b. As discussed in section 5.4.3.5.2c, some of these particles may be Nb(C,N) particles, but the majority of them are most likely spheroidised iron carbide (cementite), Fe_3C.

Fig. 124 shows the effects of lowering the deformation temperature, homogeneous deformation at the macro-level being assured by upsetting with the optimised lubrication technique (section 3.3.4.2). Decreasing the deformation temperature from 1100°C (fig. 124a) to 900°C (fig. 124b) or 850°C (fig. 124c), significantly refined the α-grain size. However, at the lower temperatures of 900°C and 850°C, a mixed α-grain size (fig. 124d) was observed at various positions within the sample despite deformation being homogeneous from surface-to-centre of the sample.

A comparison of fig. 124b with fig. 124c reveals that at the high strain of 0.94, reducing the deformation temperature from 900°C (fig. 124b) to 850°C (fig. 124c) did not produce a significant further α-grain size refinement. However, fig. 125 shows that, at a lower strain ($\varepsilon = 0.49$), the mean size of α-grains developed in the material deformed at 850°C (fig. 125bi) is significantly finer than the mean size of those developed in the material deformed at 900°C (fig. 125ai). Although these particular samples were transferred into the salt bath within ≦1s after being homogeneously deformed at these lower temperatures (900°C and 850°C) so that $\gamma \rightarrow \alpha$ transformation could proceed from totally unrecrystallised, deformed γ-grains, the mixed α-grain size was still observed. As illustrated at lower magnifications in figs. 125aiii & biii, the mixed structure observed is characterised by islands of coarse α-grains which

are surrounded by relatively fine ones.

Fig. 126 summarises, at high magnifications, the structural inhomogeneities observed when deformation was inhomogeneous at a lower strain (0.49), or low deformation temperature (900°C or 850°C), or a combination of a low, or a high strain, with a low temperature. At various positions in the central planes of the samples deformed to $\varepsilon = 0.49$ at 900°C or 850°C, mixtures of coarse and relatively fine polygonal ferrite were observed, fig. 126a; and at some other regions, mixed structures consisting of coarse-grained polygonal ferrite, fine-grained polygonal ferrite, and bainite (essentially acicular ferrite), were seen, fig. 126b. At and closer to the surface planes, bainitic structures predominated, even in samples deformed to the high strain of 0.94 (at 850°C), fig. 126c. It may be observed that the precipitate particles previously noted, occur predominantly at the ferrite-grain boundaries and bainitic boundaries, figs. 126a-c.

4.5 RESULTS OF THE PLANE STRAIN DEFORMATION ON THE COMPUTER-CONTROLLED SERVO-HYDRAULIC MACHINE

4.5.1 Dynamic Flow Stress during Hot Deformation

Fig. 127 shows typical flow curves obtained for the niobium-free austenitic stainless steel (Cast 2) at various constant strain rates in the deformation temperature range, 900-1100°C. Corresponding flow curves for the 0.45%Nb-bearing austenitic stainless steel (Cast 8) are shown in fig. 128. In order to keep the influence of initial austenite grain size within a particular material constant, a common reheating temperature of 1100°C was adopted throughout the tests (section 3.8.2). From figs. 127 and 128, it can be seen that the flow curves for both steels are characterised by a rapid initial rise to a peak stress followed by a gradual fall to a virtually steady state stress at larger strains. The dynamic flow curves obtained for the C-Mn steel (Cast 12) and the C-Mn-0.055%Nb steel (Cast 14) under the same working conditions are presented in figures 129 and 130 respectively and they exhibit similar features to those of the stainless steels.

A comparison of the flow curves in figs. 127 and 128 with those in figs 129 and 130 reveals that the austenitic stainless steels have higher flow stresses than the C-Mn-Nb steels under similar hot working conditions. It can also be seen by comparing fig. 127 with fig. 128 and fig. 129 with fig 130 that the level of niobium addition used in this work resulted in

only marginal increments in the flow stresses probably because of the relatively high testing temperatures used.

4.5.2 Effects of Deformation Temperature and Strain Rate on the Dynamic Flow Stress

It can be seen from figs. 127-130 that the flow stress consistently increases with increasing strain rate at a given deformation temperature and with decreasing temperature at a given constant strain rate. Similarly the flow curves show that the work-hardening rate, $\frac{d\sigma}{d\varepsilon}$, increases with increasing strain rate at the same temperature and with decreasing temperature at a given strain rate. It can also be seen from the curves that, at temperatures $\geqq$1000°C the effect of strain rate tends to diminish as strain is progressively increased in the steady state regime of deformation. Indeed, as illustrated in fig. 131 for the 0.45%Nb stainless and 0.055%Nb-containing C-Mn steels, the strain rate effect on flow stress at 1100°C deformation temperature is well marked only up to the strain prior to the onset of the steady state deformation regime.

The stress at a strain of 0.1, denoted by $\sigma_{\varepsilon=0.1}$, the peak stress (σ_p), and the steady state flow stress (σ_s), at the various testing strain rates and temperatures are summarised in tables 37(a-d) for the four steels investigated. The strain rates shown are those actually observed experimentally rather than the pre-set values. Similarly the indicated centre-plane temperatures are included in Tables 37(a-d). The $\sigma_{\varepsilon=0.1}$, σ_p and σ_s values are presented graphically as functions of testing temperatures in figures 132-136 from which it can be seen that $\sigma_{\varepsilon=0.1}$, σ_p, and σ_s, all decrease as the deformation temperature is increased. The decrease generally follows an exponential path although a few inverse linear relationships seem to occur, particularly at high strain rates. The curves in figs. 132-135 also show that a higher strain rate raises the stress-temperature curve. Fig. 136 shows that a Nb addition has a similar effect on the stress-temperature curve, this effect being more pronounced at lower testing temperatures.

4.5.3 Computation of the Activation Energy for Hot Deformation

The activation energy for hot deformation, Q_{def}, has been evaluated for each of the four steels investigated, at $\sigma_{\varepsilon=0.1}$, σ_p, and σ_s. As a first stage of this evaluation, graphs of $\ln\dot{\varepsilon}$ versus $\sigma_{\varepsilon=0.1}$, σ_p, and σ_s were plotted using the data in Tables 37(a-d). These are shown in figs. 137a-c and 138a-c for the stainless steels, Casts 2 and 8 respectively;

and in figs. 139a-c and 140a-c for the C-Mn steels, Casts 12 and 14 respectively. With the exception of $\ln\dot{\varepsilon}$ vs σ_s for Cast 2 (fig. 137c) and for Cast 8 (fig. 138c) which exhibit considerable scatter of the points, all the curves furnish remarkably good linear relationships, confirmed by computing the correlation coefficients and establishing their significance at the 5% level (Appendices 6a&b). This provides strong evidence that strain rate, $\dot{\varepsilon}$, is related to flow stress, σ, by an exponential law of the form:

$$\dot{\varepsilon} = A\exp(\beta\sigma).\exp(\frac{-Q_{def}}{RT}) \quad \text{---------- (71)}$$

where $\sigma = \sigma_{\varepsilon=0.1}$ or σ_p or σ_s in the present work, and A and β are constants. Mean values of β within 95% confidence limits, evaluated by computing (Appendix 6c) the slope of appropriate $\ln\dot{\varepsilon}$ vs σ plots, are listed in Table 38a.

After the least square fit line

$$\ln\dot{\varepsilon} = \beta\sigma + \text{constant} \quad \text{---------- (72)}$$

had been established at each deformation temperature for the condition, $\sigma = \sigma_{\varepsilon=0.1}$, values of $\ln\dot{\varepsilon}$ were evaluated for $\sigma = \sigma_{\varepsilon=0.1}$ = 60, 100, 150, 200 and 250 MPa. This procedure was repeated for $\sigma = \sigma_p$ and $\sigma = \sigma_s$. The choice of the exact stress levels used for each material was guided by considerations of the range of stress values covered by the experimental flow curves in figs. 127-130 and the range of values of strain rates typically encountered in commercial hot working operations. Thus, the stainless steels (Casts 2 and 8) whose flow stresses generally lie in the 100-300 MP_a stress range were analysed in the stress range 100-250 MP_a. Similarly, after considering the stress values of the C-Mn and C-Mn-Nb steels (Casts 12 and 14) within strain rates of practical relevance to industrial hot working, their $\ln\dot{\varepsilon}$ values were evaluated at stress levels in the range 60-200 MP_a for $\sigma = \sigma_{\varepsilon=0.1}$ and σ_p, and in the range 60-150 MP_a for $\sigma = \sigma_s$. The appropriate values of $\dot{\varepsilon}$ with the associated testing and indicated temperatures at each stress level are shown in Tables 39ai-aiii, 39bi-biii, 39ci-ciii and 39di-diii for casts 2,8,12 and 14 respectively. From these tabulated data, values of $\ln\dot{\varepsilon}$ were plotted against $(1/T)x10^4K^{-1}$, figs. 141-144, for the stainless (Casts 2 & 8) and the C-Mn (Casts 12 & 14) steels. There was a strong linear relationship between $\ln\dot{\varepsilon}$ and $(1/T)x10^4K^{-1}$, confirmed by evaluating the correlation coefficients which were significant at the 5% level. The slopes of each line, denoted by m, was evaluated (Appendix 6C). Since the activation energy for hot deformation (Q_{def}) is defined by

$$Q_{def} = -R\left[\frac{\partial(\ln\dot{\varepsilon})}{\partial(1/T)}\right]_{\sigma_k} \quad \text{cf eqn (34)}$$

then, m can be related to Q_{def} by

$$m = -\left(\frac{Q_{def}}{R}\right) \quad (73)$$

where the Universal Gas constant, R, has a value of 8.314 J/mol. Using this relationship, values of Q_{def} were evaluated at $\sigma_{\varepsilon=0.1}$, σ_p and σ_s for all the steels tested and the results are listed in Tables 40a, 40b, and 40c respectively. The mean values of these Q_{def} values, over the appropriate ranges of stress levels, are discussed in Section 5.5.4 in relation with the Activation Energies for Self-diffusion of iron in the austenite region and for high temperature creep (see Table 43a) and also in relation with Q_{def} values obtained by other workers (see Table 43b).

4.5.4 Influence of Temperature Inhomogeneity within the Material being deformed on the Activation Energy, Q_{def}

The influence of temperature variations within the sample during deformation on Q_{def} was examined by evaluating Q_{def} at the indicated centre-plane temperature. These results, incorporated into Tables 40a-c, clearly show that, at a given strain rate and stress level, Q_{def} moderately increases in those regions within the material where there is a rise in temperature during deformation. Thus Q_{def} varies within the sample as a result of temperature variations within it.

4.5.5 Effect of Stress Level on the Activation Energy, Q_{def}

From Table 40a it can be seen that $(Q_{def})_{\sigma_{\varepsilon=0.1}}$ consistently increases as the stress level increases for all the casts, except cast 8 which exhibited a reverse behaviour, see discussion later. Similarly, $(Q_{def})_{\sigma_s}$ increases with increasing stress level for all the steels including cast 8. In contrast, $(Q_{def})_{\sigma_p}$ generally decreases with increasing stress level, (Table 40b).

4.5.6 Reliability of $(Q_{def})_{\sigma_s}$ compared with that of $(Q_{def})_{\sigma_p}$

Inter-face friction adversely affects the accuracy of true flow stress and, often, lubrication offers little protection at high strains. In this work, in order to assess the continued effectiveness of the applied "dag" lubricant (see section 3.8.2) in the steady state regime of deformation, some samples were deformed to low strains ($\varepsilon = 0.25$) and their external surfaces were compared with those deformed to high strains ($\varepsilon \geq 2.5$). The lightly deformed samples had thin films of lubricant

still left on their surfaces. In contrast, no such residual lubricant film was observed on the surfaces of the samples deformed to high strains. The appearance of these surfaces indicate that lubrication broke down during the latter stages of the deformation. Thus σ_s is more severely affected by friction and so the estimated μ value based upon the existence of some lubricant film throughout the deformation process cannot be valid in the steady state regime.

Figures 145(a-d) show on-line computer graphical plots of flow stress and strain rate against true strain at different test strain rates, for the 0.45%Nb-Austenitic stainless steel (Cast 8) tested at 1000°C. It can be seen from these that, at high and low test strain rates, the value of the strain rate ($\dot{\varepsilon}$) can only be presumed to remain reasonably constant at strains less or equal to ~1.0. Beyond this strain, the strain rate oscillates about the mean value in a violent manner with a general upward trend. Another feature which can be observed from fig. 145b is the tendency for the flow curve to rise after attaining a minimum value at a strain between 2.0 and 2.5. In contrast, the flow stress at the higher strain rates of $12s^{-1}$ and $22s^{-1}$ (figs. 145c and d) tend to fall continuously albeit very slowly.

The consequence of the above is that the steady stage flow stress (σ_s) is difficult to determine uniquely and even when it can be determined, it is unreliable because of the effects of friction and the variable oscillations. The Activation energy evaluated at peak stress, that is, $(Q_{def})_{\sigma_p}$, has therefore been considered more reliable than that evaluated at the steady state flow stress, viz $(Q_{def})_{\sigma_s}$.

4.5.7 Correlation of Temperature Compensated Strain Rate with Peak Stress

For reasons which are discussed in Section 5.5.5, the temperature compensated strain rate,

$$Z = \dot{\varepsilon}\exp\left(\frac{Q_{def}}{RT}\right) \qquad \text{cf eqns(33)\&(39)}$$

has been evaluated using $(Q_{def})_{\sigma_p}$ in preference to both $(Q_{def})_{\sigma_{\varepsilon=0.1}}$ and $(Q_{def})_{\sigma_s}$. Also, the upper limits of $(Q_{def})_{\sigma_p}$ evaluated at the test (furnace) temperature, summarised in Table 40d, have generally been used for computing Z. The computed values of Z at testing temperature T_1, indicated centre-plane temperature T_2, and the mean Temperature $T_3 = \frac{1}{2}(T_1+T_2)$, denoted by $(Z)_{T_1}$, $(Z)_{T_2}$ and $(Z)_{T_3}$ respectively, are summarised in Table 41a for casts 2 and 8 and Table 41b for casts 12 and 14. The relevant activation energies and peak stresses are also included in the